DEPARTAMENTO DE COMUNICACIONES

UNIVERSITAT POLITÈCNICA DE VALÈNCIA

Universitat Politècnica de València

Departamento de comunicaciones

High performance photonic devices for switching applications in silicon photonics

Luis David Sánchez Diana

Supervisor: Dr. Pablo Sanchis Kilders

Tesis presentada para la obtención del título de Doctor por la Universitat Politècnica de València.

Thesis submitted for obtaining the degree of Doctor by the Universitat Politècnica de València.

December 2016

Contents

Acknowledgments 4

Resumen 5

Resum 6

Abstract 7

Introduction 8

1.1. Photonics. 8

1.2. Plasmonics. 13

1.3. Vanadium dioxide. 14

1.4. Objectives and outline of the thesis. 15

Polarization management 17

2.1. Plasmonic polarization splitting and rotation device. 19

2.1.1 Design of the plasmonic rotator. 21

2.1.2 Design of the plasmonic splitter 25

2.1.3 Final design. 31

2.2. Plasmonic TM to TE polarization converter. 31

2.2.1. Design of the coupling and rotating region. 32

2.2.2. Design of the plasmonic polarizer. 35

2.2.3. Final design. 38

2.3. Polarization management controlled by VO_2. 39

2.3.1. Design of the TE pass polarizer. 39

2.3.2. Design of the TM pass polarizer. 45

Optical switching 49

3.1. Method to reduce the power consumption. 51

3.1.1. Simulation results. 51

3.1.2. Experimental results. 56

3.2. Optical switching controlled by vanadium dioxide. 59

3.2.1. Analysis of the 2x2 optical switching structure. 59
3.2.2. Waveguide design. 64
3.2.3. Design optimization for TE polarization. 76
3.2.4. Design optimization for TM polarization. 82
3.2.5. VO_2 optical characterization by ellipsometry. 88
3.2.6. Electrical characterization over VO_2 films. 90
3.2.7. Proposal of a short-circuited electrode. 97
3.2.8. Electro-optical characterization of VO_2/Si devices. 101

VO_2 as active material for other applications 114

4.1. Electro absorption modulation. 115
4.2. Electro absorption modulation with polarization rotation. 119
4.3. Optical memory. 126
4.4. Smart waveguide-based bionanosensor. 128
4.5. Reconfigurable metamaterial for smart material-based surfaces. 129

Conclusions and future work 131

5.1. Conclusions. 131
5.2. Future work. 133

List of publications 136

Bibliography 138

Acknowledgments

To my family,

Especially to my mom. Thanks for your support and for always believing in me. For encouraging me to set my sights higher and to go further. Because you see in me a man better than I really am. This victory does not belong to me, it is yours.

To Zaida,

Thanks for taking care of me even when I do not deserve it.

To my workmates,

Thanks to all of you for teaching me and inspiring me. Each day, working with all of you side by side has been an amazing experience. Without any doubt, the most incredible journey of my life.

To the fabrication team,

For providing me the samples during these years and specially for being so patient with my gds files.

To Antoine Brimont,

Thank you for showing me the kind of person I would like to become. I admire you as a researcher, as a person and as a friend.

To Pablo Sanchis,

For always believing in this work, even when I did not. Because you have been my director, a workmate and a friend. I will be always indebted to you.

Resumen

El silicio es la plataforma más prometedora para la integración fotónica, asegurando la compatibilidad con los procesos de fabricación CMOS y la producción en masa de dispositivos a bajo coste. Durante las últimas décadas, la tecnología fotónica basada en la plataforma de silicio ha mostrado un gran crecimiento, desarrollando diferentes tipos de dispositivos ópticos de alto rendimiento.

Una de las posibilidades para continuar mejorando las prestaciones de los dispositivos fotónicos es mediante la combinación con otras tecnologías como la plasmónica o con nuevos materiales con propiedades excepcionales y compatibilidad CMOS. Las tecnologías híbridas pueden superar las limitaciones de la tecnología de silicio, dando lugar a nuevos dispositivos capaces de superar las prestaciones de sus homólogos electrónicos. La tecnología híbrida dióxido de vanadio/ silicio permite el desarrollo de dispositivos de altas prestaciones, con gran ancho de banda, mayor velocidad de operación y mayor eficiencia energética con dimensiones de la escala de la longitud de onda.

El objetivo principal de esta tesis ha sido la propuesta y desarrollo de dispositivos fotónicos de altas prestaciones para aplicaciones de conmutación. En este contexto, diferentes estructuras basadas en silicio, tecnología plasmónica y las propiedades sintonizables del dióxido de vanadio han sido investigadas para controlar la polarización de la luz y para desarrollar otras funcionalidades electro-ópticas como la modulación.

Resum

El silici és la plataforma més prometedora per a la integració fotònica, assegurant la compatibilitat amb els processos de fabricació CMOS i la producció en massa de dispositius a baix cost. Durant les últimes dècades, la tecnologia fotònica basada en la plataforma de silici ha mostrat un gran creixement, desenvolupant diferents tipus de dispositius òptics d'alt rendiment.

Una de les possibilitats per a continuar millorant el rendiment dels dispositius fotònics és per mitjà de la combinació amb altres tecnologies com la plasmònica o amb nous materials amb propietats excepcionals i compatibilitat CMOS. Les tecnologies híbrides poden superar les limitacions de la tecnologia de silici, donant lloc a nous dispositius capaços de superar el rendiment dels seus homòlegs electrònics. La tecnologia híbrida diòxid de vanadi/silici permet el desenvolupament de dispositius d'alt rendiment, amb gran ample de banda, major velocitat d'operació i major eficiència energètica en l'escala de la longitud d'ona.

L'objectiu principal d'esta tesi ha sigut la proposta i desenvolupament de dispositius fotònics d'alt rendiment per a aplicacions de commutació. En este context, diferents estructures basades en silici, tecnologia plasmònica i les propietats sintonitzables del diòxid de vanadi han sigut investigades per a controlar la polarització de la llum i per a desenvolupar altres funcionalitats electró-òptiques com la modulació.

Abstract

Silicon is the most promising platform for photonic integration, ensuring CMOS fabrication compatibility and mass production of cost-effective devices. During the last decades, photonic technology based on the Silicon on Insulator (SOI) platform has shown a great evolution, developing different sorts of high performance optical devices.

One way to continue improving the performance of photonic optical devices is the combination of the silicon platform with another technologies like plasmonics or CMOS compatible materials with unique properties. Hybrid technologies can overcome the current limits of the silicon technology and develop new devices exceeding the performance metrics of its counterparts electronic devices. The vanadium dioxide/silicon hybrid technology allows the development of new high-performance devices with broadband performance, faster operating speed and energy efficient optical response with wavelength-scale device dimensions.

The main goal of this thesis has been the proposal and development of high performance photonic devices for switching applications. In this context, different structures, based on silicon, plasmonics and the tunable properties of vanadium dioxide, have been investigated to control the polarization of light and for enabling other electro-optical functionalities, like optical modulation.

Chapter 1

Introduction

1.1. Photonics.

Silicon has become the cornerstone of different technologies, specially microelectronics and photonics, due to its optical and electrical properties [1]. Although several properties of silicon can be overcome by other materials, as some III–V compounds or polymers, several reasons have granted silicon its relevant status as the most used semiconductor material in the industrial environment. It is easily procesable because the industrial silicon infrastructure has been widely extended around the world due to the development of electronics in the last decades. Additionally, it is the second most abundant element, so the cost related to the fabrication and process of the silicon wafers are the lowest comparing with exotic materials such as the III–V compounds or lithium niobate ($LiNbO_3$). This reduction in the cost compared to other technologies does not imply a reduction in the properties. In fact, silicon wafers have the highest crystal quality of any semiconductor material. Moreover, related to silicon, silica (SiO_2) and silicon nitride (Si_3N_4) are also fundamental materials for the fabrication of nanodevices. In particular, SiO_2 can be developed thermally over a wafer by means of the interaction between the oxygen and the silicon. The high index contrast between silicon and its oxide, enables a strong light confinement reducing the scale to the nanometer range enabling optical devices with ultra-compact foot-prints [2].

Taking profit of the electrical characteristics of silicon, the electronics industry has experimented an unprecedented growth during the last decades. As a result, highly advanced fabrication processes have been enhanced, enabling the mass production of cost-effective devices. Integrated microelectronic circuits are key components in almost all engineering fields.

In the last decade, the requirements of the communication networks are always increasing in terms of data, bandwidth, energy consumption and users, guiding the networks based on conventional technologies to a bottleneck. The tendency shows that these requirements will continue rising up exponentially.

Nevertheless, the limited quantity of information carried by electrons limits the further development of the information transmission systems. As instance, the major roadblock for multicore processor topologies is the maximum velocity at which the information can be transferred between the cores. At high data rates, the performance of the electrical signals guided by means of copper interconnects is deteriorated due to the crosstalk between connections and due to the losses linked to the resistance of the wires [3]. Especially critical are the losses because they are transduced into heat. The generated heat needs to be dissipated and usually is the limiting factor in a system.

One feasible option consist on using photons instead of electrons as information carriers. Photons are faster, have a higher information capacity and the heat generated in a low loss dielectric is negligible. Furthermore, comparing with electrons, they are less affected by electro-magnetic noise signals commonly founded in harsh environments.

In this context, photonics acquires a key role for the development of future high performance devices. As the electronics technology, photonics uses silicon as the key material, exploiting its optical and electrical properties. Silicon photonics, provides technological reasons to envision great future perspectives in the development of crucial optical integrated devices for telecom, datacom and embedded sensors among others [4].

The fact that both technologies, electronics and photonics, are based on the same material, gives them a perfect compatibility and provides the photonics technology the ability to reuse the highly optimized CMOS manufacturing processes developed by the electronics industry [5]. This is crucial to obtain mass produced and cost-effective optical devices, with advanced functionalities and high performance in terms of efficiency, bandwidth, speed and power consumption.

In fact, silicon manufacturing has the most spectacular convergence of economics of scale and technological sophistication. Depending on the production volume and the complexity level of the chips, the fabrication costs have been highly decreased in the last years.

Table *1* shows a summary of the chip cost in a CMOS foundry as function of the aforementioned statements.

Table 1: Chip cost in a CMOS fab. Data extracted from the ePIXfab Silicon Photonics training course at the ECOC 2015.

	Simple chip (€)	**Complex chip (€)**
Very low volume (100-1000 per year)	100	1000
Low volume (<10k per year)	10	100
Medium volume (10k-1M per year)	1	10
High volume (>1M per year)	0.1	1

However, in spite of all the previously mentioned advantages, silicon photonics also has disadvantages. Table 2 shows a summary of the advantages and the disadvantages of the silicon photonics platform.

Table 2: Advantages/disadvantages of the SOI platform.

Advantages	**Disadvantages**
Silicon is a stable, well understood material.	Indirect bandgap difficults the implementation of optical sources based only on Silicon.
High index contrast allows for ultra-compact devices	High index contrast implies polarization dependence. Lower bound on the dimensions limited by diffraction.
Optical modulation is possible by means of carrier injection or by using the thermo optic effect.	No Pockels effect. Modulation mechanisms are relatively slow.
Optically transparent for wavelengths ranging 1.3 to 1.6µm	
High quality wafers	
CMOS compatibility	

These performance restrictions, linked to the constant growth in the optical application requirements, will impose limitations in terms of size, capabilities and efficiency to the silicon photonics technology. Therefore, these limitations have motivated the hunt for reliable alternatives by the scientific community, seeking

new kinds of technologies or materials able to fulfil the demanding specifications in current photonic systems. For instance, combining Silicon photonics with plasmonics technology will allow to reduce the size of the optical devices beyond the diffraction limit [6,7]. Or, on the other hand, another goal in this moment is to integrate the well-known silicon industrial standards with new compatible materials, so as to develop hybrid structures. In this way, it is envisioned that hybrid technologies can overcome the limits of silicon technology and develop new low-cost and much more robust devices with groundbreaking performances, paving the way to a new era in the photonic industry. Researchers efforts are now focused on the study of the new features that these materials are able to deliver in order to mitigate the current bottleneck performance of silicon-based systems. Materials like germanium and graphene [8-12] have been widely integrated in the SOI platform and recently certain transition metal oxides (TMOs) are under study. TMOs have attracted a considerable interest in different areas like matter physics, chemistry and several fields of engineering due to their unique properties. Due to its electrical capabilities, TMOs have been considered for oxide electronics in different ways; for elements of non-volatile memory, FETS based on materials with semiconductor to metal transition, sensors, devices for signal processing etc. In addition, their integration in the silicon platform makes possible to take advantage of its tunable optical characteristics. Nowadays, several applications in fields like computing, datacom, telecom or space are being developed combining the properties of the TMOs with the silicon platform and allowing a total CMOS compatibility. Figure 1 shows the wide range of applications for the TMOs on silicon technology.

Figure 1: The combination of the TMOs with the silicon platform mix the characteristics of both technologies allowing for new applications in a wide range of fields. Silicon platform ensures CMOS compatibility and low cost volume manufacturing while the TMOs provide tunability in its electrical and optical properties.

Among these TMOs, vanadium dioxide (VO_2) is one of the most disruptive candidates. Its optical and electrical properties can be controlled and tuned by an external signal (electric field, focused optical excitation, temperature variation, strain or pressure). These unique properties allow VO_2 films to be used for building intelligent components for a broad range of optical applications like modulators, polarizers, switches, filters, sensors, detectors etc.

Part of the work of this thesis has been developed in the framework of the European project SITOGA (FP7-ICT-2013-11-619456). The title of the project is "Silicon CMOS compatible transition metal oxide technology for boosting highly integrated photonic devices with disruptive performance" and it is a collaborative project included in the seventh framework programme. The partners involved in the project are the Centre National de la Recherche Scientifique (CNRS, France), Katholieke Universiteit Leuven (KU Leuven, Belgium), Innovations for High Performance microelectronics (IHP GMBH, Germany), IBM Research GMBH (IBM, Switzerland), DAS Photonics (DAS, Spain) and Universitat Politècnica de Valencia (UPV, Spain) which is the project coordinator.

The SITOGA project addresses for the first time the integration of transition metal oxides materials in the silicon photonics platform for offering breakthrough electro-optical functionalities due to their unique properties not present in pure silicon. Such integration combined with the development of beyond state-of-the art photonic devices will pave the way towards a wide range of photonic applications.

The main objectives of the SITOGA project are:

- Develop the technology (deposition pathways and processing) of two innovative TMO materials, $BaTiO_3$ and VO_2, with unique properties for boosting photonic integration in silicon CMOS.
- Demonstrate beyond state-of-the art electro-optical modulation and switching photonic components and develop novel electro-optical functionalities.
- Integrate the developed material technology on the silicon CMOS platform for large-scale manufacturing of highly integrated and complex photonic devices.
- Validate the enhanced capabilities provided to the silicon platform by means of two functional demonstrators and define the roadmap for the exploitation of the developed technology.

1.2. Plasmonics.

As it was mentioned in the introduction, dielectric optical devices are able to carry higher information quantities but their size is limited by diffraction. This problem does not allow the localization of electromagnetic waves into regions much smaller than the wavelength of light in the material, so usually the devices require large foot-prints. The most feasible way to achieve localization of electromagnetic waves in nanoscale regions, circumventing the diffraction limit, is using materials with negative dielectric permittivity like the metals below the plasma frequency [7].

Plasmonics is a nanophotonics field which paves the way to sub-wavelength confinement shrinking the dimensions of photonic optical devices. It is based on the behavior of the electromagnetic modes supported by the metal-dielectric interfaces. These modes are known as surface plasmon-polariton (SPP modes) and are hybrid electron-photon oscillations which propagate along the metal/dielectric interface [13]. In comparison with the modes propagated in insulating medias, plasmonic modes have lower wavelengths which provides sub-lambda confinement without a decrease in the optical bandwidth. In this way, plasmonics allow to ultra-high field confinement, paving the way to optical structures not limited by the diffraction [14], minimizing the size mismatch with nano-scale electronics. Plasmonics applications have been widely studied in several fields as biodetection or high resolution optical imaging among others and a huge amount of devices like waveguides [15], switches [16] or modulators [17-20] have been demonstrated. The ongoing studies of these devices has remarked their interesting capability to concentrate and manipulate light in nanoscale regions. However, SPPs suffer from high propagation losses due to the field concentrated in the metal [21]. In fact, SPPs are not a feasible option to transport optical information. Current works have proposed different ways to reduce propagation losses in plasmonic structures, such as enhanced waveguide guiding structures [15] or electric pumping in an active gain medium [22].

The optimized photonic-plasmonic hybrid technology paves the way for optical devices able to information transfer thanks to the photonics platform with an ultra-compact footprint due to the plasmonics physics.

1.3. Vanadium dioxide.

The combination of new materials with silicon provides new opportunities to develop optical devices with outstanding properties. Polymers, germanium or graphene are some examples of materials integrated in the SOI platform. In the last years, vanadium dioxide (VO_2) has become one of the most disruptive candidates. Especially interesting is its controllable change between an insulator phase and a metallic phase, known as the semiconductor to metal transition (SMT). The phase transition can be triggered by an external signal as an electric field, focused optical excitation, temperature variation, strain or pressure variation. At room temperature, VO_2 is in the semiconductor phase and has a monoclinic structure with high transparence in the infrared spectrum. After inducing the SMT, it changes to the metallic state, having a tetragonal structure with absorbing and reflecting properties. The most substantial optical contrast between the semiconducting and metallic states occurs near 1.5μm, making VO_2 particularly attractive for applications in optical communications. Figure 2 shows a scheme of the change in the electrical resistance and the optical losses due to the SMT induced in the VO_2.

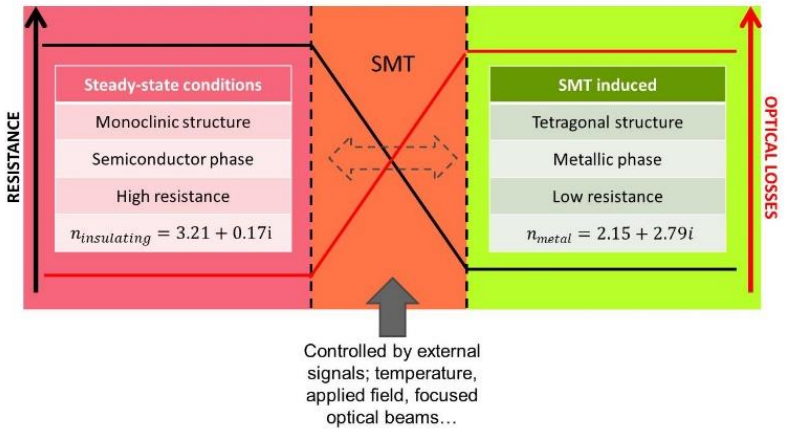

Figure 2: Schematic of the electrical and optical changes induced by the SMT in a VO_2 film.

Reaching the SMT, a change in the conductivity around 4-5 orders of magnitude and a huge increment in the optical losses is accomplished. These variation in the optical losses are due to the large change in the imaginary part of the VO_2 refractive index, $\Delta Im(nVO_2) = Im(n_M) - Im(n_S)$, on the order of +2.6i which is very useful for electro absorption applications among others. Furthermore, the real part of the refractive index also experiments a variation, $\Delta Re(nVO_2) = Re(n_M) - Re(n_S)$, of approximately −1.06 paving the way for huge wavelength shifts in interferometric or resonant structures. Moreover, the great change in the refractive index can give rise to a significant reduction in power consumption as well as in the active length in several optical devices. Table 3 summarizes the

VO_2 properties at optical wavelengths and the enhanced capabilities offered to the silicon platform.

Table 3: VO_2 disruptive properties at optical wavelengths and the enhanced capabilities provided to the silicon platform.

VO_2 properties at 1550nm	**VO_2/Si hybrid technology**
SMT induced via several methods; thermally, electrically or by optical focusing among others.	The different ways to induce the SMT are perfectly compatible with the silicon platform in terms of temperature and power.
Large change of the refractive index including the real and the imaginary parts.	Provides changes in the optical absorption and reduces the footprints and power consumption.
Ultra-fast time response and bistable performance.	Enables groundbreaking applications like ultra-fast optical switches and optical memories among others.

1.4. Objectives and outline of the thesis.

The main goal of this thesis has been the proposal and development of high performance photonic devices for switching applications. In this context, structures to control the polarization of light and for enabling electro-optical functionalities like modulation have been investigated. The thesis has been structured in four principal topics; polarization management, optical switching, optical modulation and the integration of vanadium dioxide in the silicon platform. Each topic has been worked independently and finally they have been linked through the combination with the vanadium dioxide as it is shown in *Figure 3*.

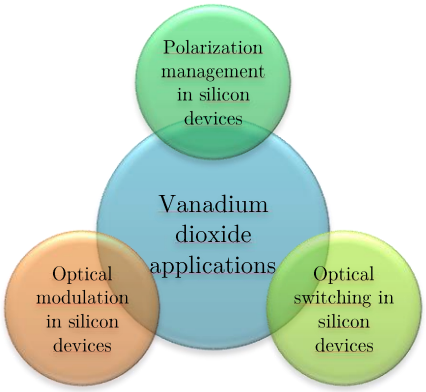

Figure 3: Schematic of the main topics in this thesis. The integration of the vanadium dioxide in the silicon platform provides a way to the interconnection of the different topics.

The first chapter is a brief introduction which aims to describe the characteristics of the silicon technology, plasmonics and vanadium dioxide.

Chapter two is devoted to the polarization management. To ensure the optimal performance of the optical devices based on silicon technology, the control over the polarization of light is a crucial process. This chapter starts with the design of a polarization splitting and rotation device and a transverse-magnetic to tranverse-electric polarization converter, both combining the silicon technology with plasmonics. Finally, the chapter is completed with the design of polarizers controlled by the semiconductor to metal transition of the vanadium dioxide, paving the way for an active polarization management.

The third chapter is focused on the optical switching. Mainly, there are two different ways to improve the performance of the optical switches; improvements in the optical design of the switching structures and improvements due to the enhancement of the physical effect which provokes the switching process. Hence, a silicon switching structure has been optimized to stablish a method to reduce the power consumption. It is followed by a full design, fabrication and characterization of a hybrid vanadium dioxide-silicon switch. The switch has been optimized to have the best performance metrics and experimental results have also been conducted to analyze the power consumption and the phase transition behavior of the vanadium dioxide.

Chapter four is dedicated to the proposal of other applications based on vanadium dioxide as active material. In particular, the implementation of electro-optical modulators is addressed in detail. Furthermore, other potential applications are sketched.

Finally, conclusions and future work are discussed in Chapter 5.

Chapter 2

Polarization management

Polarization is the direction of the electric field (and its related magnetic field) associated with a propagation wave. In optical waveguides the polarization configuration is plane polarized light, which means that the electric vectors are in the same plane (vertical or horizontal respect to the waveguide surface) [23]. According to this, in silicon waveguides there are two different polarizations that can be considered orthogonal; transverse electric polarization (TE) and transverse magnetic polarization (TM).

Due to the high index contrast and the structural birefringence, SOI waveguides are highly polarization dependent. It means that the behavior of the TE and TM modes inside a silicon waveguide is different in terms of losses and dispersion among others [24]. In fact, optical devices are designed to maximize their performance using a specific polarization. Therefore, for each type of optical device it is crucial to achieve the specific polarization to avoid the deterioration of the performance. Polarization management stages based on rotators, converters, polarization beam splitters and polarizers have been widely reported in the SOI platform [25]. These stages provide the possibility of circumvent the problems related to the polarization dependence bringing to each device the appropriate polarization.

Among the different elements dedicated to the polarization management, rotators and splitters are especially relevant. High efficiency in the conversion and the polarization splitting are the desired requirements respectively. Furthermore, ultra-compact size is also desired, seeking high density integration.

The main goal of a rotator is the conversion between the different polarizations of the field. It means, that a rotator provides the ability to convert transverse electric modes into transverse magnetic ones and viceversa with high extinction

ratios and low losses. To achieve the rotation of the field inside the waveguide, rotators are usually based on two main techniques; mode-coupling and mode evolution. Rotators based on the mode coupling condition theory achieve the rotation of the mode coupling the power from the input mode with a certain polarization to an output mode with the opposite polarization by matching the effective refractive index of both modes. The matching is achieved changing the structural dimensions of the waveguide. Therefore, these rotators are less tolerant to fabrication errors [26]. On the other hand, mode-evolution polarization rotators change the polarization of the field by rotating it gradually along the rotating structure. They achieve a better 90° rotation effect, a larger wavelength operation window [27,28] and are less affected to fabrication errors but they usually have larger footprints to smoothly convert the mode adiabatically [29]. Using both techniques, low insertion losses with high values of extinction ratios have been reported reaching high ratios of efficiency.

Recently, a 23μm long pure silicon rotator featuring an ER higher than 17dB over a wavelength range of 40 nm has been experimentally demonstrated [30]. On the other hand, a silicon rotator based on an asymmetrical dielectric loading on the core with a polarization conversion efficiency of 99.8% and losses below 0.2dB has also been reported [31].

Silicon splitters have been also widely studied in the silicon platform. A polarization splitter aims to separate the two orthogonally polarized TE and TM components to be processed individually in the following circuit. Low losses and high crosstalk levels are required to achieve an optimum performance. In the last years, several silicon based splitter topologies have been demonstrated with extinction ratios above 15dB and lengths in the micrometer scale [32-35].

Splitters and rotators are usually integrated together to combine their performances allowing to a higher control of the light polarization. Recently, a fully CMOS compatible compact polarization rotator and splitter with a length of 27μm was experimentally characterized showing an extinction ratio of 20dB with insertion losses below 0.5dB for a wavelength range of 30nm [36].

As it has been mentioned before, polarization management devices based on silicon show high efficiency levels but usually they are penalized by large foot-prints. In the last years, plasmonics has been revealed as a key technology to redefine this components allowing the development of ultra-compact polarization management devices. Comparing with their counterparts in silicon, plasmonic polarization devices are ultra-compact, but they have a lower efficiency due to the inherent losses associated to the interaction between light and metals. Therefore, for both silicon and plasmonic technologies, a trade-off between the

efficiency in the polarization management and the footprint is required depending on the application.

Several plasmonic rotators have been proposed in the last years. Zhang et al.[37] demonstrated an ultracompact 3µm long rotator based on surface plasmon polariton with an extinction ratio of 13dB but with high insertion losses of 12 dB. In 2012, M.Komatsu et al., in [26], showed theoretically the possibility of achieving an extinction ratio of 20dB and less than 4.7dB loss for both polarization conversions for an 11µm long rotator. The same year, J.Niklas et al.[38], presented the design of an ultracompact rotator of 5µm with ER>14dB and low insertion loss of 2.1dB. This design was fabricated and experimentally demonstrated in 2013, showing an extinction ratio higher than 13dB with insertion losses below 2dB for a bandwidth of 90nm [39]. In [40] a polarization conversion of 99.5% with insertion losses of 1.38dB was proposed while in 2014 a rotator for Silicon slot waveguides [41] with insertion losses below 1dB and a polarization conversion efficiency of 97.6% was presented. Recently, a 5µm long mode-evolution-based polarization rotation and coupling scheme with a high coupling efficiency (achieving a 92%), broad bandwidth (around 500nm) and near-zero reflection has been proposed [29].

Plasmonics has been also used to enhance the characteristics of the splitters and polarizers. In 2012, a 6.5µm long plasmonic splitter with ERs higher than 12dB for both polarizations, insertion losses of 2.8dB and 6dB for TE and TM respectively and a bandwidth of 70nm was experimentally demonstrated [42]. In 2013, Y.Huang et al. [43] reported the characterization of an extremely short polarizer (1µm) with a bandwidth of 80nm, extinction ratio of 16dB and insertion losses of 2.2dB. Two years later, a plasmonic nanostructured TM pass polarizer based on a silver nanograting was proposed showing extinction ratios above 35dB with low insertion losses [44]. Recently, a hybrid plasmonic TE pass polarizer compatible with SOI platform has been proposed and experimentally demonstrated. The device is 30µm long, has an extinction ratio higher than 28dB and negligible losses for a broadband response of 150nm [45].

2.1. Plasmonic polarization splitting and rotation device.

Combining the phase matching condition and mode evolution theories with the silicon platform and the plasmonic technology, a novel polarization splitting and rotation device has been proposed and designed. Figure 4 shows a concept art of the performance of the device as function of the input polarization.

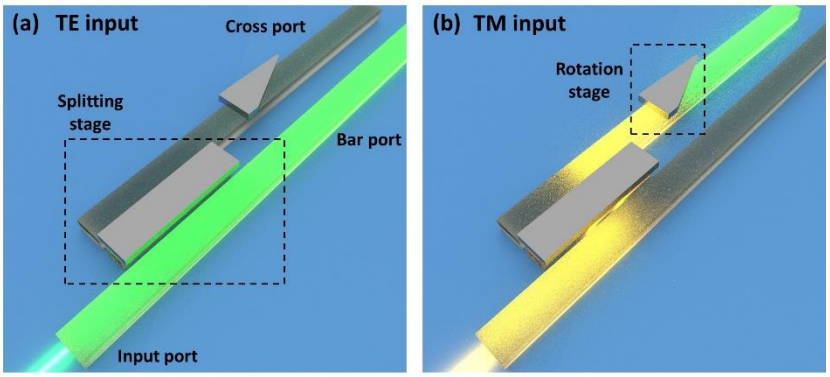

Figure 4: Performance description of the device as function of the input polarization. Green light symbolizes a TE polarization while the yellow light symbolizes TM polarization.

The control over the input polarization is carried out via two plasmonic stages; first a splitting stage to separate the TM polarized signal from the TE signal and finally a rotation stage to convert the TM splitted signal into a TE signal. In the splitting stage, TE signals are guided directly to the bar port while the TM signals are coupled to a parallel waveguide through a hybrid waveguide. This coupling of the TM mode between the three waveguides is achieved via the phase matching condition. The lateral waveguides have the same cross section while the hybrid has been designed in order to have a TM mode with the same effective refractive index than the TM mode of the input/output waveguides. Hence, due to the proximity of the waveguides, the TM mode of the input waveguide is coupled to the TM mode of the hybrid and finally this is coupled to the TM mode of the output waveguide. Nevertheless, the hybrid waveguide does not have a mode similar to the TE mode of the input/output waveguides. This is the main reason why the TE component is not coupled from the input waveguide to the output waveguide through the hybrid waveguide. Thus, with this stage, the TM and TE components are splitted into different waveguides. The splitted TM component is guided to a rotation stage. A plasmonic mode-evolution rotator, converts the TM field into a TE field providing at the end of the stage a second port with a TE output signal. In this way, the TM input component has been splitted and finally rotated into a TE signal. This polarization management device is based on the splitter and the rotator structures proposed in [26] and [42] respectively. However, we have redesigned the components, to obtain the best performance working together while reaching the easiest fabrication process. As instance, we have decided including several restrictions to minimize the number of fabrication steps;

- The rotator in [26] uses aluminum for the metallic layer while the splitter in [42] uses copper. We have redesigned the splitter to use aluminum in

both stages. Furthermore, we have imposed the same thickness (200nm) for both metallizations.

- In the original works, [26] and [42] use a different silica spacer between the silicon waveguides and the metallic layers. Once again, for the design of our polarization management device, we have imposed that both structures must use the same thickness for the silica spacer to avoid the introduction of additional fabrication steps. This restriction implies the necessity of achieving a trade-off between the performance of both structures.

As it is expected, the performance of the whole device is directly related with the performance of the individual structures. The use of plasmonic technology ensures a compact footprint but the optimal design of the components is crucial to achieve low losses and high efficiency.

2.1.1 Design of the plasmonic rotator.

Figure 5 shows a concept art of the performance of the mode evolution rotator. The silicon waveguide has a cross section defined by $W_{Si} \cdot H_{Si}$ while the metallic layer starts with a cross section defined by $W_{Al} \cdot H_{Al}$ and then is linearly tapered. A silica buffer layer with a thickness H_{SiO2} is placed between the waveguide and the metal to reduce the losses. The rotator length and the mismatch between the silicon wire waveguide and the metal layer are L_R and M respectively.

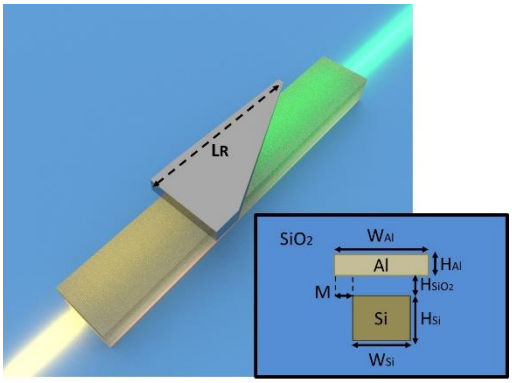

Figure 5: Performance description of the device for the TM to TE polarization conversion. Green light symbolizes a TE polarization while the yellow light symbolizes TM polarization.

The TM mode propagates through the input waveguide until it arises to the rotation region where the aluminum layer is tapered. Then, the mode is hybridized and gradually the polarization of the input mode is rotated along the rotation region.

The lateral mismatch (M) between silicon waveguide and aluminum layer has been fixed to 100nm and the aluminum height to 200nm. In order to obtain a reasonable trade-off between the extinction ratio (ER) and the insertion losses (IL), the rotating length (L_R) and the silica spacer between the silicon waveguide and the metallic layer (H_{SiO2}) has been optimized by means of 3D-FDTD simulations. Figure 6 shows the (a) insertion losses and (b) extinction ratio as function of both parameters. It is important to notice that the scale in the ER has positive values when the silica spacer is higher than 50nm independently of the rotating length. It means that for higher spacers, the device does not rotate the field due to the weak effect of the metallic layer over the guided field. For a coupling length of 5μm and a silica spacer of 20nm, insertion losses as low as 1.9dB with an extinction ratio of 16dB is obtained for a wavelength of 1550nm.

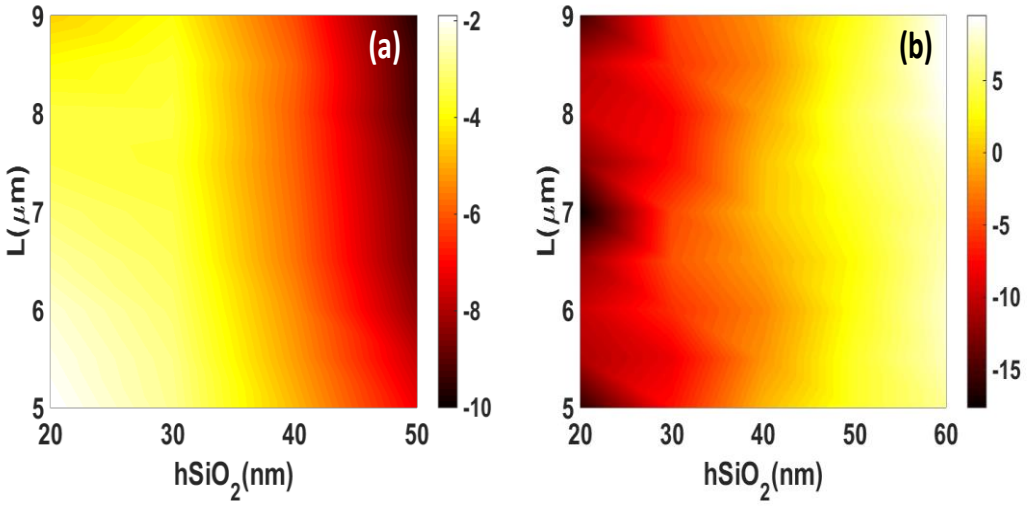

Figure 6: (a) Insertion losses and (b) extinction ratio as function of the silica spacer and the rotating length for the TM to TE conversion.

Figure 7 shows the top and lateral contour maps of the optimized structure. It can be seen how the Ey component of the input is gradually rotated to a Ex component in the output along the rotating section.

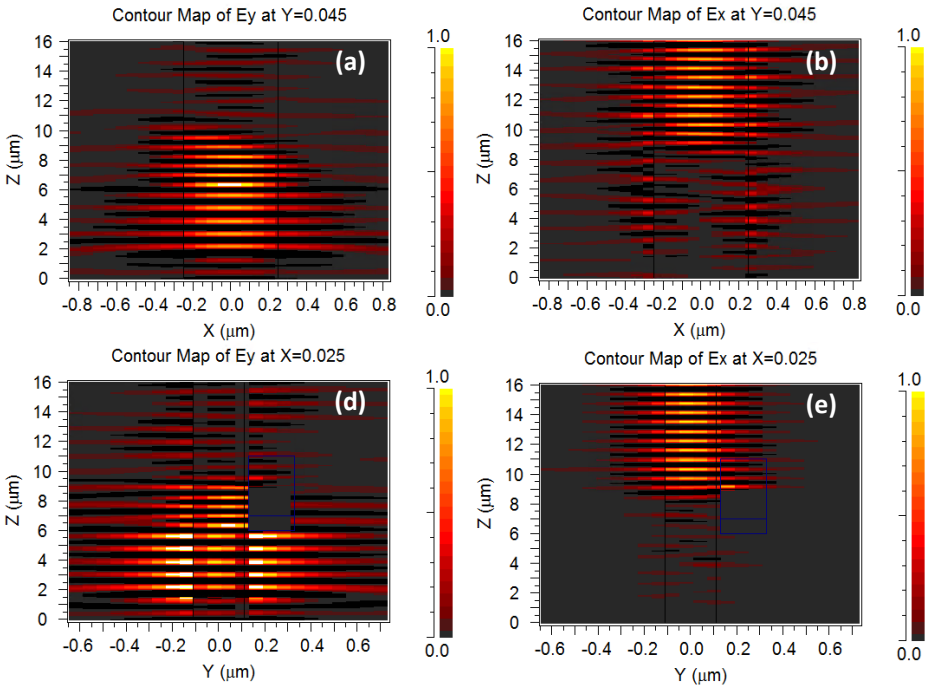

Figure 7: Contour maps of the optimized device. Top and lateral views are displayed for the Ey component (a,d) and Ex component (b,e).

Figure 8 shows the mode evolution along the rotating section. The left column corresponds to the Ex component of the field while the right column to the Ey component. In the input waveguide the mode has a magnetic polarization so the principal component is Ey. When the field reaches the metallization, the field is coupled to the metallic surface and it is gradually rotated as the metallization is laterally displaced respect to the center of the waveguide. Reaching the ending corner of the metallization, the field has been rotated and the Ex component reaches the status of principal component of the field.

The broadband performance of the device has been also demonstrated. For wavelengths ranging 1520 to 1580nm the insertion losses are maintained below 2.5dB and the extinction ratio upper 10dB, as it is shown in Figure 9.

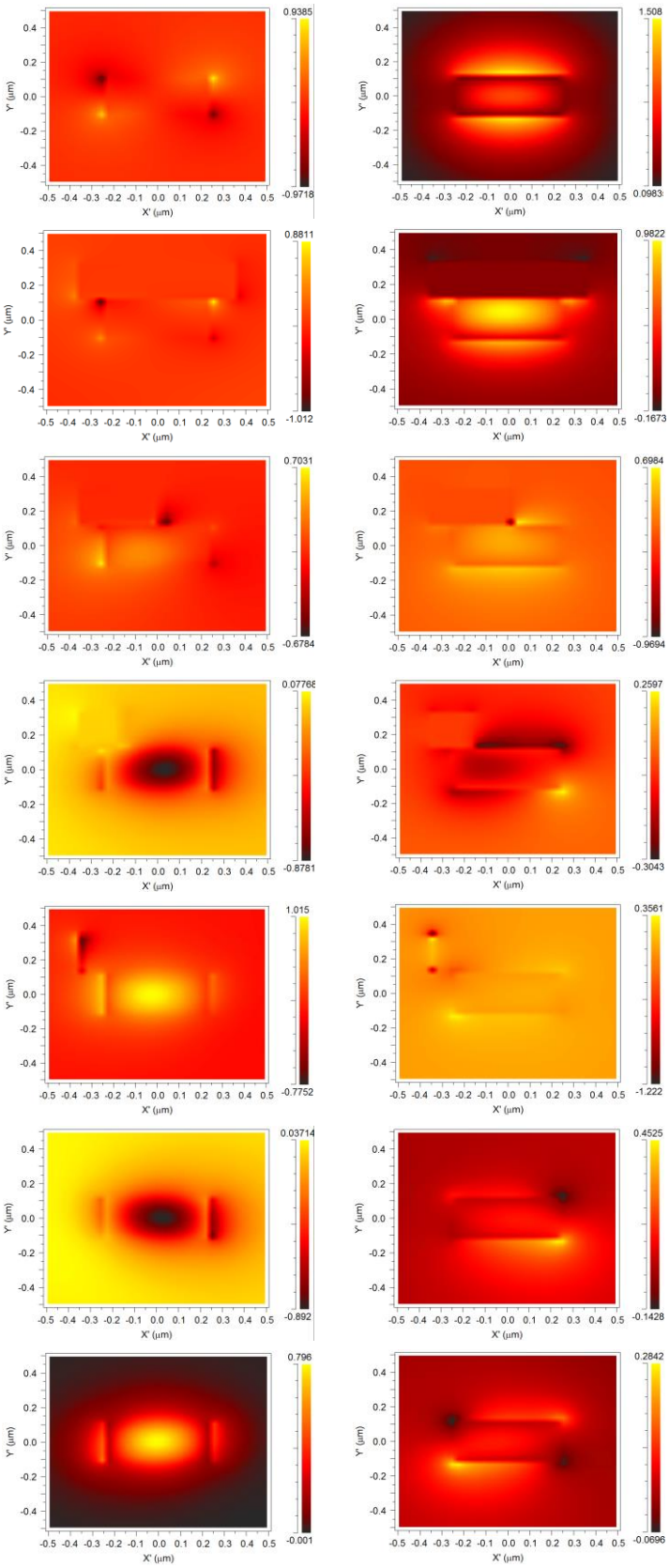

Figure 8: Cross section of the field along the rotating section. The left column corresponds to the **Ex** *component of the field while the right column to the* **Ey** *component. The TM input mode is gradually converted to a TE output mode.*

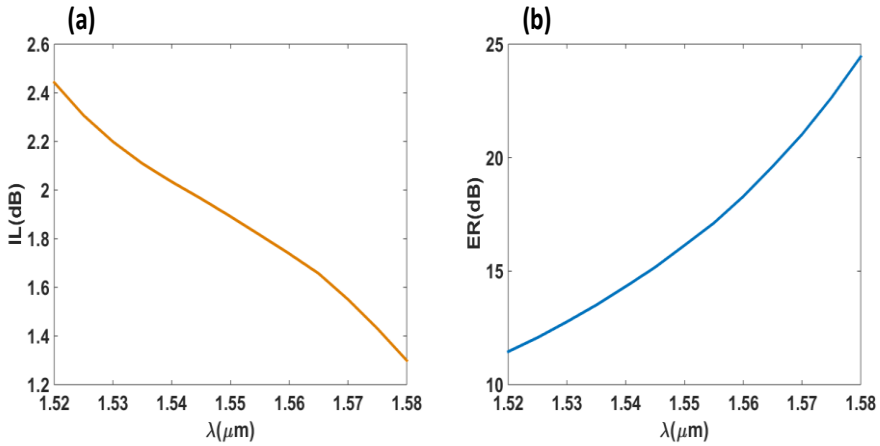

Figure 9: Insertion losses and extinction ratio for the TM to TE conversion as function of the wavelength.

2.1.2 Design of the plasmonic splitter.

Figure 10 shows a concept art of the splitter performance as a function of the input polarization and a cross section of the coupling stage. Silicon input/output waveguides with the same cross section are used to couple in and out the light. Between the waveguides, a hybrid $Si/SiO_2/Al$ waveguide is placed. This waveguide is responsible of the coupling between the input and the output waveguides as function of the input polarization. The main principle of the plasmonic splitter to couple the TM field from the input port to the cross port is the mode coupling theory. According to this theory, a mode of a waveguide excites a mode in other waveguide if the effective refractive index of both modes are the same. In this way, the structural dimensions of the central waveguide can be designed to obtain a mode with the same effective refractive index than the TM mode of the input/output waveguides. The Silicon of the hybrid waveguide has the same height than the external waveguides (H_{Si}) but its width (W_c) is adjusted with the SiO_2 gap thickness (H_{SiO2}) to achieve the phase matching condition between the TM modes of the hybrid waveguide and the input/output Si waveguides. Finally, the coupling length (L_c) and the separation between the central waveguide and the external ones (D) has been optimized to reduce the insertion losses while the crosstalk level is increased.

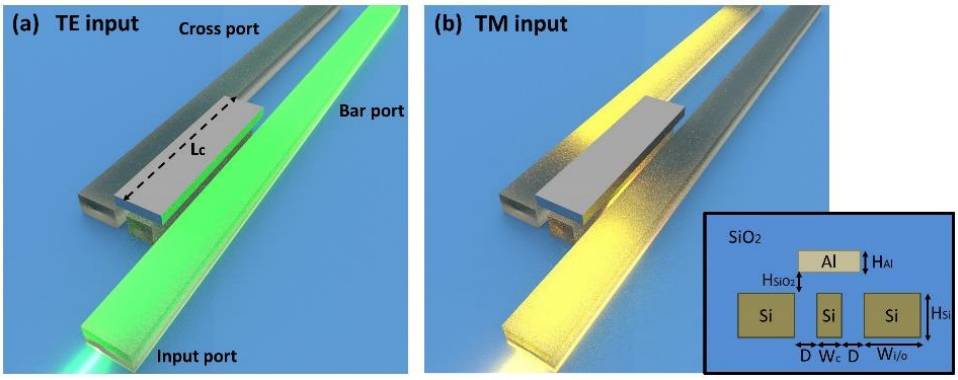

Figure 10: Concept art of the performance of the plasmonic polarization splitter for both input polarizations. The inset shows a cross section of the splitting section.

Summarizing, for TM polarization, the mode of the input/output waveguides and the mode of the hybrid waveguide have the same effective refractive index allowing to exchange power between them. In this way, the input TM field is coupled to the cross waveguide through the hybrid waveguide due to the phase matching condition. On the other hand, for TE polarization, the hybrid waveguide do not have a mode with a similar effective refractive index of the TE mode of the input waveguide. In this case, the TE input field is directly guided to the bar port without coupling to the hybrid waveguide.

In order to achieve the desired performance, the cross section of the waveguides are designed to accomplish the phase matching condition. The height of the silicon waveguides and the thickness of the metal layer have been fixed to 220 and 200nm respectively. In this way, the waveguides can be fabricated using a standard silicon wafer and the thickness of the metallic layer is a feasible value for a deposition process. Therefore, the optimizable parameters to accomplish the phase matching condition are the cross section of the input/output waveguides, the thickness of the SiO_2 spacer and the width of the central waveguide.

For a silicon waveguide with a height of 220nm, the effective refractive index of the TM mode has a value between 1.7 and 1.79 for a width ranging 400 to 500nm, as is shown in Figure 11. So, to achieve the phase matching condition, the silica spacer and the width of the hybrid waveguide has to be optimized to obtain a TM mode with an effective refractive index in the same range. The width of the metal layer has been fixed to 320nm to make the device insensitive to mask misalignment issues by a DUV lithography process [42].

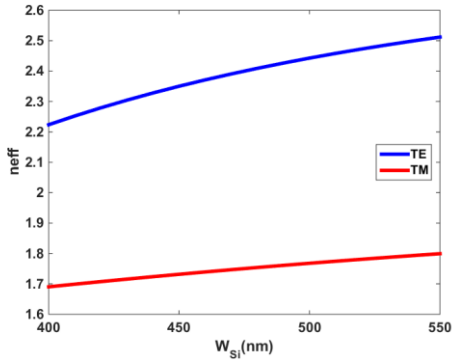

Figure 11: Effective refractive index for the TE and the TM modes of the 220nm thick silicon waveguide surrounded by silica as function of the width.

Figure 12 shows the effective refractive index of the TM mode of the hybrid waveguide as function of the silica spacer and the silicon width. The white dashed lines delimit the area in which the combinations of H_{SiO2} and W_c provide an effective refractive index in the required range to accomplish the phase matching condition.

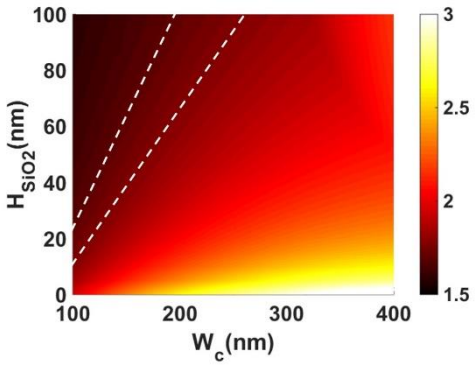

Figure 12: Effective refractive index of the TM mode of the hybrid waveguide as function of the silica spacer and the silicon width of the hybrid waveguide.

Several combinations of silica spacer and waveguide width accomplish the phase matching condition. Nevertheless, this splitter is considered to be integrated in a polarization management stage with the rotator described in the previous section. To achieve an easier fabrication process, one of the crucial requirements in the stage is using the same thickness in the silica spacers for the metallizations of the splitter and the rotator. As it was shown in Figure 6 the performance of the rotator is more sensitive with the silica spacer. So the rotator imposes a silica spacer of 20nm for both devices. According to this spacer and Figure 12 the width of the central waveguide should be 110nm to accomplish the phase matching condition with an effective refractive index of 1.746. Finally, the width of the input/output waveguides is fixed to 470nm according to Figure 11.

Figure 13 shows (a) the TE and (b) TM mode of a 470x220nm silicon waveguide surrounded by silica and (c) the TM mode profile of the hybrid waveguide with a silica spacer of 20nm and a silicon width of 110nm. It can be seen that with the optimization of the dimensional parameters, the effective refractive index of the TM modes of both waveguides are matched ($n_{eff} = 1.74$) ensuring the power transfer between them.

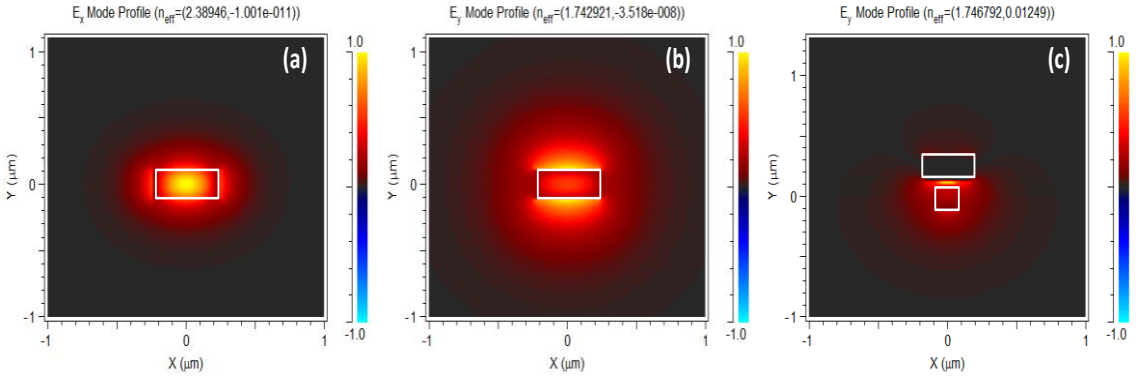

Figure 13: (a) TE mode of the input waveguide. (b) TM mode and (c) its counterpart in the hybrid waveguide. The hybrid waveguide has been optimized to match the effective refractive index of both TM modes allowing an efficient coupling between them.

To have a good performance and optimize the coupling of the TM component from the input port to the cross port, without introducing losses in the guiding of the TE component from the input port to the bar port, the separation between the waveguides and the coupling length have been optimized by means of 3D-FDTD simulations. Figure 14 shows the insertion losses as function of the coupling length and the separation between the external waveguides and the hybrid waveguide. For a coupling length of 6.5µm and a distance between the waveguides of 235nm the insertion losses are as low as 0.85dB.

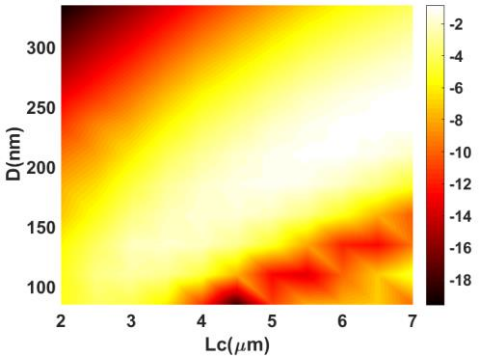

Figure 14: Insertion losses as function of the coupling length and the distance between the input/output waveguides and the hybrid waveguide.

Figure 15 shows the (a) contour map and the modal shape at different points of the structure. At the beginning (b) the TM mode is in the input waveguide. Along the coupling region, the mode is gradually transferred from the input waveguide to the output waveguide through the hybrid waveguide due to the phase matching condition, as it can be seen in (c), (d) and (e). Finally, the TM mode is guided along the output waveguide as it is depicted in (f).

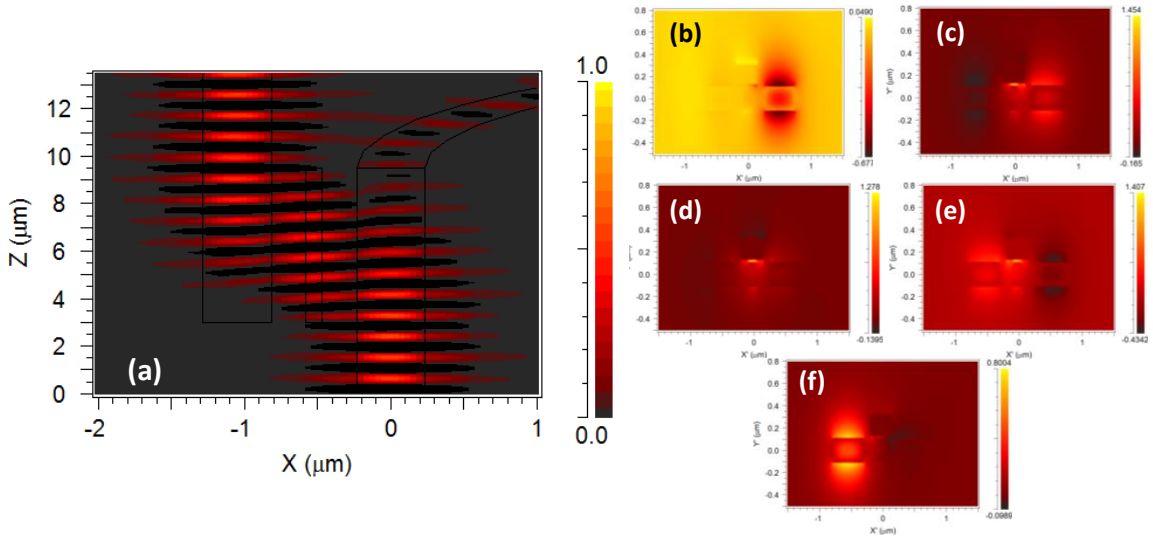

Figure 15: (a) Contour map of the TM propagation along the structure. Insets (b-f) show the gradually propagation from the input waveguide to the output waveguide along the hybrid waveguide.

The performance of the device for TE polarization is also analyzed. As it was expected, the TE mode does not excite any mode in the hybrid waveguide so there is not a coupling between them. In this case, the field is guided directly to the bar port. In this way, the correct performance of the splitter is accomplished; while the TM input mode is coupled to the TM mode of the hybrid waveguide due to the phase matching condition, the TE input mode goes through the device without coupling. Therefore, the input polarizations are splitted providing the possibility of an individual processing. Figure 16 shows (a) the contour map and the modal shape of the TE mode at (b) the beginning of the structure and at (c) the output.

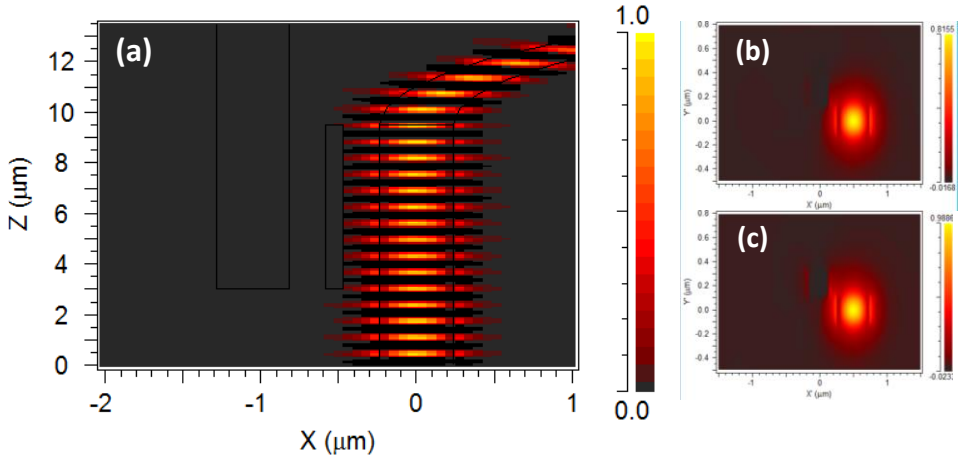

Figure 16: (a) Contour map of the TE propagation along the structure. Insets (b,c) show how the TE input mode is not coupled to the hybrid section and therefore is guided directly to the bar output port.

In order to demonstrate the broadband performance of the device, the insertion losses and crosstalk levels have been obtained as function of the wavelength. Figure 17 shows the insertion losses and crosstalk levels for both input polarizations. For TM input polarization and a wavelength of 1550nm, the insertion losses are 0.85dB with a crosstalk of 37.5dB. Furthermore, for all the wavelength range, the insertion losses are maintained below 1.5dB with extinction ratios higher than 20dB. In the case of TE polarization, the insertion losses are below 0.1dB and the crosstalk between the outputs is extremely low, ensuring the complete independence between them, for the whole wavelength range.

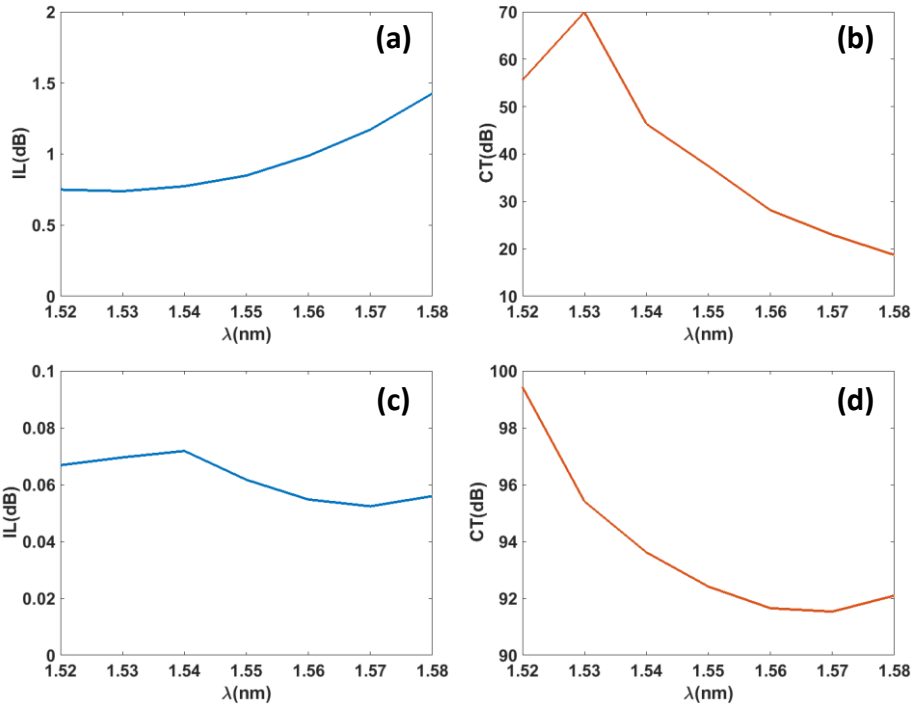

Figure 17: Insertion losses and crosstalk for (a,b) TM and (c,d) TE input polarization.

2.1.3 Final design.

For the optimized structure, combining the converter and the polarizer, Figure 18 shows how the coupling and conversion occurs in the different ports when the input mode is TM or TE polarized.

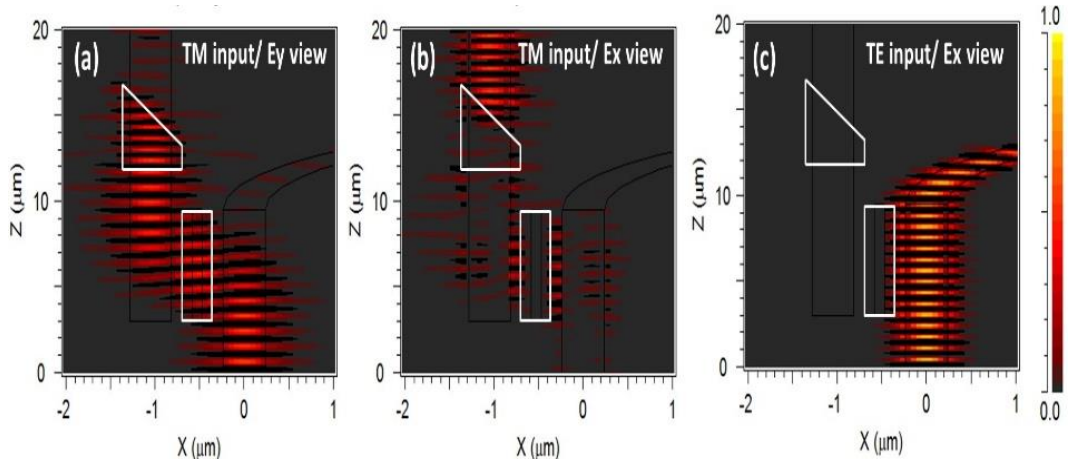

Figure 18: (a) For a wavelength of 1550nm and TM input, the field is coupled to the cross port. (b) The coupled TM field is converted to TE by the rotator. (c) TE input power is guided along the bar port without coupling.

In summary, for a wavelength of 1550nm and TE input polarization, Figure 18(c), the field is not coupled to the output waveguide and is guided to the bar port with insertion losses below 0.1dB and a negligible crosstalk. On the other hand, TM polarization is coupled and rotated to the output waveguide with insertion losses below 3dB and crosstalk higher than 35dB. In this case, the polarization extinction ratio at the output of the rotator is higher than 15dB. A broadband performance over a range of 60nm is also achieved. This work was published in the 10th International Conference Group IV Photonics 2013 [46].

2.2. Plasmonic TM to TE polarization converter.

A novel ultra-compact and low-loss TM–TE converter topology has also been designed. A concept art of the device is shown in Figure 19. It has two metallizations; the first one defines the coupling and rotating region while the second one is a plasmonic TE polarizer. The metallizations have a cross section of $W_3 \cdot H_m$ and $W_4 \cdot H_m$. The height of the metallizations has been fixed to 200nm. The input waveguide has a cross section of $W_{Si} \cdot H_{Si}$ and the cross section of the parallel waveguide is $W_2 \cdot H_{Si}$ where W_{Si} is 500nm and H_{Si} is fixed to 220nm to use a standard SOI wafer.

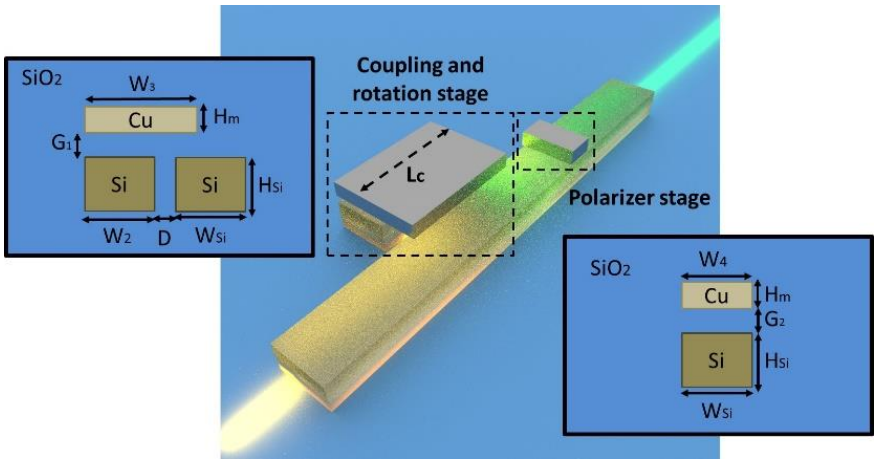

Figure 19: Concept art of the performance of the device for the TM to TE conversion. The first stage converts the TM mode (yellow light) to a TE mode (green light). The second stage rejects the residual TM to improve the extinction ratio of the device.

Such simple rectangular metallizations can be fabricated by standard processing steps; they increase the robustness of the device against potential fabrication inaccuracies by avoiding the use of sharp angles in the metallization [26] or the metal rotation around the silicon waveguide [38,39].The TM input field is guided along the silicon waveguide until it reaches the coupling and rotating region. Then, the field is coupled to the parallel hybrid waveguide. When the field returns to the input waveguide, it is rotated to a TE mode although there is a residual TM component. The physics behind the conversion is similar to previous works [26,38,39]. The electric field at the hybrid structure tends to stay normal to the metallic surface. Therefore, when light is gradually coupled back from the hybrid plasmonic parallel waveguide to the silicon waveguide, the electric field tries to continue being normal to the metallic surface. In such a way, the vertical component of the electric field is gradually rotated into a horizontal component, thus converting the input TM polarization into a TE polarization. Finally, to enhance the performance of the device, the residual TM component is almost eliminated with a polarizer while the TE generated component is guided to the output port without been affected.

2.2.1. Design of the coupling and rotating region.

First, the design of the coupling and rotating region has been realized. The coupling between two parallel waveguides is exploited to achieve the rotation from TM to TE polarization without changing the metallization shape. To achieve this goal, the parallel waveguide with a width (W_2) of 400nm is initially designed without the metal. For a coupling length (L_c) of 5μm and a gap between the waveguides (D) of 50nm, the input TM mode is coupled into the parallel

waveguide and back to the input waveguide for such a length, as depicted in Figure 20.

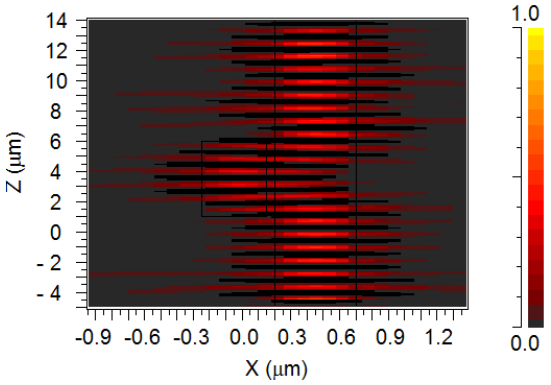

Figure 20: Contour map of the silicon structure without the metallizations for TM input polarization.

The introduction of the metal on top of the parallel waveguide is then used to achieve the TM–TE polarization conversion. In this device, copper has been choosen. The optimum values of the width of the metallic layer (W_3) and the silica spacer between the silicon waveguide and the metal (G_1) have been analyzed by means of simulations. The width of the metal has been simulated for values between 450 nm and 950 nm (full overlapping of the metal over the input waveguide) while the silica spacer has been varied between 10 to 100nm. Figure 21 shows the (a) insertion losses and (b) extinction ratio of the converter stage as function of the width of the metallic layer and the thickness of the silica spacer between the metal and the silicon waveguide. It can be seen that there are several regions with high level of losses and low extinction ratios. This is due because for these combinations of silica spacer and metal width the conversion from the TM mode to the TE mode is not happening. Nevertheless, there are some combinations which provide low losses with high extinction ratios ensuring the correct rotation of the mode.

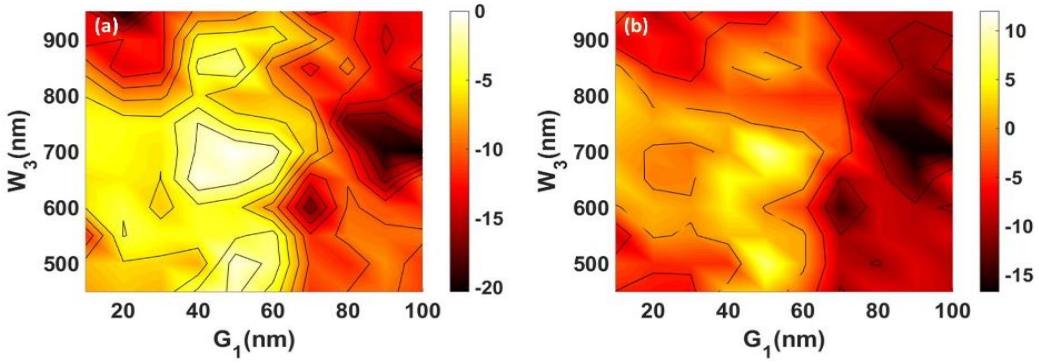

Figure 21: (a) Insertion losses and (b) extinction ratio of the converter stage as function of the width of the metallic layer and the silica spacer between the metal and the silicon waveguide.

Looking for the best trade off to obtain the highest extinction ratio with minimum insertion losses, two combinations of width and silica spacer are especially remarkable. For a width of 500 nm and a silica spacer of 50nm, an extinction ratio of 8.2 dB with insertion losses of 0.75dB are achieved. On the other hand, for the same silica spacer but using a width of 700nm, the extinction ratio is increased to 9.6dB while the insertion losses are as low as 0.12dB. Table 4 summarizes these values as function of the dimensional parameters of the converter stage.

Table 4: Summary of the converter.

λ=1.55μm	W_3	G_1	**IL(dB)**	**ER(dB)**
Topology 1	500	50	0.75	8.2
Topology 2	700	50	0.12	9.6

Figure 22 shows the insertion losses and extinction ratio as function of the wavelength when the silica spacer is 50nm and the width of the metallization is (a) 500nm and (b) 700nm. In both cases, insertion losses are kept below 3.5dB for the whole range, while the extinction ratio has a flatter response for a range of 60nm with values above 9dB using the width of 700nm.

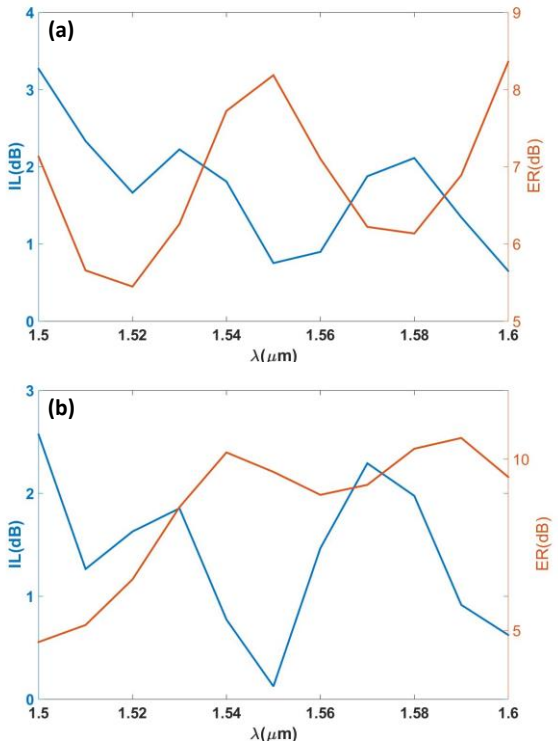

Figure 22: Insertion losses and extinction ratio for a silica spacer of 50nm and a metallization width of (a) 500 and (b) 700nm.

To check the performance of the converter region, Figure 23 shows, for the first topology, the norm of the electric field (||E||), which considers both electric field components, at the input, output and two intermediate positions of the hybrid plasmonic parallel waveguide. The input TM mode, Figure 23(a), becomes confined below the metal when it is coupled to the hybrid plasmonic parallel waveguide, Figure 23(b). As the mode starts to couple again back to the silicon waveguide, Figure 23(c), the electric field tries to continue being normal to the metallic surface and thus the mode is gradually rotated. Therefore, the polarization of the mode at the output waveguide, Figure 23(d), is converted to TE.

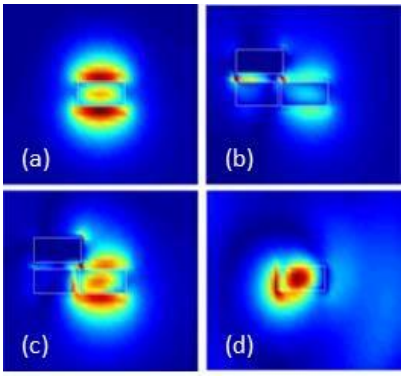

Figure 23: Normalization of the electric field is shown at the (a) input, (d) output and in (b,d) two intermediate positions of the hybrid plasmonic parallel waveguide.

2.2.2. Design of the plasmonic polarizer.

Figure 24 shows the contour maps of the (a) Ey and (b) Ex components when a TM mode is coupled to the optimized hybrid plasmonic parallel waveguide described by the first topology.

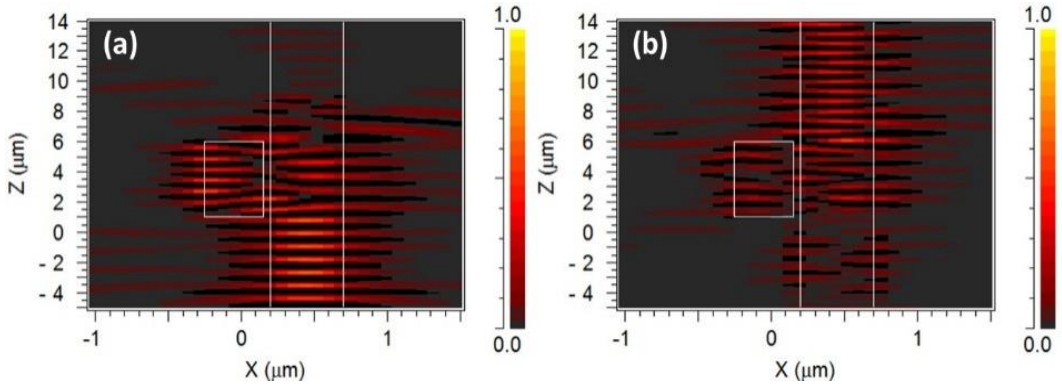

Figure 24: Contour maps of the (a) Ey and (b) Ex components along the structure only considering the rotation stage.

It is shown, Figure 24(a), that there is still a residual TM component at the output. To increase the extinction ratio of the converter, the residual TM

component has to be eliminated. Therefore, a plasmonic TE polarizer is designed to enhance the performance of the whole structure. It introduces high losses to the TM residual component while allows the TE generated signal to pass with low losses.

The TE pass polarizer consists of a metal layer on top of the silicon waveguide. In such a hybrid plasmonic waveguide, the TM mode is mostly confined between the silicon waveguide and the metallization and therefore is highly attenuated when propagating through the polarizer. On the other hand, the TE mode is mostly confined in the silicon waveguide and therefore less affected by the metallization.

For a 1μm long polarizer, the width of the metal (W_4) and the silica spacer (G_2) has been optimized to increase the extinction ratio of the whole structure, while maintaining the insertion losses as low as possible. Figure 25 shows the (a) insertion losses and (b) extinction ratios of the whole structure as function of the polarizer width and the thickness of the silica spacer between the metal of the polarizer and the silicon waveguide for the converter described by the first topology. Figure 25(c) and (d) show the correspondent results for the converter defined by the second topology.

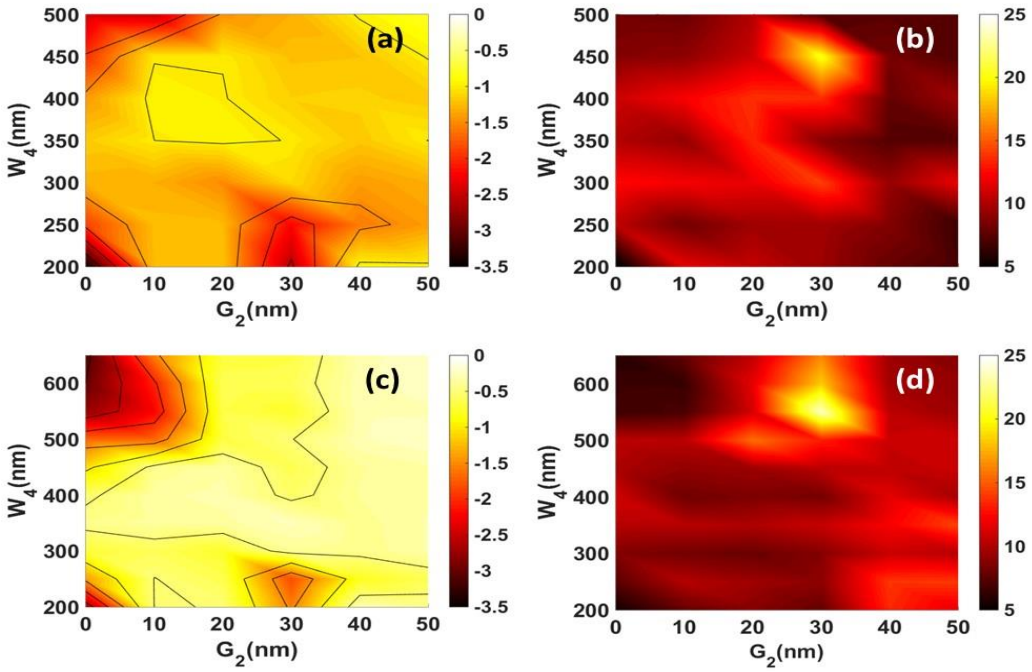

Figure 25: (a) Insertion losses and (b) extinction ratio of the whole structure as function of the polarizer width and the thickness of the silica spacer between the metal and the silicon waveguide when the converter is defined by a width of 500nm and a silica spacer of 50nm. For a converter defined by a width of 700nm and the same silica spacer, the results are plotted in (c,d) respectively.

For each converter topologies there is a combination of W_4 and G_2 which highly enhances the extinction ratio of the whole device. Table 5 summarizes the optimum values of the converter and polarizer stages to obtain the best tradeoff between the insertion losses and the extinction ratio.

Table 5: Summary of the whole converter including the polarizer.

λ=1.55µm	W_3	G_1	W_4	G_2	IL(dB)	ER(dB)
Topology 1	500	50	450	30	1.2	20.43
Topology 2	700	50	550	30	0.75	23.8

In both cases, the extinction ratio has been enhanced upper 20dB while the insertion losses are kept below 1.5dB. It is important to notice the extremely short length of the polarizer (only 1µm) as compared to the 30µm length reported for the isolated polarizer in [47]. Figure 26 shows the spectral response of the insertion losses and the extinction ratio for the structural dimensions defined by the topologies 1(a,b) and 2(c,d).

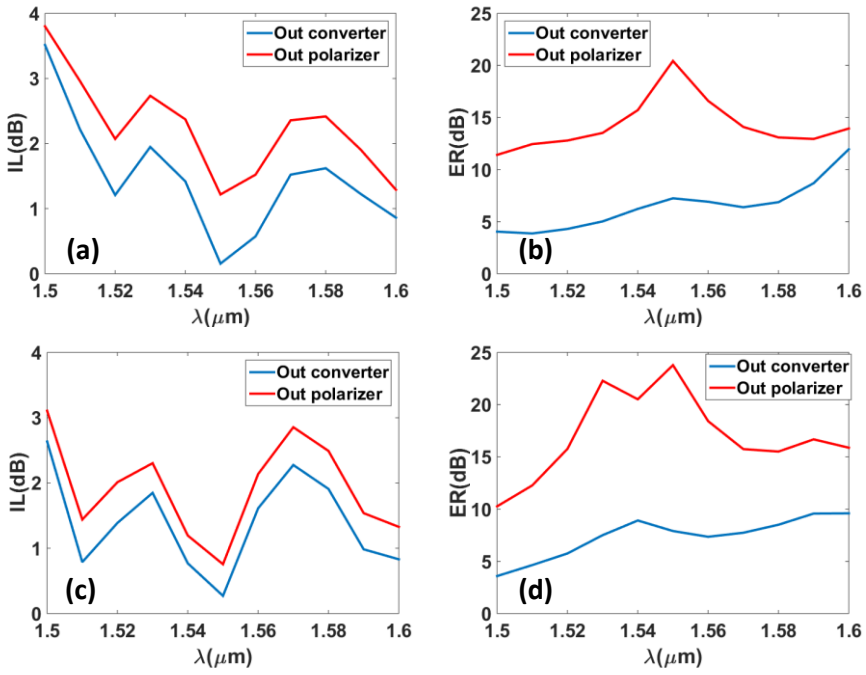

Figure 26: (a,b) Insertion losses and extinction ratio for the first topology. The same results are depicted for the second topology in (c) and (d) respectively.

The second topology provides a bit higher extinction ratios with lower insertion losses than the first topology. Nevertheless, it is important to notice that in this topology the polarizer is wider than the waveguide. In a real fabrication process, it would imply the necessity of a planarization process increasing the number of

fabrication steps. Consequently, we would choose the first topology because it also provides a great performance without complicating the fabrication process.

2.2.3. Final design.

Figure 27 shows the contour maps of the (a) Ey and (b) Ex field components along the whole structure demonstrating the correct rotation of the TM input mode to a TE output mode.

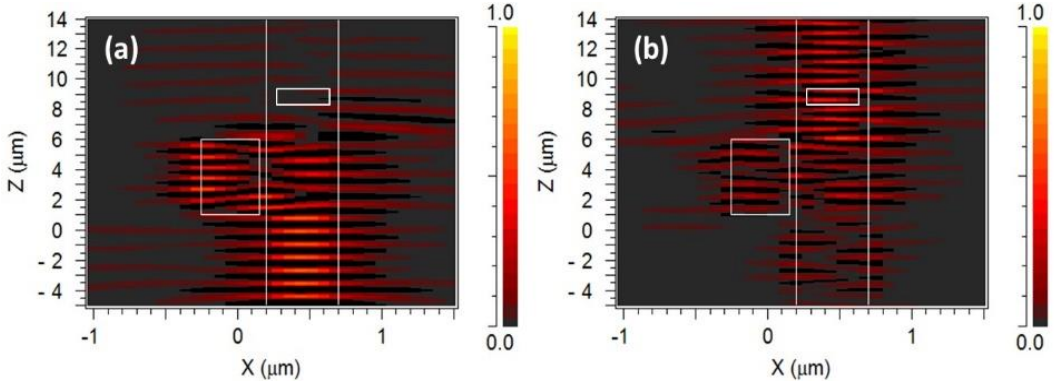

Figure 27: Contour maps of the (a) Ey and (b) Ex components along the structure including the rotation stage and the TE polarizer.

The insets in Figure 28 show the evolution of the Ex and Ey components of the mode along the structure. The TE component appears after the TM–TE converter and crosses the polarizer without noticeable losses. It can be seen that the TM polarization is suppressed after the polarizer. Comparing the first and the last inset it is clearly shown the conversion from a TM input mode (with Ey as the major component) to a TE output mode (with Ex as the major component).

The proposed device, has a total length of 8µm and improves the extinction ratio above 20dB, while maintaining the insertion losses below 1.5dB, at the standard telecom wavelength of 1550nm. This work was published in Optics Letters [48].

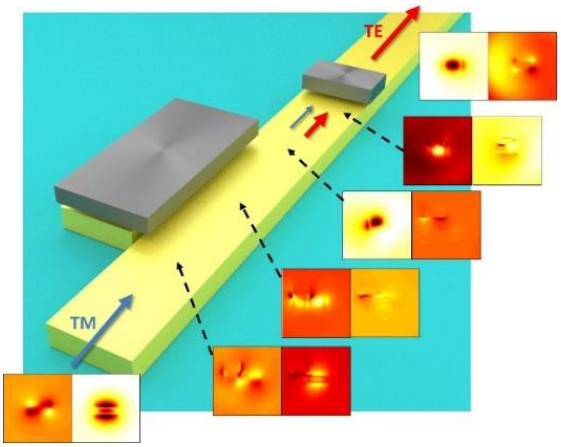

Figure 28: Concept art of the TM to TE plasmonic converter. The insets show the evolution of the mode along the structure. A TM input mode is converted into a TE mode.

2.3. Polarization management controlled by VO_2.

With rotators and splitters, the polarizers are key elements for the polarization control in photonic devices. A polarizer rejects the non-desired polarization while the desired one goes through the polarizer with low losses. A key feature for integrated optical polarizers is make them externally controlled. Introducing the VO_2 to a polarizer structure it is possible to control it by the SMT while maintaining the compatibility with CMOS fabrication techniques. In this way, the elimination of the unwanted polarization in the polarizer can be controlled by an external signal.

We have designed tunable hybrids VO_2-silicon polarizers to control the attenuation of the unwanted polarization taking advantage of the change in the refractive index in the VO_2 during its semiconductor to metal transition. To the best of our knowledge, this is the first time that tunable polarizers compatible with silicon photonics are proposed. Furthermore, devices exhibit an ultra-compact footprint with a total length of only 1µm, insertion losses below 3dB and broadband operation.

2.3.1. Design of the TE pass polarizer.

For the design of the TE pass polarizer, several simulations have been performed using a full-vectorial mode solver based on the finite element method (FEM). A singlemode silicon waveguide with a cross section of 400x220nm shows a TE and a TM mode with a different mode profile. The TE mode has the maximum of its electric field confined in the center of the silicon waveguide. On the other hand,

the maximum electric field in the TM mode is concentrated in the horizontal surfaces of the waveguide. So, the introduction of a VO_2 film over the waveguide will affect more to the propagation of the TM modes than the TE modes. Figure 29 shows concept arts of the polarizer for both VO_2 states when the input field is transverse electric or transverse magnetic. For (a,b) TE polarization, the field goes through the polarizer with low losses independently of the VO_2 phase. Nevertheless, for TM polarization, the VO_2 phase determines the attenuation level of the field. For the (c) insulating state, the VO_2 introduces low losses while during the (d) metallic state the field is almost eliminated due to the great level of losses introduced by the VO_2 patch. Therefore, by changing the VO_2 phase it is possible to control the rejection of the TM polarization.

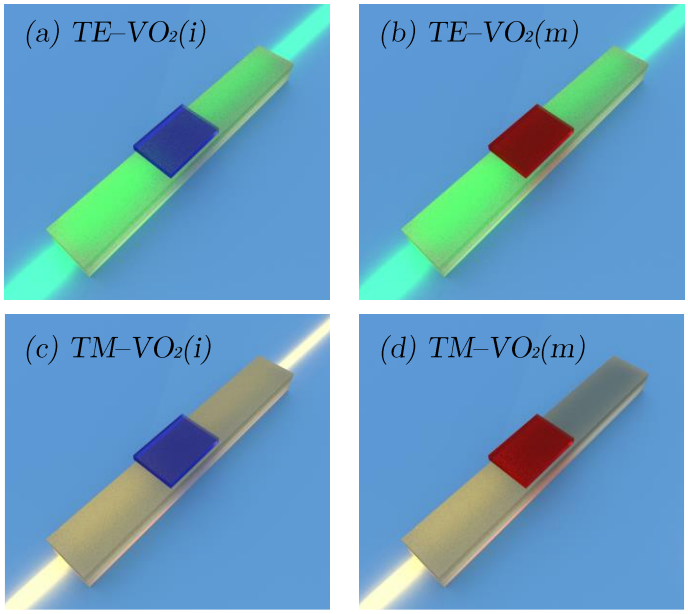

Figure 29: Concept art of the TE polarizer as function of the input polarization and for both VO_2 states. For the (a,c) insulating state, both polarizations go through the polarizer with low losses. On the other hand, for the metallic state, the polarizer introduces low losses for (b) the TE polarization and high losses for (d) the TM polarization.

The design of the TE pass polarizer starts with a waveguide with a cross section of 400x220nm with a 1µm long VO_2 film on top. The refractive index of a VO_2 film with a thickness of 70nm [49] is 3.21+0.17i and 2.15+2.79i for the insulating and the metallic states respectively. The first parameter under study is the silica spacer between the waveguide and the VO_2. Figure 30 shows the losses for the TE and TM polarizations as function of the VO_2 phase and the silica spacer thickness at 1550nm.

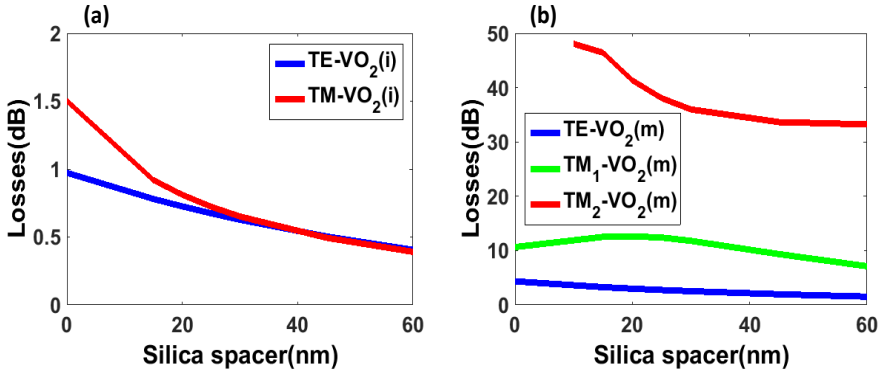

Figure 30: (a) Losses for TE and TM for the insulating state as a function of the silica spacer. (b) Losses for the metallic state as function of the silica spacer. Waveguide width is set to 400nm.

In insulating state, if the spacer is thinner, the losses are higher because the modes have a stronger interaction with the VO_2 film. In Figure 30(a), increasing the spacer is related to a reduction of losses due to the lower interaction. In any case, for a spacer higher than 15nm, the losses for both polarizations are lower than 1dB and for a spacer higher than 40nm the losses in both VO_2 states are the same because the field does not have an interaction with the VO_2. On the other hand, in the metallic state, for a spacer higher than 10nm, it should be noticed that a second TM mode appears but with a high level of losses. If the input field excites both TM modes it will provide an extra level of losses so it will improve the performance. As it was mentioned before, in this state, the polarizer should have low losses in TE and high losses in TM. Taking into account this trade off, for a silica spacer of 20nm the TM shows a local maximum of 12.5dB while the losses in TE are below 3dB. Figure 31 shows the modal shape of the (a) TE mode and the (b,c) TM modes for the metallic state and a silica spacer of 20nm. The TM modes are highly confined in the slot between the waveguide and the VO_2 layer.

Once the silica spacer has been optimized to 20nm, the width of the waveguide has also been optimized. The restriction in this case is the singlemode condition in the insulating state. Studying the structure, the maximum width that ensures the singlemode condition in the insulating state is 480nm.

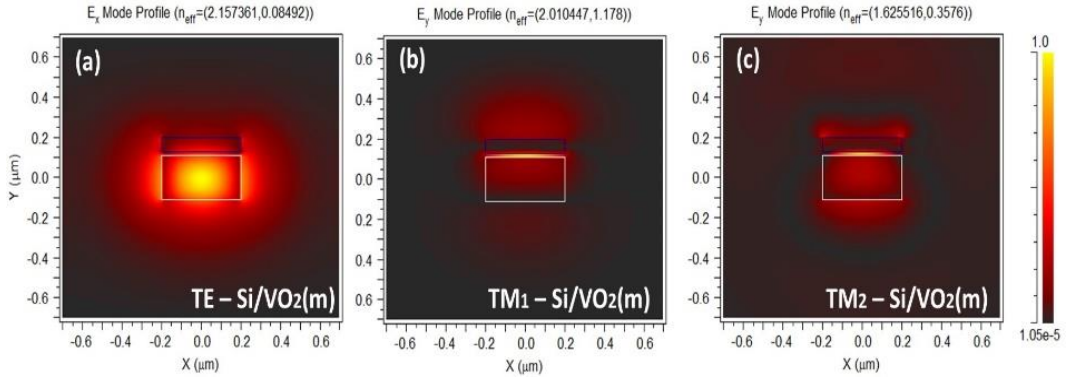

Figure 31: Modes for the hybrid Si/SiO₂/VO₂ waveguide when the VO₂ is in the metallic state. The cross section of the silicon waveguide is 400x220nm, the silica spacer is 20nm and the VO₂ thickness is 70nm.

Figure 32 shows the losses as function of the waveguide width using a silica spacer of 20nm for TE and TM in both states.

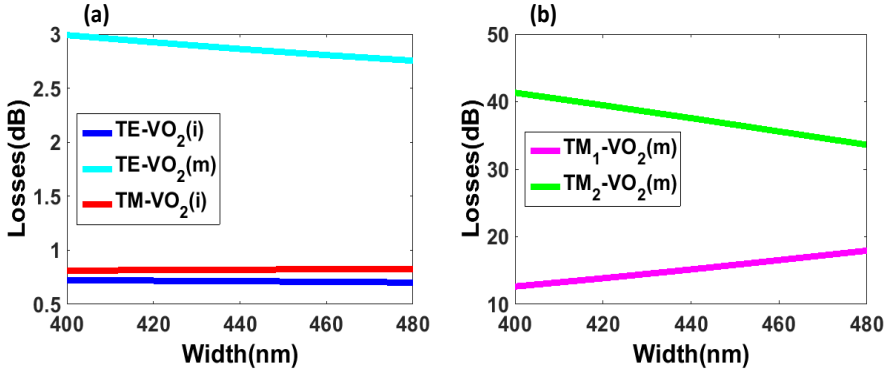

Figure 32: Losses as function of the waveguide width for (a) TE in both states and TM in the insulating state and (b) TM modes in the metallic state. The silica spacer is set to 20nm.

For TE polarization, Figure 32(a), it is desirable to achieve the lowest losses as possible for both states. Increasing the width of the waveguide, the losses decrease slightly so higher widths are more appropriate. In the insulating state, the losses for TM polarization are also maintained below 1dB. On the other hand, it can be seen in Figure 32(b) that higher widths also contribute to increase the losses of the first TM mode in the metallic state which will determine the total attenuation of the unwanted polarization. So again, it is interesting for the appropriate performance of the polarizer to use higher widths. In this way, with a silica spacer of 20nm and a width of 480nm the losses for TE and TM in insulating state are 0.7dB and 0.8dB while the losses in the metallic state are 2.8 and above 15dB respectively. Figure 33 shows the TE and TM modes for the Silicon waveguide and the hybrid Si/VO_2 waveguide as function of the VO_2 state. The TE modes

has a similar modal shape for each case. It allows a soft transition with low losses due to undesired reflections and modal mismatch between the modes of the waveguides. The TM modes of the hybrid waveguide are confined in the slot between the silicon waveguide and the VO_2 layer. In this case the modal mismatch with the mode of the silicon waveguide is stronger. Furthermore, the high confinement enhances the interaction of the mode with the VO_2 doing it more sensitive to the variation in the absorption obtained with the SMT.

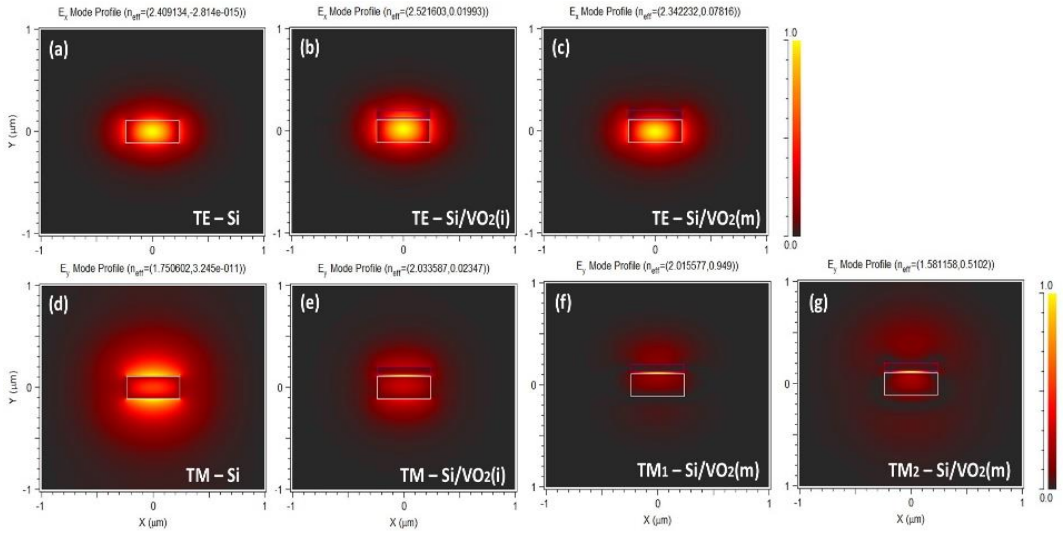

Figure 33: The (a) TE and (d) TM modes of the silicon waveguide are depicted. For the optimized hybrid structure the (b,c) TE and (e,f,g) TM modes are also depicted as function of the VO_2 state.

To confirm the results, the structure has been simulated using a 3D Finite Integration Technique (FIT) which solves Maxwell equations using the recurrent integral method and an hexahedral mesh. Figure 34(a) and (b) show the performance of the device for both polarizations when the VO_2 is in the insulating state. In both cases the field goes through the device with low attenuation. On the other hand, Figure 34(c) and (d) describes the performance in the metallic state. It can be seen that the attenuation for TM is very high and the signal is almost eliminated.

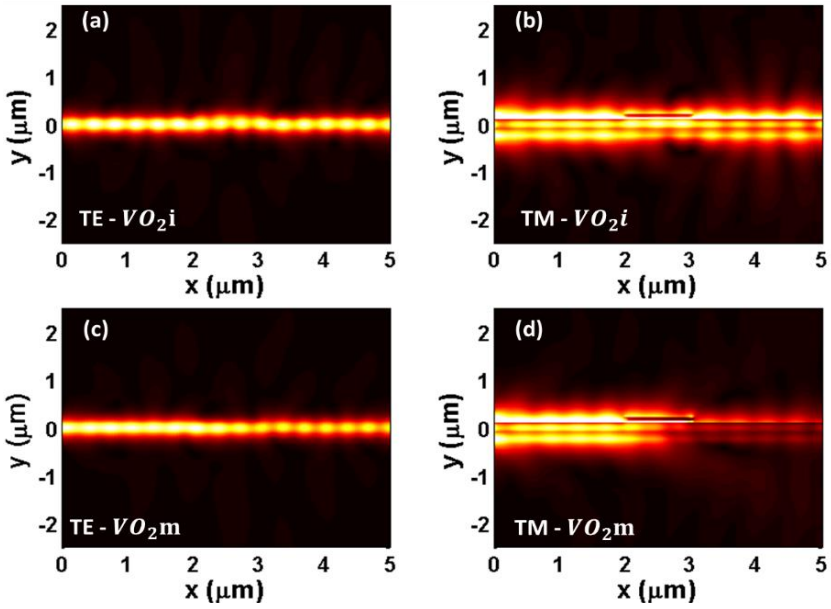

Figure 34: TE pass polarizer performance for the different light polarizations and VO_2 states. Lateral view of the device. TE and TM polarizations for the (a, b) insulating and (c, d) metallic states.

The performance of the device has been also studied for a range of wavelengths of 100nm. In this case, 3D finite difference time domain (FDTD) simulations were performed. Figure 35 shows the spectral response for (a) TE and (b) TM polarizations. It can be seen that results are in very good agreement with the ones calculated by analyzing the modes which indicates that coupling losses as well as the effect of the finite length of the structure are almost negligible. The losses for TE polarization in the metallic state are slightly higher than 3dB when the wavelength increases. On the other hand, the extinction ratio of the TM in the metallic state also decreases when the wavelength is increased, but in any case the attenuation is always higher than 12.5dB for all the wavelength range.

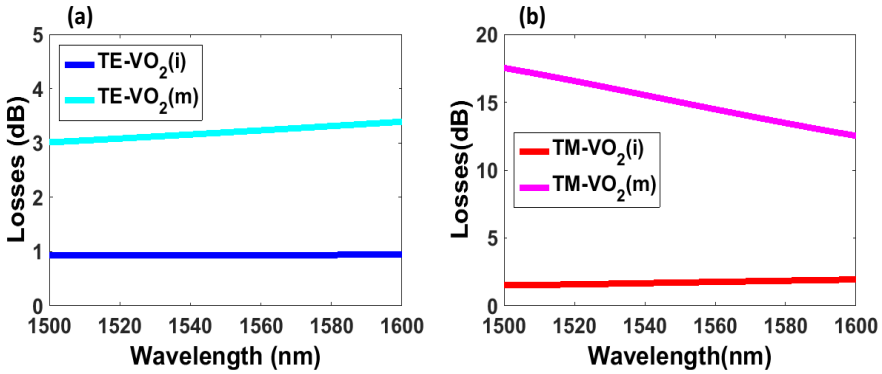

Figure 35: Transmission of TE and TM polarization as a function of the wavelength and the VO_2 state for the TE pass polarizer.

2.3.2. Design of the TM pass polarizer.

For the active TM pass polarizer, to achieve a high interaction between the VO_2 and the TE mode avoiding the introduction of losses to the TM mode, the VO_2 film must be on the sides of the waveguide. Figure 36 shows the concept arts of the TM pass polarizer considering the different polarizations of light for both VO_2 states. For (a,b) TM polarization and both VO_2 states or (c) TE polarization with the VO_2 in insulating state, the device introduces low losses to the field. However, for TE polarization and the VO_2 in metallic state the field is almost eliminated due to the great level of losses introduced by the VO_2 patchs.

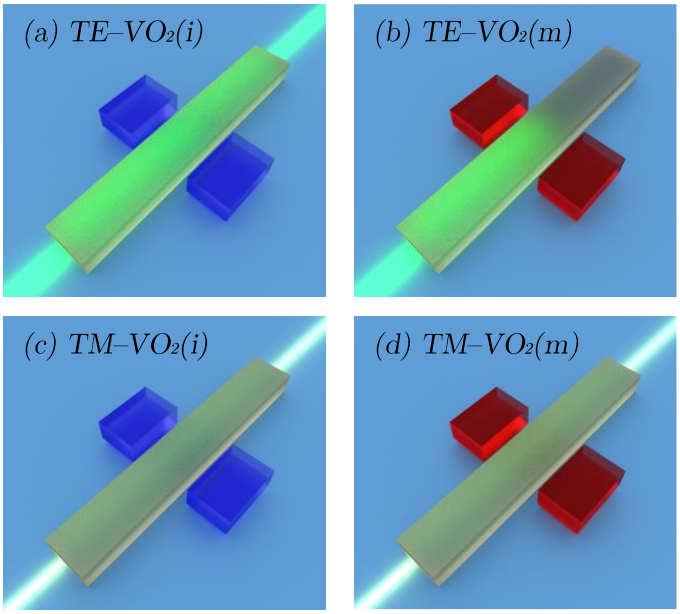

Figure 36: Concept art of the TM polarizer as function of the input polarization and for both VO_2 states. For the (a,c) insulating state, both polarizations go through the polarizer with low losses. On the other hand, for the metallic state, the polarizer introduces low losses for (b) the TM polarization and high losses for (d) the TE polarization.

In order to achieve a higher interaction, the width of the waveguide must be decreased to delocalize the mode. But at the same time, the width must be high enough to ensure low propagation losses of the TM mode. Our trade-off consists of achieving the maximum attenuation of the unwanted TE polarization in the metallic state by keeping insertion losses below 3dB. The influence of the waveguide width and the thickness of the silica spacer between the silicon waveguide and the VO_2 have also been analyzed. Fixing the silica spacer to 20nm, as a first approximation to facilitate the combination with the TE polarizer

presented in the previous section, the width of the waveguide has been decreased from 400nm to 300nm.

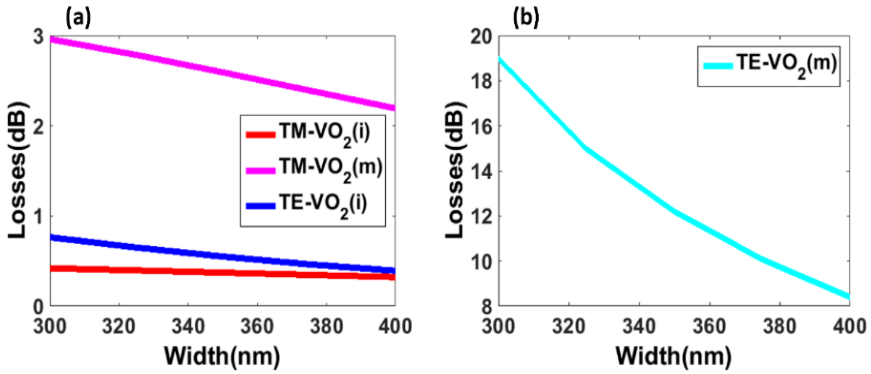

Figure 37: Transmission of the TM pass polarizer as a function of the waveguide width for both light polarizations and VO_2 states. The silica spacer is 20nm.

In Figure 37 (a), it can be seen that insertion losses are slightly increased when the waveguide width decreases. However, narrower waveguides allow to significantly increase the attenuation of the TE polarization in the metallic state, as it is depicted in Figure 37(b). Therefore, an optimum width of 300nm has been chosen that ensures that insertion losses are below 3dB at both VO_2 states. Once the optimum width has been selected, the influence of the silica spacer has also been analyzed. Results are shown in Figure 38. Smaller spacers also contribute to increase insertion losses, as seen in Figure 38(a), but on the other hand it has the benefit of a larger attenuation of the unwanted TE polarization, as shown in Figure 38(b). Therefore, a silica spacer width of 10nm has been chosen to keep insertion losses below 3dB.

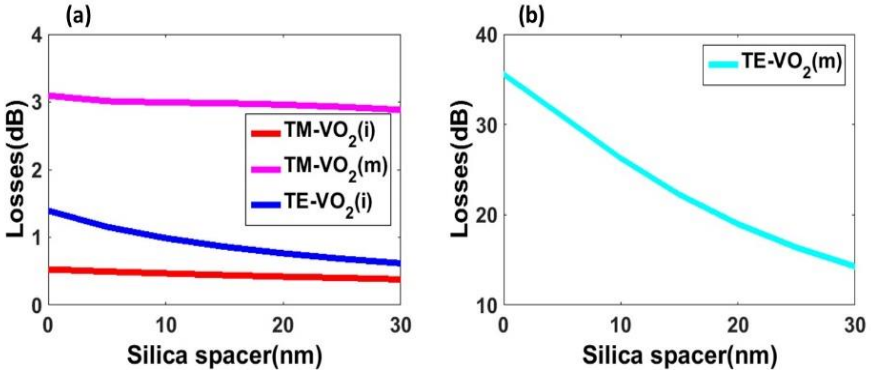

Figure 38: Transmission of the TM pass polarizer as a function of the silica spacer for both light polarizations and VO_2 states. Waveguide width is set to 300nm.

Figure 39 shows the performance of the TM polarizer for the different states and polarizations. For the insulating state, Figure 39(a) and (b), the optical field shows a low attenuation for both polarizations while for the metallic state the

field is highly attenuated for the TE polarization and low attenuated for TM polarization (Figure 39(c) and (d) respectively).

In Figure 40, the spectral response calculated with 3D-FDTD is shown between 1500 and 1600nm. It can be seen that a broadband operation range is also achieved. Results are also in good agreement with the ones calculated by analyzing the modes except for the extinction ratio of the unwanted TE polarization. The attenuation was higher than 20dB in Figure 38. However, by using FDTD as well as FIT simulations, the attenuation is reduced to around 17dB at 1550nm. We attribute this discrepancy to the finite length of the structure. In any case, the attenuation is above 12.5dB for all the wavelength range.

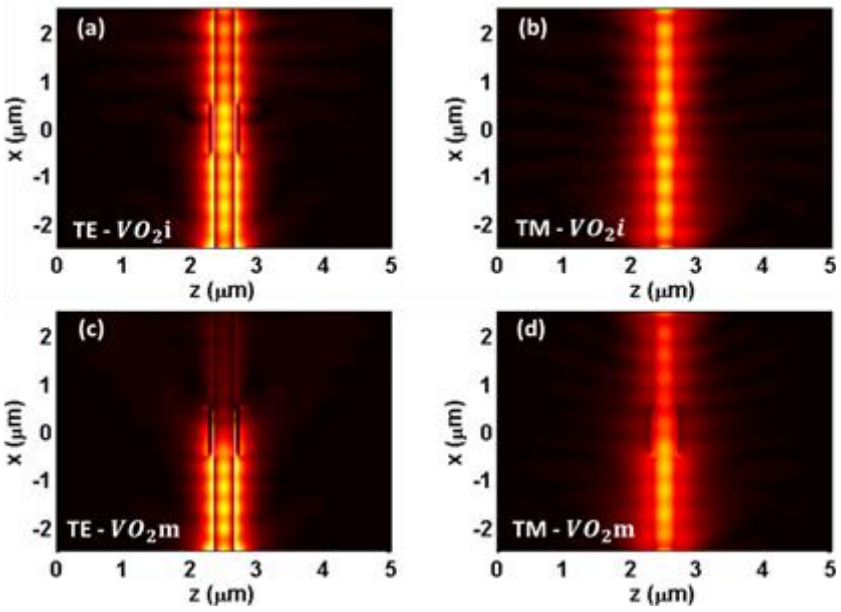

Figure 39: TM pass polarizer performance for the different light polarizations and VO_2 states. Top view of the device. TE and TM polarizations for the (a, b) insulating and (c, d) metallic states.

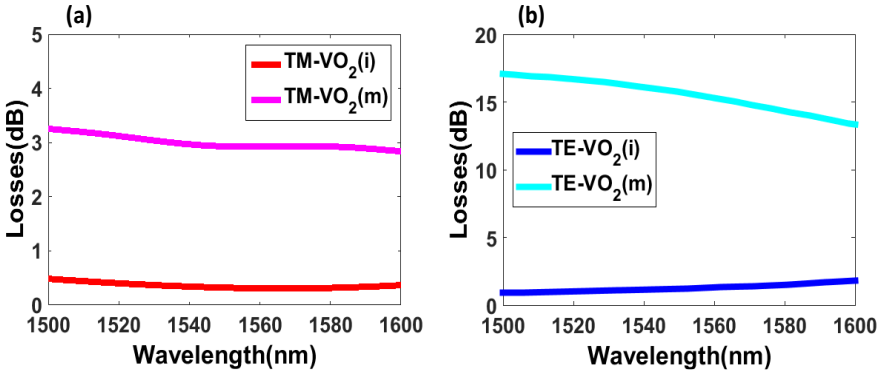

Figure 40: Transmission of TE and TM polarization as a function of the wavelength and the VO_2 state for the active TM pass polarizer.

In summary, the design of a tunable TE and TM pass polarizers based on a hybrid VO_2/Si waveguide structure has been described. Tunability is achieved by exploiting the ultra large change of the refractive index in the VO_2 between the insulating and metallic states.

In order to achieve a full control of the polarization of the input signal, the two proposed polarizers can be integrated in a compact structure to control both polarizations. Figure 41 shows the schematic of the combined structure. Tapers of 3µm length have also been simulated to ensure negligible losses during the transitions between waveguides with different cross sections. The total footprint of the device would be lower than 4µm^2. Depending on which polarizer is active it is possible to eliminate the unwanted polarization. Four main cases must be considered; both polarizers in the insulating state and TM pass polarizer or TE pass polarizer in the metallic state. If the polarizers are in insulating state, both polarizations would show losses below 3dB. For the other cases, the unwanted polarization would be attenuated above 17dB while the desired polarization would have losses below 5dB. This work was published in Optics Letters [50].

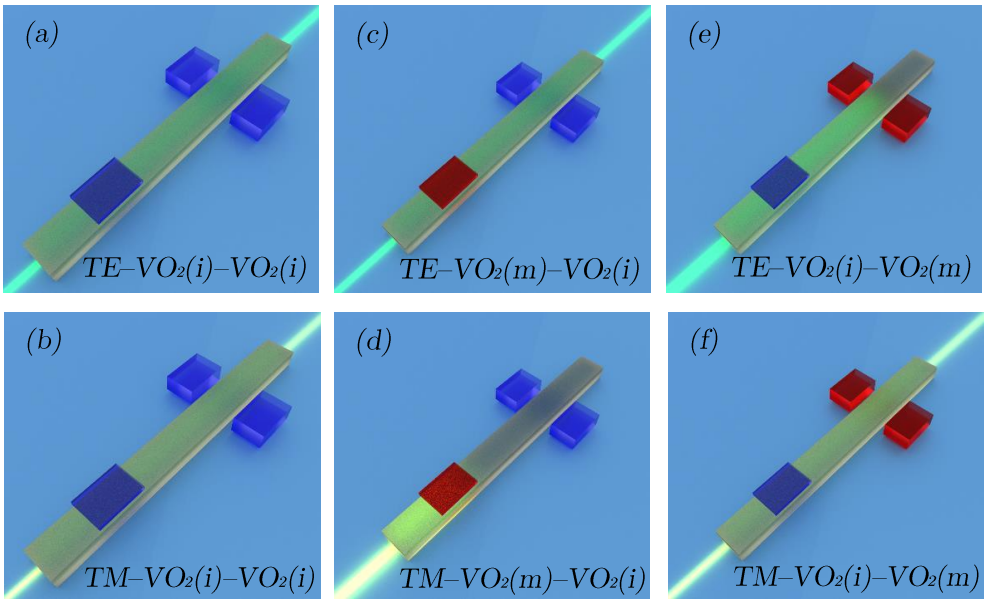

Figure 41: Schematic of the combined structure for the main performance modes.

Chapter 3

Optical switching

During the last decades, silicon photonic building blocks like modulators, filters, detectors or switches have been improved in terms of speed, sensitivity, power consumption and losses. Ring resonators and Mach-Zehnder interferometric structures (MZIs) are the most common structures for optical switches in photonic integrated circuits. MZI-based switches exhibit broadband spectral operation and their electro-optic switching performance may be achieved using the thermo-optic (TO) or the plasma dispersion effects. The TO effect suffers from higher power consumption and is slower than the plasma dispersion effect but it enables larger phase shifts per unit length due to silicon's high thermo-optic coefficient, and it is also fast enough for switching applications.

In order to achieve a better performance than current electrical networks, optical networks will require low power consumption, low latency and high bandwidth [51,52]. To achieve this, it is necessary to improve optical switching matrices whose overall performance are directly related to the characteristics of their optical switches. Therefore, a key point to improve is the efficiency and power consumption of optical switches (based on ring resonators [53,54] or MZI structures [55,56]) in order to obtain high performance optical networks. MZI-based optical switches using the TO effect feature high efficiency but usually require their power consumption to be reduced in order to ensure low power operation. Recent works showing a 4x4 switch with a power consumption below 20.4mW for a bandwidth per port of 40Gbps [55], a 2x2 non-blocking switch matrix based on MZI with a total power consumption which varies from 4.55mW to 22.4mW depending on the switching state and physical path [57], a Mach Zehnder-based five-port silicon router with a consumed power of 25mW[58] or a Mach-Zehnder based four port switching module with a power consumption from 9mW to 42.6mW [59] have been demonstrated.

Another way to reduce the power consumption and the footprint of optical switches is by the combination of the photonics platform with CMOS compatible materials. The combination of high-contrast waveguides and active materials, like the vanadium dioxide, together with microring resonator structures provides a unique path towards the development of switching components with best performance. The microring resonator is a very versatile photonic component that has been proposed for enabling a large variety of passive and active functionalities such as (de)multiplexing, filtering, modulating, switching or sensing. On the other hand, VO_2 has been proposed for the development of ultra-compact modulators and switches in the silicon photonics platform. The integration of VO_2 with silicon photonic devices was demonstrated several years ago. The fabrication of VO_2 thin films grown on a silicon-on-insulator (SOI) photonic waveguide was demonstrated to develop ultra-compact absorption modulators [49]. A very strong variation of the refractive index was measured which indicated a clear transition from a nearly transparent state to a phase with metallic optical properties. The more than 16-fold increase in absorption in VO_2 was exploited for demonstrating absorption modulation with an extinction ratio of more than 6.5dB with only 2dB insertion losses over a 2µm active length by using a 65nm-thick VO_2 layer on top of the silicon waveguide. Two years later, thermo-optically induced switching of a hybrid Si-VO_2 micro-ring resonator with extinction ratios up to 10dB was also demonstrated [60]. The modulator consisted of a submicron long and ~70nm thick patch of VO_2 material integrated onto a silicon ring resonator as small as 1.5µm in radius. In this case, a pump laser focused onto the device was used to photothermally induce the transition in the VO_2. Optical modulation in excess of 7dB from modest Q-factor (~10^3), and therefore high-bandwidth (>100GHz) ring resonators, was demonstrated [61]. Furthermore, the change in the imaginary part of the VO_2 refractive index was used for enabling electro-absorption modulators. Hybrid structures based on a silicon waveguide covered with a VO_2 patch ranging from 0.5µm to 1µm was proposed showing modulation depths of 4dB/µm and insertion losses between 0.5dB to 2dB [61]. Optical modulation by means of an electric-field has also been recently demonstrated by the same group [62]. However, discrepancies between simulations and experimental results were observed and attributed to a combined effect from applied electric field and Joule heating. More recently, a 1µm long electro-absorption modulator with an extinction ratio of 10dB and modest insertion losses of 5 dB has been demonstrated [63].

The use of plasmonic structures has also been theoretically proposed by combining VO_2 with metals [64,65] and experimentally demonstrated in a structure based on SOI [66].In the latter, switching voltages of 0.4V were sufficient to attain an extinction ratio higher than 20dB by using a thermally induced VO_2 phase

transition. However, the coupling to conventional silicon waveguides is challenging. More recently, an electro-absorption modulator based on a silicon slot waveguide with VO_2 in the slot region and coupled to a standard silicon waveguide has also been theoretically proposed [67] and a plasmonic structure with optimum coupling has been analyzed by means of simulations but the achieved extinction ratios were below 9dB [68].

3.1. Method to reduce the power consumption.

Considering the necessity of reducing the power consumption of the switching blocks, we propose a novel approach to minimize the power consumption required for switching between two states in an asymmetric Mach-Zehnder structure in comparison with the symmetric counterpart. The approach is based on taking advantage of the periodic response of the transmission spectrum in the asymmetric MZI (a-MZI) structure. Switching power consumption reduction from 32% to 50% is experimentally demonstrated for bit rates ranging from 10 to 30Gbps introducing only an extra level of insertion losses below 0.5dB.

3.1.1. Simulation results.

Figure 42 show (a) the 3D schematic of the a-MZI switching structure, (b) a scanning electron microscope (SEM) image of the fabricated device, (c) the cross section of the considered waveguide and (d) the fundamental transverse electric mode.

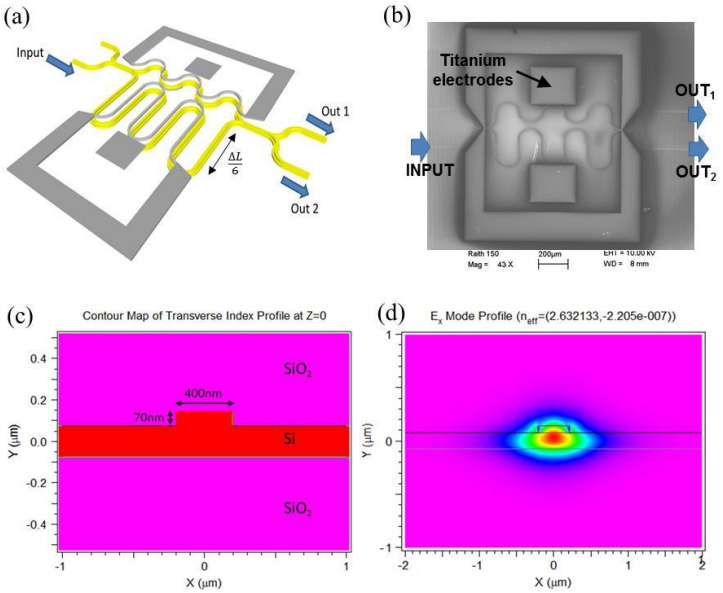

Figure 42: (a) 3D schematic of the a-MZI switching structure where ΔL is the length difference between the MZI arms, (b) SEM image of fabricated device, (c) cross section of the rib waveguide and (d) TE mode profile.

The a-MZI is based on a shallow-etched rib waveguide with 70nm-deep sidewalls. Multimode interferometers have been used at the input and the output of the MZI to split and recombine the signals. The electrodes have a configuration with central fed to achieve a better distribution of the heat from the center to the sides thus obtaining a more gradual change in the refractive index.
In a MZI, the input field is splitted in two signals with the same amplitude. Each signal is guided along its respective arm until the output where they are recombined to generate the output signal. If the interferometer is symmetrical, both signals have been guided through the same optical path. When they are recombined, they are in phase and the input signal is recovered at the output, only disturbed by the losses introduced by the splitters/combiners. On the other hand, if the structure is asymmetrical due to a different length in the arms of the interferometer, each signal goes through a different optical path so they have a different phase when they are recombined. This difference in the phase provokes constructive/destructive interferences as function of the wavelength. For the wavelengths with a constructive interference, the output signal shows low attenuation while for the ones with destructive interference the attenuation is highly increased. Therefore, the obtained output signal is a periodic comb instead of a continuous field like the input signal.

The electric fields of the propagating modes in the different arms of the interferometer are E_1 and E_2 respectively.

$$E_1 = E_0 \sin(\omega t - \beta_1 z)$$
$$E_2 = E_0 \sin(\omega t - \beta_2 z)$$

Where E_0 is the amplitude field and β_1 and β_2 are the propagation constant of each arm. The term $(\beta_2 L_2 - \beta_1 L_1)$ is the phase shift between the signals going through the arms of the interferometer. The lengths of the arms are L_1 and L_2. The phase shift between the guided signals can also be introduced and tuned by the application of an external signal independently if both arms have or not the same length. The phase control is achieved varying the propagation constant of the fields in the waveguides. In this way, controlling externally the phase shift is possible to tune the device to obtain low or high attenuation at the working wavelength.

Figure 43 shows the simulated optical power at both output ports as a function of the wavelength for (a) the symmetric MZI (s-MZI) structure and (b) the a-MZI structure without applying any electrical power. The switching performance in the a-MZI can be understood by looking at the evolution of the transmission spectrum as a function of the applied electrical power. Therefore, Figure 43 shows

also the output optical power as a function of the wavelength for (d) the s-MZI and (e) the a-MZI structures when a normalized electrical power, P/Pπ, of 0.6 is applied. Pπ is the power required for achieving a phase shift of π radians.

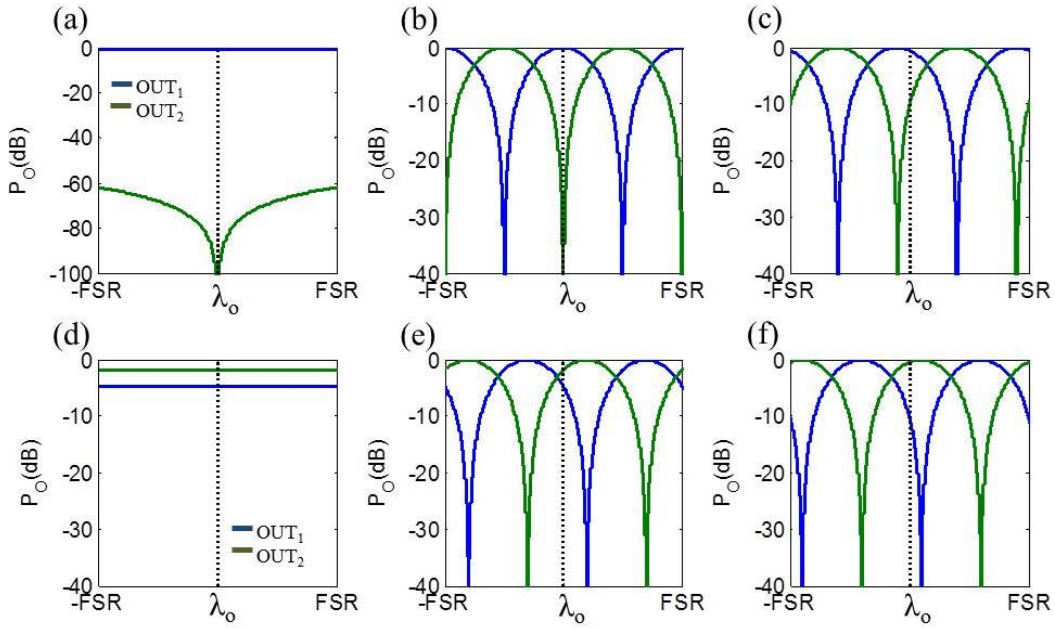

Figure 43: Simulated output optical power as a function of the wavelength for the s-MZI structure and the a-MZI structure with γ=0 and γ=0.2 taking into account a normalized applied electrical power of (a)-(c) P/Pπ=0 and (d)-(f) P/Pπ=0.6 respectively.

It can be seen that the periodic response in the a-MZI structure maintains the same shape but is wavelength shifted. Therefore, by choosing an operation wavelength shifted with respect to the central wavelength, two identical switching states can be achieved with much less electrical power than in the s-MZI, as it is shown in Figure 43(c) and (f). The operation wavelength, λ_o, can be defined as:

$$\lambda_o = \lambda_{max} + \gamma \cdot \frac{FSR}{2}$$

Where λ_{max} is the wavelength at which the maximum output power is achieved in one of ports without applying any electrical power, FSR is the free spectral range of the a-MZI and γ is a design parameter directly related with the reduction in power consumption. The output optical power as a function of the wavelength for the a-MZI structure with γ=0.2 is shown in Figure 43(c) without applying electrical power and (f) applying an electrical power of 0.6Pπ. If γ=0.2 only 0.6Pπ is required to switch from the cross state, shown in Figure 43(c), to the bar state, shown in Figure 43(f). On the other hand, Pπ is always required in the s-MZI, as well in the a-MZI with γ=0, to complete the switching because otherwise high

insertion losses and unacceptable crosstalk would be given in the bar state, as it can be seen in Figure 43(d) and (e) respectively.

The percentage of power consumption reduction in the a-MZI is around two times the γ-parameter (for example the required electrical power has been reduced in a 40% when the γ-parameter is 0.2). However, it can also be seen in both Figure 43(c) and (e) that there is a penalty on insertion losses and crosstalk. Such penalty as a function of the γ-parameter is depicted in Figure 44. It can be seen that the influence on the insertion losses is almost negligible while a low crosstalk can also be achieved. Using a γ-parameter below 0.25, insertion losses below 1dB and crosstalk values above 10dB will be achieved.

It is important to notice that the change in the operation wavelength only implies that the optical response of the a-MZI switch would be designed to fit with the wavelengths used in the system. Therefore, once λo is defined and λmax is obtained, they are used to calculate

$$N = \frac{2n_{eff}\lambda_{max}}{n_g FSR}$$

Where n_{eff} and n_g is the effective and group indices of the optical waveguide. In such a way, the required length difference, shown in Figure 42(a), will be obtained as

$$\Delta L = \frac{N_{even}\lambda_{max}}{2n_{eff}}$$

Where N_{even} is the closest even integer to N. In our case, the group index is 3.619 and λ_{max} has been set to 1550nm so to achieve a free spectral range of 100GHz, the required length difference between the arms of the a-MZI is 830μm.

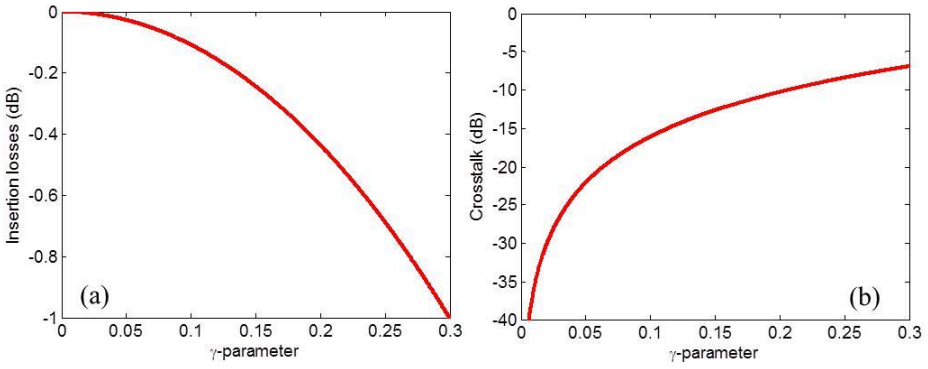

Figure 44: Penalty on (a) insertion losses and (b) crosstalk as a function of γ-parameter in the proposed a-MZI switching structure.

System simulations have also been carried out to analyze the influence of the a-MZI spectral response on the switching performance. Simulations have been done in Matlab© and considering white Gaussian noise and a non-return-to-zero (NRZ)

digital signal. The bit error rate (BER) in the s-MZI as a function of the applied electrical power (normalized by P_π) is shown at both output ports in Figure 45(a). The FSR is 100GHz, the bit rate of the digital signal is 10Gbps and the signal to noise ratio (SNR) is 13dB. The response of the outputs is complementary and there are two different states. Without applying any power, the cross state, output one (OUT_1) is in error free level (lower than 10^{-9}) while output two (OUT_2) has a very high BER level. It means that almost all the input signal is switched to OUT_1 port and only a negligible portion is undesirably switched to OUT_2 port due to the crosstalk. By applying P_π, the bar state, the switching is reversed and the input signal is now switched to OUT_2 port so the output signal is in error free.

Figure 45(b) shows the BER as a function of the normalized applied electrical power in the a-MZI switch at both output ports and for different values of the γ-parameter. The red dotted line is for γ=0 so the a-MZI is working at the central wavelength and the switching response is almost identical to that of the s-MZI depicted in Figure 45(a). Therefore, the required power to complete the switching in the a-MZI is also P_π. However, when the γ-parameter is increased to 0.1 (green dotted line), the switching from the error free level to a high error level is accomplished with around a 20 percent less power consumption. It is important to notice that the same error levels at both output ports are required at the two switching states, i.e. $P/P_\pi=0$ and $P/P_\pi=0.8$ for γ=0.1, to have the same conditions of insertion losses and crosstalk. On the other hand, for an applied electrical power equal to zero, the BER is a bit higher than for γ=0 but it is still in error free confirming that the impact on insertion losses is almost negligible. For γ=0.2 (blue line), a significant power reduction of around 40% is achieved as only $P/P_\pi=0.6$ is required for switching between the two states.

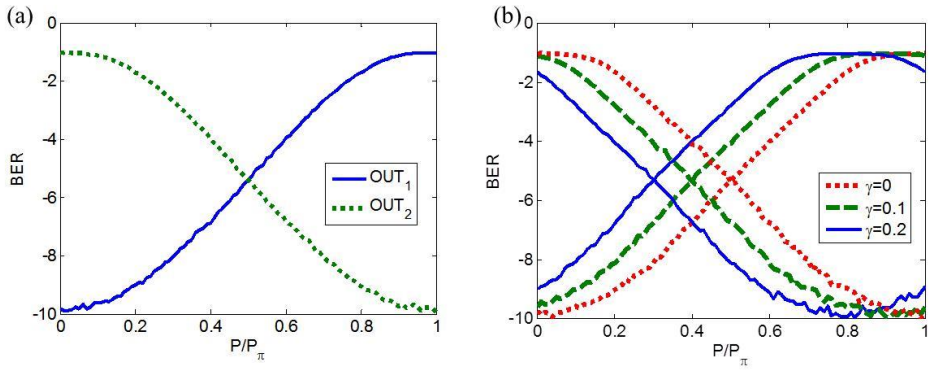

Figure 45: Simulated BER as a function of the normalized applied electrical power for (a) the s-MZI and for (b) the a-MZI for different γ-parameter values.

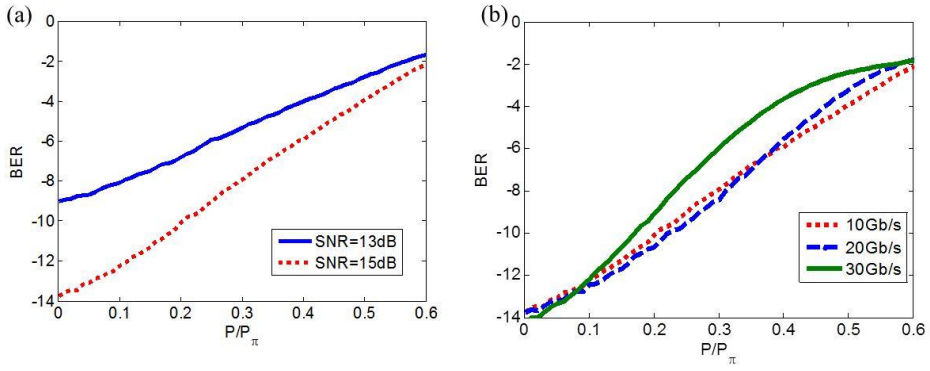

Figure 46: Simulated BER as a function of the normalized applied electrical power for the a-MZI with γ=0.2 and different values of (a) signal-to-noise ratio and (b) data bit rate.

The influence of other parameters like the SNR or the bit rate has also been also analyzed. Figure 46(a) shows that, for a fixed value of γ=0.2 and a bit rate of 10Gbps, increasing the SNR from 13 to 15 improves the BER level at the cross state, i.e. $P/P_\pi=0$, but it is important to notice that this does not mean a reduction in power consumption because a high error level must be achieved for complete switching to the bar state. Therefore, $0.6P_\pi$ is always required for γ=0.2 to switch between the bar and cross states independently of the SNR value. On the other hand, Figure 46(b) shows the influence of the bandwidth of the signal for a fixed FSR of 100GHz, a SNR of 15 and γ=0.2. When the bit rate is increased, higher values of BER may be achieved with a lower applied electrical power due to the filtering effect of the spectral response of the a-MZI structure but in the end the amount of power to complete the switching is again the same independently of the bit rate. Therefore, adjusting the FSR as a function of the bit rate does not provide a reduction in power consumption but it is interesting for introducing several channels simultaneously. It should be noticed that by inserting several channels in the pass bands of the a-MZI, a wide optical bandwidth can be achieved as it has also been proposed for ring based switches [69].

3.1.2. Experimental results.

The a-MZI switch has been fabricated to experimentally demonstrate the proposed approach to reduce the power consumption. In order to avoid any influence of the electrodes, the same structure has been measured and compared at the central wavelength, in which the performance is like in a s-MZI, and working with different operation wavelengths. The device was fabricated on standard SOI samples of SOITEC wafers with a top silicon layer thickness of 220nm and a buried oxide layer thickness of 2μm. The structure fabrication is based on an electron beam direct writing process performed on a coated 100nm

hydrogen silsesquioxane (HSQ) resist film. After developing the HSQ resist using TMAH as developer, the resist patterns were transferred into the SOI samples employing an also optimized Inductively Coupled Plasma- Reactive Ion Etching process with fluoride gases (SF_6/C_4F_8). The etching process was optimized to reach 70nm deep structures (rib waveguides). Once the silicon is etched, the samples were covered with 0.7 microns of silicon dioxide deposited by means of PECVD tool. Finally, Titanium microheaters were placed on the tuning structures by evaporation and a lift-off process.

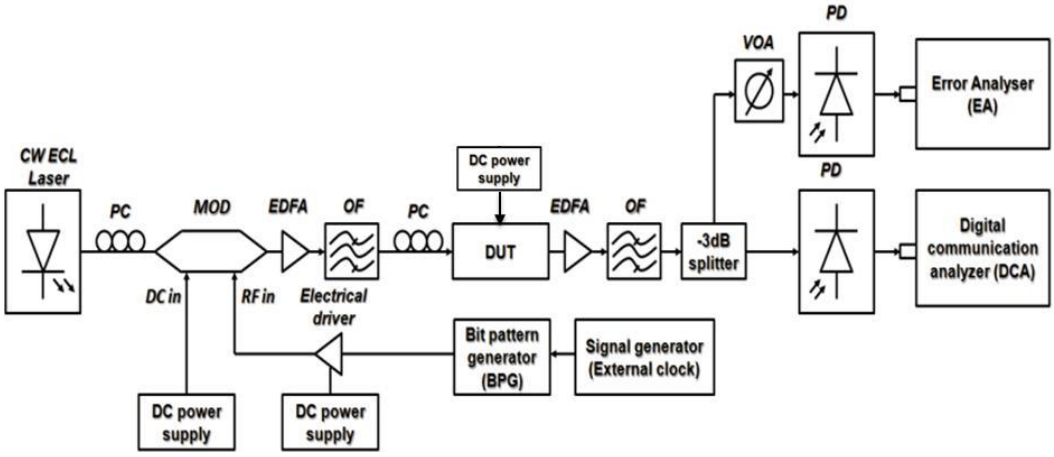

Figure 47: Experimental set-up. The laser signal is modulated by an electrical pattern and applied to the device under test (DUT). Finally, the signal is guided to the error analyzer and the digital communication analyzer.

Figure 47 illustrates the experimental set-up. A commercial $LiNbO_3$ modulator fed with a 10-30Gbps NRZ pseudo-random bit sequence (PRBS 2^{31}-1) delivered by a bit pattern generator is used. The electrical signal was amplified through a broad bandwidth driver amplifier (DC to 40 GHz) to achieve a voltage swing of ~5 Vpp and combined to a 1.7 V DC offset to ensure the modulator is biased at quadrature. The input modulated signal was amplified and filtered with an optical filter of 3nm to decrease the noise introduced by the EDFA. Then, the signal was coupled in and out the silicon chip via grating couplers. An EDFA after the device amplifies its output signal and a 3dB splitter divides the power for simultaneously measuring the eye diagram and the BER. The signal was then photodetected by a 40 GHz Digital Communication Analyzer to see the eye diagram and the BER was measured by means of a 75 GHz photodiode connected to the Error Analyzer and evaluated as a function of the electrical power applied to the device under test (DUT).

Several measurements of the BER value as function of the applied electrical power to the electrodes have been carried out. First, the a-MZI switch has been characterized at the central wavelength of the spectral response, as it was depicted

in Figure 43(b). BER measurements as a function of the applied power normalized by Pπ are shown in Figure 48(a) for bit rates between 10 to 30Gbps and γ=0. Without applying electrical power, error free performance was achieved for all the bit rates under study. If the bit rate of the signal increases, higher BER values are achieved for electrical powers above 0.5Pπ, in agreement with simulations results depicted in Figure 46(b). However, it is important to remind that this does not mean that power consumption is lower because to complete the switching an electrical power of Pπ is required.

The switching performance has been compared with the device working at different operation wavelengths. Results are shown in Figure 48(b)-(d). It can be clearly seen that, for a certain bit rate, the same value of BER is achieved with an important reduction in the applied electrical power. For example, in Figure 48(b), to obtain a variation from error free to 10^{-4} BER level by using γ=0.24 and a bit rate of 10Gbps, the power reduction comparing with the same structure working at the central wavelength (γ=0) is around 50% in agreement with simulation results. Figure 48(c) and (d) show that the power reduction is lower, independently of the used bit rate, when the γ-parameter is decreased. A power reduction of around 40% is demonstrated for γ=0.2 and around 32% for γ=0.16, which is once more in agreement with simulation results. In our device, a Pπ power of 36mW was measured. Therefore, the proposed approach would allow reducing the power consumption up to 18mW with respect to a conventional s-MZI switch.

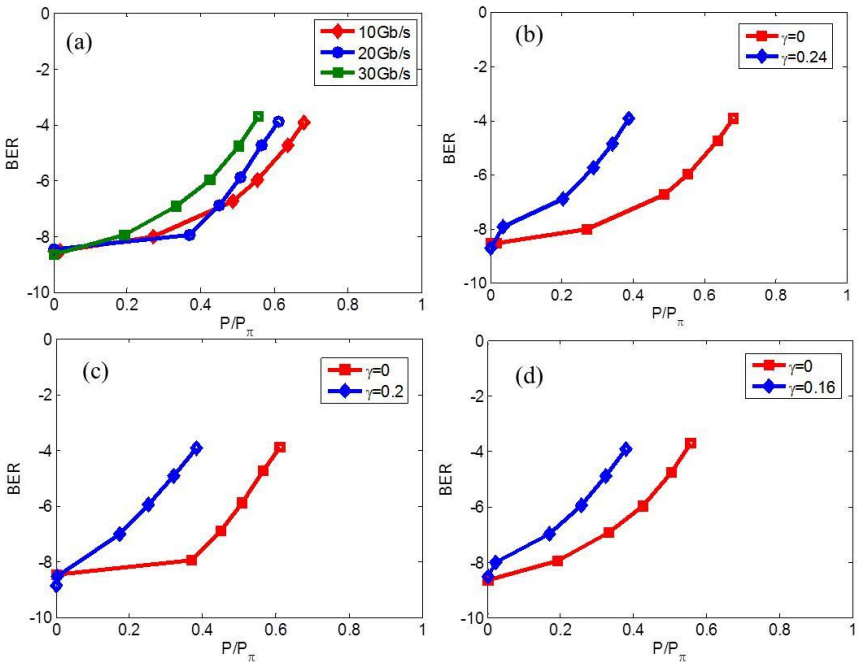

Figure 48: BER as function of the normalized applied power for (a) γ=0 and different bit rates, (b) 10Gbps, (b) 20Gbps and (c) 30Gbps.

In summary, a novel approach has been proposed, analyzed by means of simulations and experimentally demonstrated to decrease the power consumption in silicon switches. The switch is based on an asymmetric MZI structure and operated with a conveniently chosen wavelength. The latter only implies that the optical response of the a-MZI switch would be designed to fit with the wavelengths used in the system. A power consumption reduction up to 50% has been demonstrated which could open a new path for energy efficient switching in silicon via the thermo-optic effect.
This work was published in Photonics Journal [70], in the international conference SPIE Photonics Europe 2014 [71] and in the 11th International Conference on Group IV Photonics 2014 [72].

3.2. Optical switching controlled by vanadium dioxide.

The structures proposed for hybrid VO_2/Si optical switches have been based on a one input/ one output (1x1) configuration. In the next sections, the analysis and design optimization of a 2x2 microring switch based on a hybrid VO_2/silicon waveguide structure is reported. Active performance is based on the VO_2 SMT so that a change in optical absorption losses and phase shift is achieved due to the complex nature of the refractive index. Switching is achieved by exploiting the change in absorption loss but also taking advantage of the induced phase shift to enhance the performance. Thus, insertion losses below 1.8 dB and crosstalk values above 12 dB are achieved in a compact switching device with an active length as low as 2.8μm and a footprint below 100μm^2.

3.2.1. Analysis of the 2x2 optical switching structure.

Figure 49 shows a concept art of the proposed 2x2 switch based on a conventional add-drop microring resonator structure for the (a) insulating and (b) metallic VO_2 states. The structure is symmetric so the transmission coefficient of the ring is the same at both coupling sections.

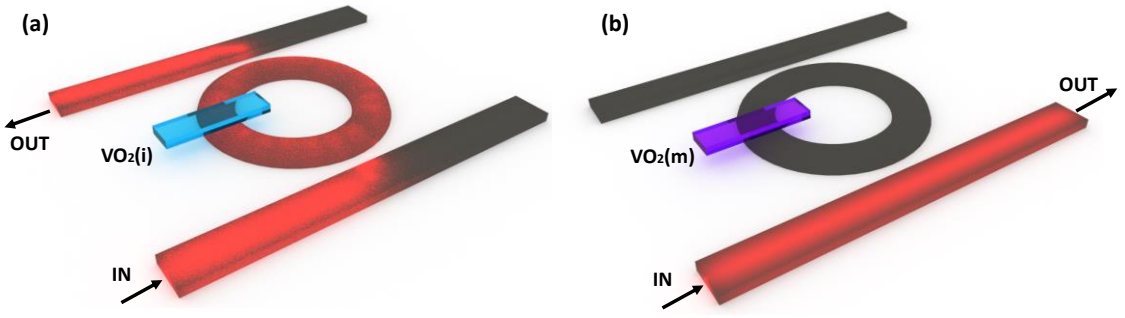

Figure 49: Concept art of the 2x2 hybrid VO_2/Si switch based on an add-drop microring resonator for (a) the insulating and (b) metallic states.

As a difference with rings based on other materials, silicon rings can maintain the field confined inside rings with extremely small radii because of the high index contrast of the SOI platform. Reducing the radius of the ring provides wider FSR which is crucial in several applications.

In an add-drop ring resonator, the power of the resonance dips in the transmission of the through port is coupled to the drop port. It means, that the signals of both output ports have a comb response but they are complementary between them. The device depicted in Figure 49 switches between the bar and cross states by exploiting the change of the VO_2 complex refractive index. The normalized power at the output port and the crosstalk can be calculated by [73],

$$P_{out} = \frac{a_i(1-t^2)^2}{1-2t^2a_i cos\phi_i + (t^2a_i)^2}$$

$$P_{crosstalk} = \frac{t^2a_i^2 - 2t^2a_i cos\phi_i + t^2}{1-2t^2a_i cos\phi_i + (t^2a_i)^2}$$

Where t is the transmission coefficient, $\emptyset_i$ is the phase shift and a_i is the amplitude losses in the ring for the insulating state.
The switch operates in two different states depending on the VO_2 phase:

- Cross state (Figure 49(a)): In this switching state, the field must be coupled to the ring and goes through the hybrid section of the ring. Hence, to achieve a low value of ring losses the VO_2 is in its insulating state. Furthermore, low values of the transmission coefficient are favorable to achieve low insertion losses and low crosstalk.
- Bar state (Figure 49(b)): In this state, the field must not be propagated across the ring so high losses are desirable. Therefore, the VO_2 is in its metallic state. In contrast with cross state, high values of the transmission coefficient help to achieve low insertion losses and low crosstalk.

Figure 50(b) shows the normalized output power and crosstalk in the cross state for a value of $A_i = 20\log_{10}(a_i) = 0.5$dB and a transmission coefficient of 0.88. It can be seen that the lowest insertion losses and highest crosstalk are obtained by placing the input optical signal at the ring resonance ($\emptyset_i = 0$).

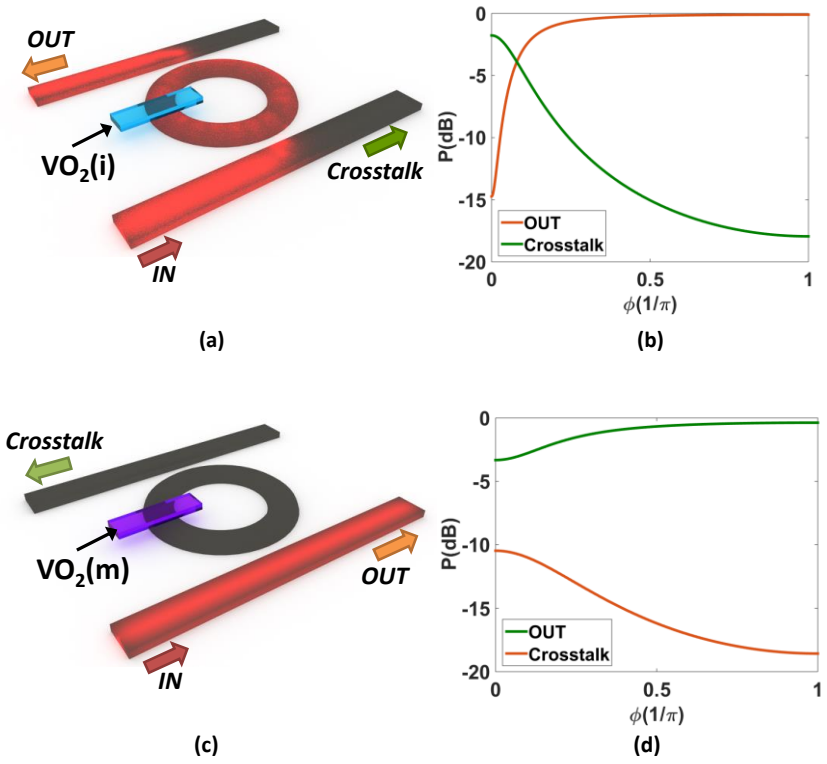

Figure 50: Switch operation in the cross state (a,b) and bar state (c,d). Transmission response as a function of the phase shift taking into account t=0.88 and losses in the ring of 0.5dB (b) and 5dB (d).

On the other hand, in the bar state, shown in Figure 50(c), the VO_2 is in its metallic state. Therefore, losses in the ring are increased to a_m due to the variation of the imaginary part of the refractive index. In this case, the output power of the switch and the crosstalk are calculated exchanging the expressions taking into account the new ring loss value of a_m. Low insertion losses and high crosstalk can also be achieved as it can be seen in Figure 50(d), which depicts the switching performance for a value of $A_m = 20\log_{10}(a_m) = 5\text{dB}$ and the same transmission coefficient than in Figure 50(b). It should be noticed that the change in the real part of the VO_2 refractive index will give rise to a phase shift difference with respect to the insulating state ($\emptyset_m > \emptyset_i$) that will contribute to improve the insertion losses and crosstalk in the switch, as it can be seen in Figure 50 (d).The same insertion losses are desirable for both switching states which can be achieved by conveniently designing the transmission coefficient of the ring structure. Figure 51 shows the insertion losses and crosstalk as a function of the transmission coefficient for the same cross ($\emptyset_i = 0$, $A_i = 0.5\text{dB}$) and bar ($\emptyset_m = 0.2\pi$, $A_m = 5\text{dB}$) states considered in Figure 50(b) and (d), respectively. It can be seen that there is a transmission coefficient value, t=0.88 in Figure 51(a), that allows obtaining the same insertion losses at both switching states although the crosstalk level is slightly different. It is interesting to notice that there is also a different

transmission coefficient that provides the same crosstalk level, as it can be seen in Figure 51(b).

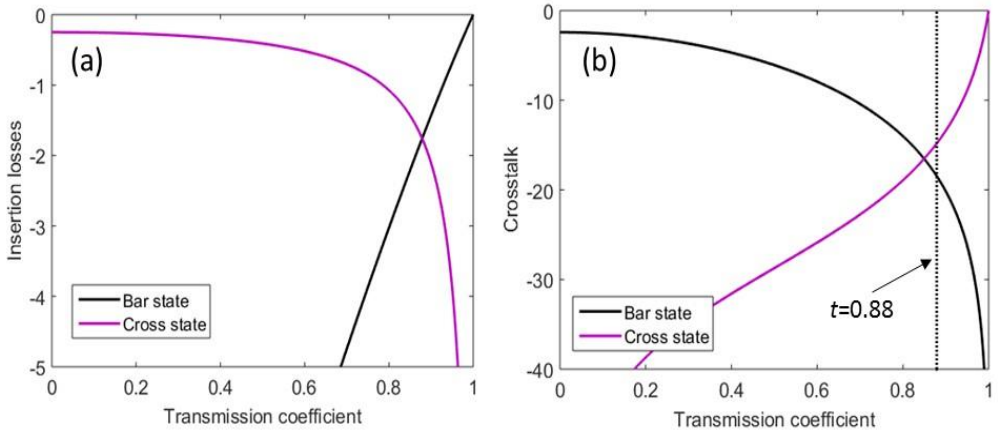

Figure 51: (a) Insertion losses and (b) crosstalk level as function of the transmission coefficient taking into account $\emptyset_i = 0$ *and* $A_i = 0.5dB$ *for the cross state and* $\emptyset_m = 0.2\pi$ *and* $A_m = 5dB$ *for the bar state.*

As it was shown before, switching can be achieved by only varying the losses in the ring. Figure 52 shows the insertion losses and transmission coefficient depending on the loss difference ($\Delta\alpha = A_m - A_i$) between the bar and cross states by assuming that the phase shift is zero ($\Delta\emptyset = \emptyset_m - \emptyset_i = 0$).

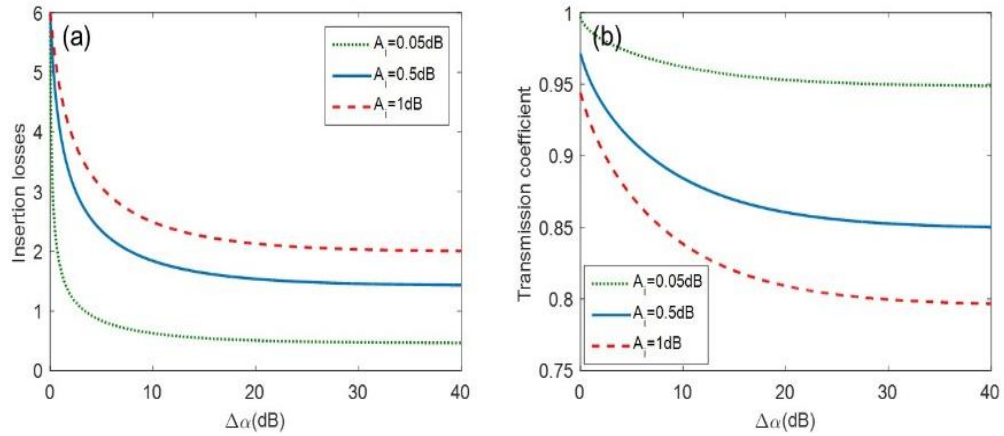

Figure 52: (a) Insertion losses and (b) transmission coefficient as a function of the ring loss difference ($\Delta\alpha$) *between the bar and cross states by assuming that the phase shift variation is zero* ($\Delta\emptyset = 0$).

It can be seen that low insertion losses can be achieved by only varying the ring losses between the two switching states. However, there is a bound in the lowest insertion loss that is determined by the ring loss in the cross state (A_i). Insertion losses below 1.5dB can be achieved if the ring loss in the cross state is 0.5dB, which is possible to achieve with the value of the VO_2 refractive index in the

insulating state. Lower insertion losses can be achieved by reducing the ring loss at the cross state but then a higher transmission coefficient will be required that will decrease the bandwidth of the ring resonance and therefore the optical bandwidth of the switch.

Figure 53 shows the switching performance as a function of the ring loss difference between the bar and cross states by considering that the ring loss in the cross state is 0.5dB. Furthermore, the impact of having an additional phase shift is also depicted. It can be seen that if the loss difference is large enough ($\Delta\alpha > 20dB$), low insertion losses and high crosstalk at both switching states are achieved without requiring any phase shift and for a transmission coefficient around 0.85. In fact, the influence of the phase shift in the switching performance is negligible. However, a good performance can also be achieved with a lower loss difference if there is a certain phase shift, for instance $\Delta\emptyset = 0.25\pi$ as it is shown in Figure 53. Insertion losses below 1dB are only achieved by having a π-phase shift and keeping the loss difference below 7dB. In this case, it should be noticed that negligible losses are not desired as then crosstalk will increase at the bar state.

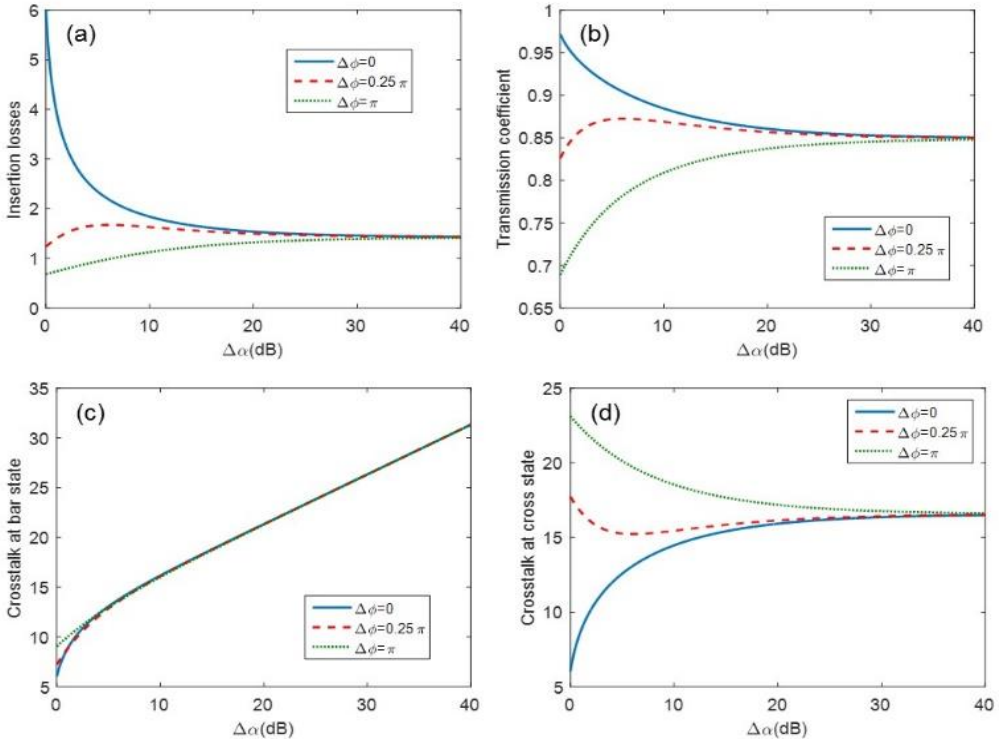

Figure 53: (a) Insertion losses, (b) transmission coefficient (c) crosstalk at bar state and (d) crosstalk at cross state as a function of the ring loss difference between the two switching states. The ring loss in the cross state is A_i*=0.5dB.*

Therefore, the optimum hybrid VO_2/Si waveguide is designed by exploiting both the loss difference and phase shift variation between the insulating and metallic

states. On the other hand, the active length is determined to ensure that losses in the insulating state are 0.5dB.

3.2.2. Waveguide design.

Once the behavior of the 2x2 microring switch based on a hybrid VO_2/silicon structure has been studied in the previous section, the first target is to achieve a waveguide structure with single-mode transmission and low losses. The considered waveguide structures are shown in Figure 54. In all cases, a standard silicon-photonic SOI-substrates consisting of a 220nm thick top-silicon layer is considered and, as a first approach, the vanadium dioxide film has a thickness of 70nm with a refractive index of 3.21+0.17i in the insulating phase and 2.15+2.79i in the metallic phase at λ=1550nm [49]. In this initial approach, electrodes are not considered so the waveguide are surrounded by silica.

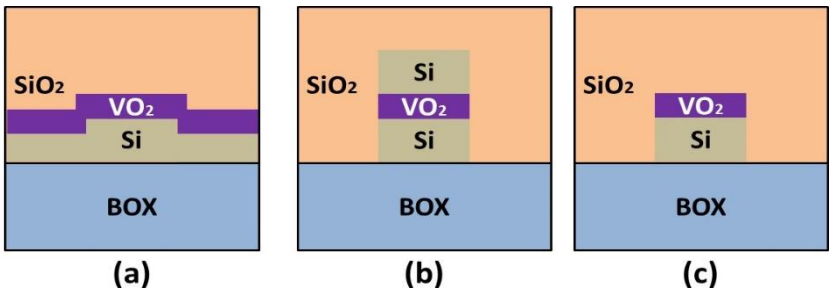

Figure 54: Proposed waveguides; (a) shallow etched, (b) vertical slot and (c) rib. As a first approximation, the waveguides are considered surrounded by silica.

In Figure 55(a), the silicon waveguide is only shallow etched to allow a direct thin-film VO_2 deposition on top of it, therefore reducing the number of fabrication steps. For a width of 500nm and an etching depth of 70nm, Figure 55 shows the TE mode profiles for the waveguide (a) without vanadium dioxide and covered with a 70nm thick VO_2 film in the (b) insulating and the (c) metallic states.

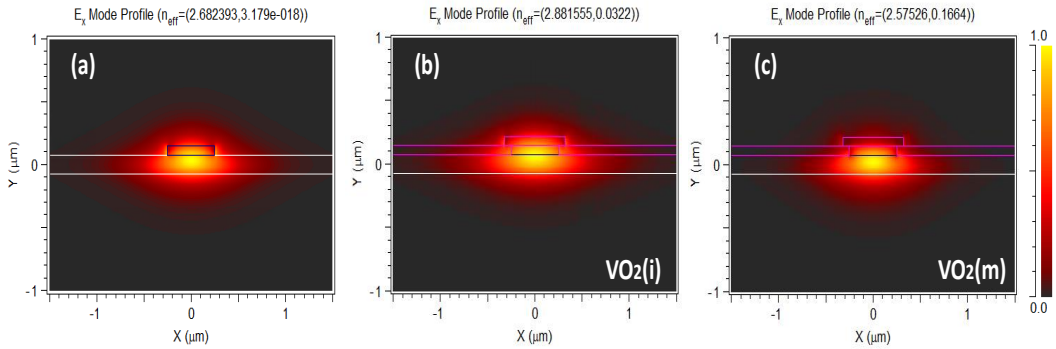

Figure 55: TE mode profiles for a 500nm-wide VO_2/Si shallow etched waveguide (a) without vanadium dioxide, and with a layer of 70nm of vanadium dioxide in (b) insulating and (c) metallic states.

Two main points have to be considered from the comparison of the effective refractive index of the modes for both vanadium dioxide states. First, the variation in the real part of the effective refractive index (Δn_{eff}) determines the active length to achieve the phase shift of π radians (L_π):

$$L_\pi = \frac{\lambda}{2 \cdot \Delta n_{eff}}$$

From the imaginary part of the effective index of the modes, the losses in dB/μm have been obtained using the next equation:

$$\alpha\left(\frac{dB}{\mu m}\right) = 10 \cdot \log(e) \cdot \left(\frac{4 \cdot \pi \cdot k}{1.55}\right) \approx 35.2 \cdot k$$

And the total losses for the L_π length has been calculated as:

$$a(dB) = \alpha\left(\frac{dB}{\mu m}\right) \cdot L_\pi(\mu m)$$

According to these equations and the modes depicted in Figure 55, the waveguide has been characterized as function of the VO_2 phase and summarized in Table 6.

Table 6: Characterization of the shallow etched waveguide for TE polarization.

TE	n	k	$\alpha\left(\frac{dB}{\mu m}\right)$	Δn_{eff}	$L_\pi(\mu m)$	$a(dB)$
Insulating state	2.881	0.0322	1.13	0.306	2.53	2.86
Metallic state	2.575	0.1664	5.86			14.82

Compact active lengths can be achieved with moderate losses. In the case of a 500nm-wide waveguide, a $L\pi$ of $2.53\mu m$ can be achieved while the total losses for the metallic and insulating states will be 14.8dB and 2.86dB respectively. However, the main limitation of this waveguide for our ultra-compact switching structure is that small bending radii are not supported. Figure 56 clearly shows that light is not confined in a bend with 3.5μm radius. The simulation was carried out by 3D-FDTD with the Fullwave package of RSoft software.

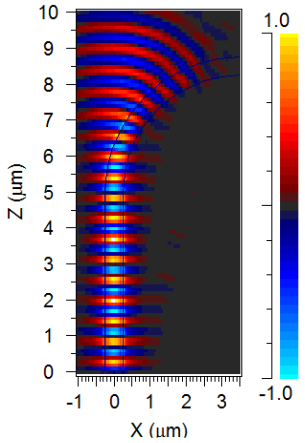

Figure 56: Simulation of light propagation in a bend with 3.5µm radius. The radius is too small for this waveguide structure and the field is not confined inside the bend.

The structure shown in Figure 54(b) exploits the slot concept to maximize the optical confinement. Figure 57 shows the different mode profiles of the slot waveguide when the material between the silicon waveguides is silica and when it is vanadium dioxide in its both states. In several applications, for example in electro-absorption devices, a maximum confinement of optical power in the VO_2 layer to take the maximum profit of its changes due to the SMT is desirable. As the change that can be achieved in the VO_2 refractive index is also extremely high, devices can be made so that the total losses will not limit the performance.

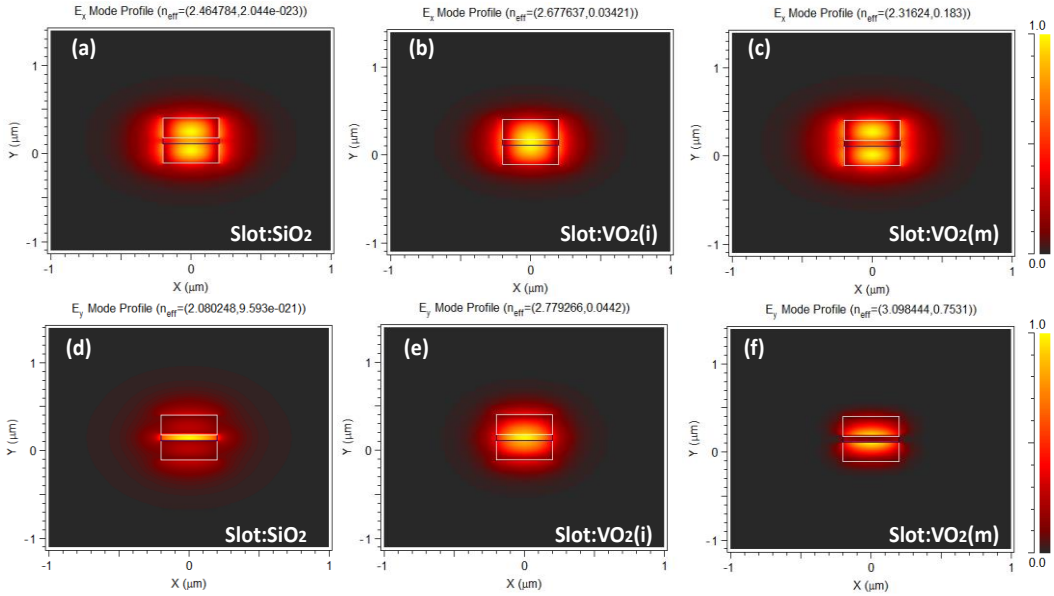

Figure 57: (a,d) TE and TM mode profiles for a 400nm-wide slot waveguide with silica as the centered material. (b,c) TE and (e,f) TM mode profiles for a VO_2/Si slot waveguide for the insulator state and the metallic states respectively.

The great confinement inside the slot allows for small bending radii. Figure 58 show the same mode profiles depicted in Figure 57 but considering a radius of 3.5µm. Doing a comparison, it is clearly seen that the losses introduced by the bends are negligible.

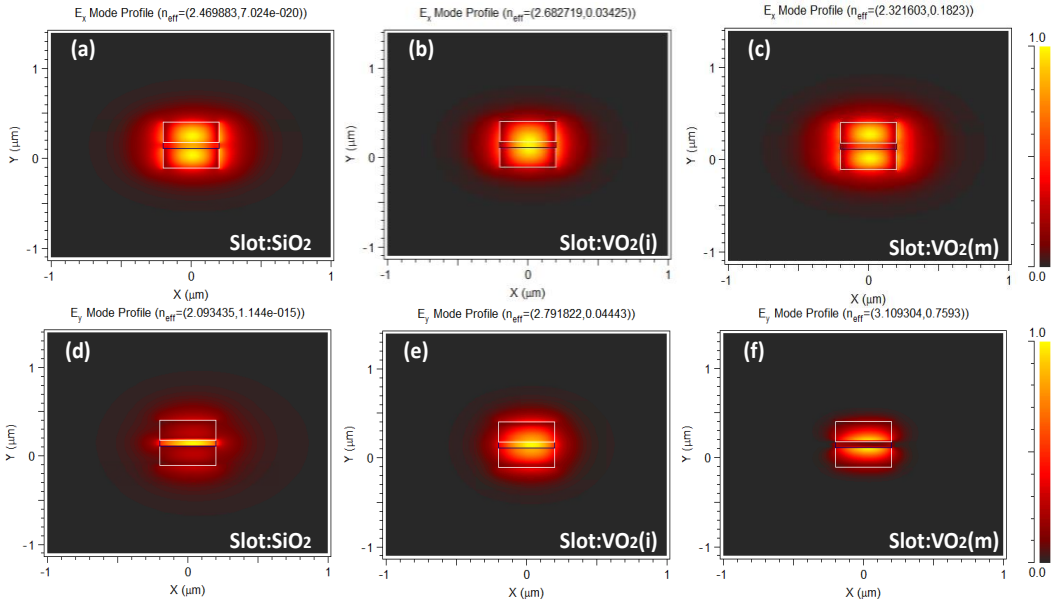

Figure 58: Bend mode profiles for 3.5µm radius calculated by conformal transformation. (a,d) TE and TM mode profiles for a 400nm-wide slot waveguide with silica as the centered material. (b,c) TE and (e,f) TM mode profiles for a VO_2/Si slot waveguide for the insulator state and the metallic states respectively.

Table 7 and Table 8 summarizes the main results obtained for the slot structure considering both VO_2 states. It is especially remarkable that for TM polarization there is a huge absorption increment when the vanadium dioxide is switched to its metallic state. In fact, the slot structure with TM polarization would be a very useful solution for an electro-absorption application.

Table 7: Characterization of the slot waveguide for TE polarization.

TE	n	k	$\alpha\left(\frac{dB}{\mu m}\right)$	Δn_{eff}	$L_\pi(\mu m)$	$a(dB)$
Insulating state	2.677	0.034	1.19	0.361	2.14	2.55
Metallic state	2.316	0.183	6.44			13.8

Table 8: Characterization of the slot waveguide for TM polarization.

TM	n	k	$\alpha\left(\frac{dB}{\mu m}\right)$	Δn_{eff}	$L_{\pi}(\mu m)$	$a(dB)$
Insulating state	2.779	0.044	1.55	0.319	2.43	3.76
Metallic state	3.098	0.753	26.51			64.4

Nevertheless, for both polarizations, even in the insulating state, the losses due to the confinement in the vanadium dioxide are not negligible. Considering this, to avoid an excess of losses in the structures, the VO_2 cannot be present in the entire sample and must be necessarily etched away from the unwanted regions. Structures, like the proposed in Figure 59, to excite the slot mode are required and it would introduce additional fabrication steps.

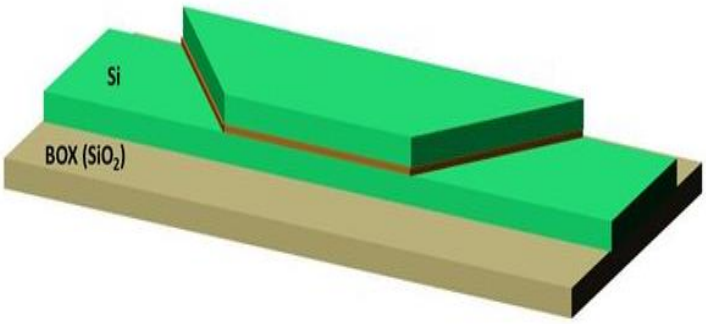

Figure 59: (d) Proposed coupler structure for coupling from a conventional silicon waveguide into and out of the VO_2/Si slot waveguide.

Finally, the deep etched structure shown in Figure 54(c) is analyzed. A silicon waveguide with a cross section 480x220nm ensures singlemode transmission for both polarizations. The mode profile for TE polarization is shown in Figure 60(a) while the mode profile for TM polarization is shown in Figure 60(c). In contrast with the shallow etched structure, for TE polarization negligible bend losses for 3.5µm radius have been obtained by conformal transformation (Figure 60(b)). On the other hand, bend losses of 0.07dB/µm (total losses of 1.5dB for a ring with 3.5µm radius) have been obtained for TM polarization (Figure 60 (d)). The bend losses values obtained by conformal transformation have also been confirmed by means of 3D-FDTD simulations.

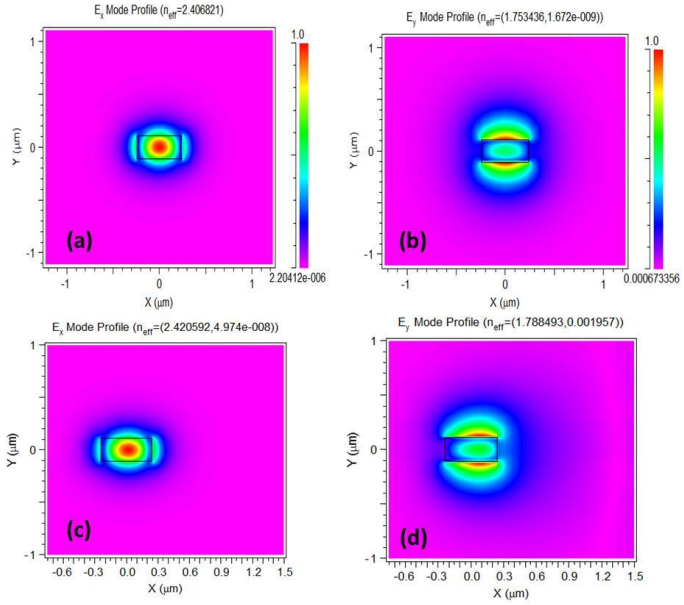

Figure 60: Mode profile for (a) TE and (c) TM polarizations in the deep etched structure for a waveguide width of 480nm. Bend mode profile for 3.5µm radius calculated by conformal transformation for (b) TE and (d) TM polarizations.

The influence of a spacer between the silicon waveguide and the VO_2 film has been analyzed in a first step taking into account a VO_2 film thickness of 70nm. Figure 61 shows as a function of the thickness of the spacer for TE polarization and a wavelength of 1550nm; (a,b) the real and imaginary part of the effective refractive index for both states, (c) the variation of the effective refractive index (Δn_{eff}) due to the change of the VO_2 film between its two different states, (d) the length to achieve the phase shift of π radians (L_π) and (e,f) the propagation losses in dB/µm and total losses for the L_π length respectively. If the spacer is thin, the VO_2 interacts more with the field and high values of Δn_{eff} are obtained and thus shorter L_π lengths, as it is shown in Figure 61(c) and (d). The impact of the spacer thickness on the total losses, Figure 61(f), is relatively small. The lowest losses in the insulating state are obtained when the VO_2 film is directly deposited on the silicon waveguide. However, even in this case, losses around 2.8dB are obtained due to the high value of the imaginary part of the refractive index of the VO_2. On the other hand, the losses in the metallic state are slightly higher when the spacer thickness decreases.

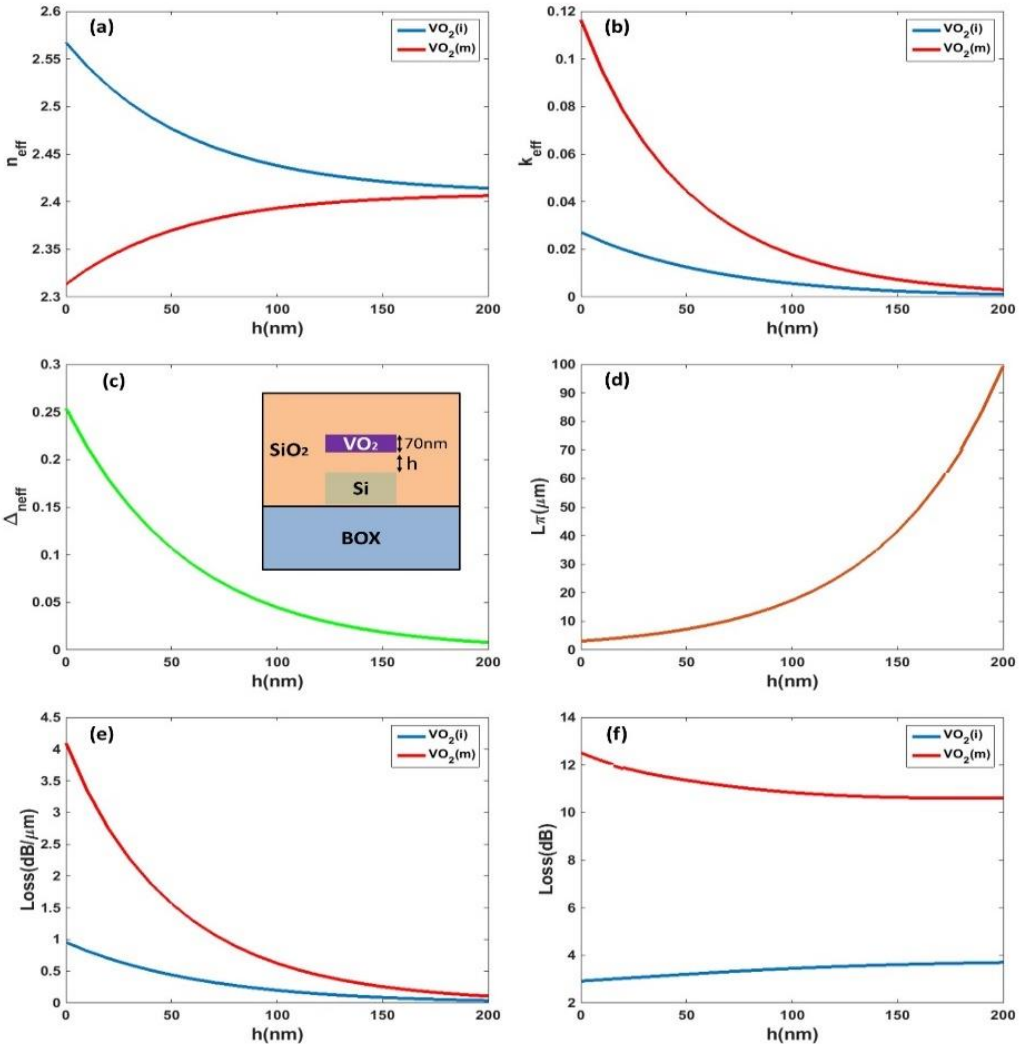

Figure 61: For TE polarization, (a,b) real and imaginary part of the effective refractive index for both states. (c) Δneff and (d) Lπ length for a wavelength of 1550nm as a function of the spacer thickness for the waveguide structure shown in the inset. (e) Propagation losses for both VO_2 states and (f) total losses for the Lπ length.

The influence of the VO_2 film thickness has also been studied. Assuming that the refractive index of the VO_2 does not change with the film thickness, simulations of the waveguide structure have been carried out to study the effect on the L_π length and losses. Figure 62 shows the obtained results. The spacer thickness has been set to h=0nm. By reducing the thickness of the VO_2 film, the Δn_{eff} decreases because there is a smaller interaction with the active material and therefore the L_π length increases, as it is shown in Figure 62(c) and (d). It is interesting to notice that the total losses in the metallic state, Figure 62(f), increase due to a longer L_π length despite the propagation losses are smaller for thinner VO_2 films. The opposite performance occurs for the insulating state in which the total losses decrease for thinner VO_2 films. However, for a radius of 3.5μm, the maximum L_π

length is 22µm which means that the thickness of the VO_2 film must be above 10nm. Therefore, for such value, the total losses in the insulating state can be slightly reduced to 2.3dB. In any case, it can be seen that the impact of the VO_2 film thickness on the total losses in the insulating state is also relatively small.

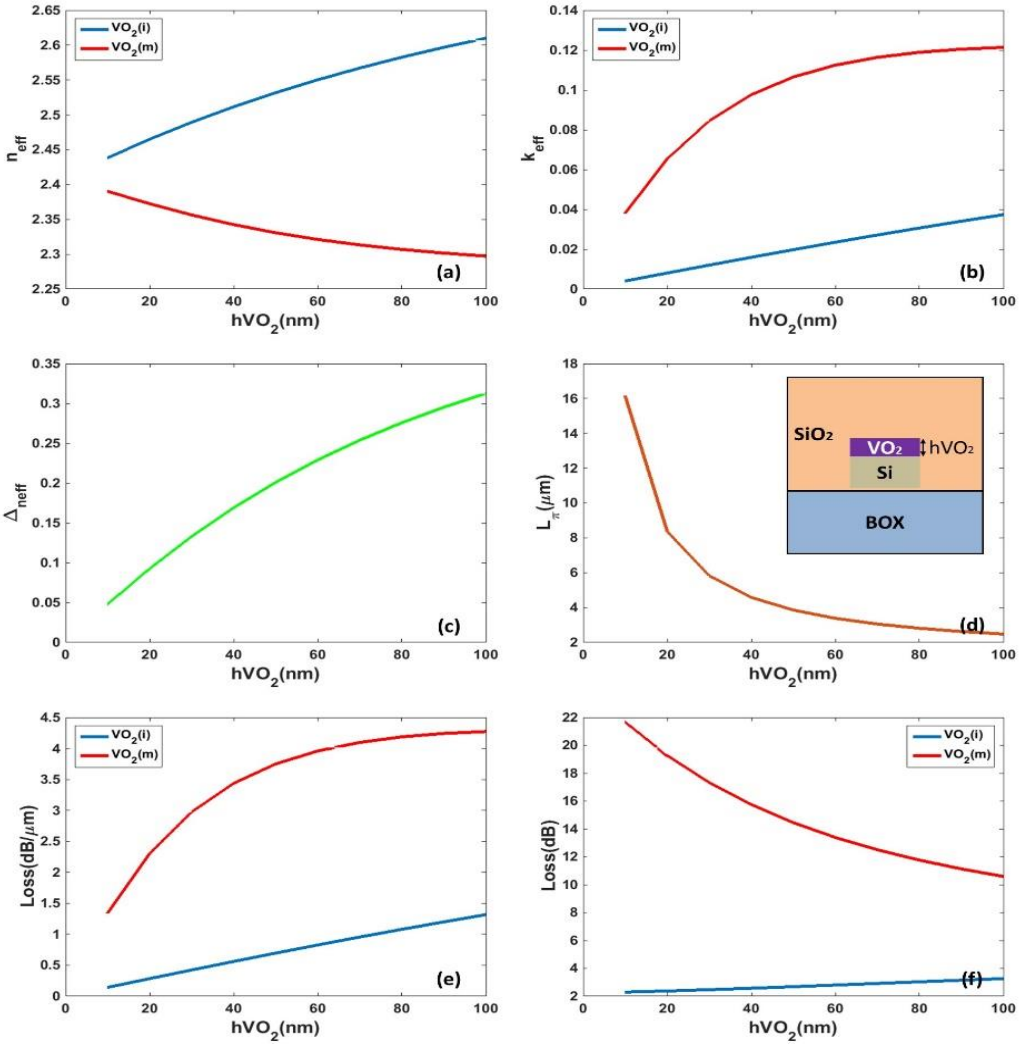

Figure 62: (a,b) Real and imaginary part of the effective refractive index for both states. (c) $\Delta neff$ and (d) resultant $L\pi$ for a wavelength of 1550nm as a function of the VO_2 film thickness for the waveguide structure shown in the inset. (c) Propagation losses for both VO_2 states and (d) total losses for the $L\pi$.

The influence of the VO_2 film on top of the deep etched waveguide structure has also been analyzed for TM polarization. Figure 63 shows the obtained results as a function of the spacer thickness taking into account a VO_2 film thickness of 70nm. As for TE polarization, the Δn_{eff} decreases as the spacer thickness increases giving rise to longer L_π lengths. However, it can be seen that an extremely short L_π length of 4.5µm can be achieved for a spacer thickness of 30nm due to a much higher value of Δ_{neff} with respect to TE polarization. The propagation losses for

both states decrease for thicker spaces but the L_π length increases because Δ_{neff} decreases. It implies that the total losses are reduced for thinner spacers. For a 30nm spacer, a minimum total losses of 2.9dB in insulating state can be achieved. On the other hand, the propagation losses in the metallic state are much higher than for TE polarization. This difference could be highly exploited in electro-absorption applications.

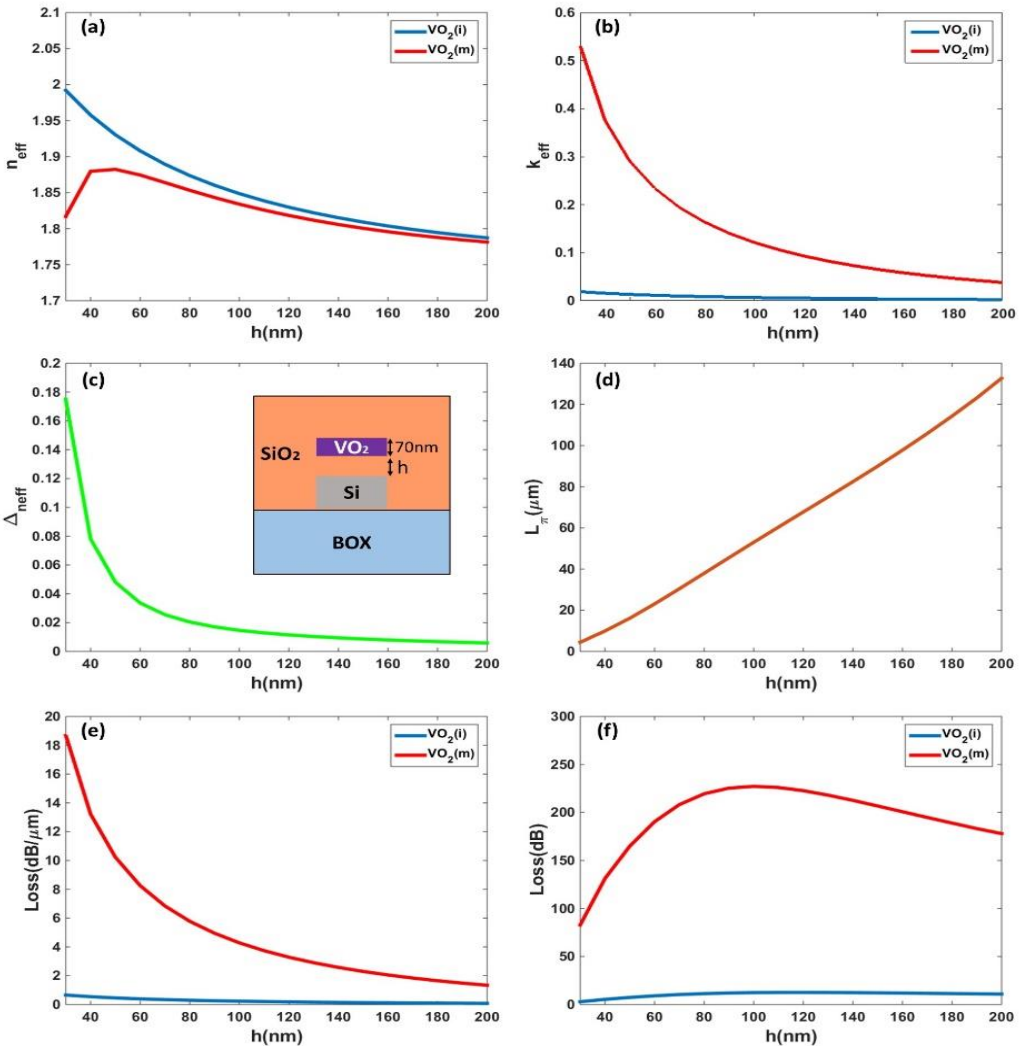

Figure 63: For TM polarization, (a,b) real and imaginary part of the effective refractive index for both states. (c) Δneff and (d) Lπ length for a wavelength of 1550nm as a function of the spacer thickness for the waveguide structure shown in the inset. (e) Propagation losses and (f) total losses for the Lπ length considering both VO_2 states.

The influence of the VO_2 film thickness has also been analyzed and results are shown in Figure 64. In this case, the spacer thickness has been set to h=30nm. Increasing the thickness, the index variation between both states increases and therefore the L_π length is decreased. For a thickness of 70nm, L_π is reduced until an ultra-compact length of only 4.5μm. For such value, the total losses in the

insulating state are only 2.9dB while the losses in the metallic state would be as high as 83dB.

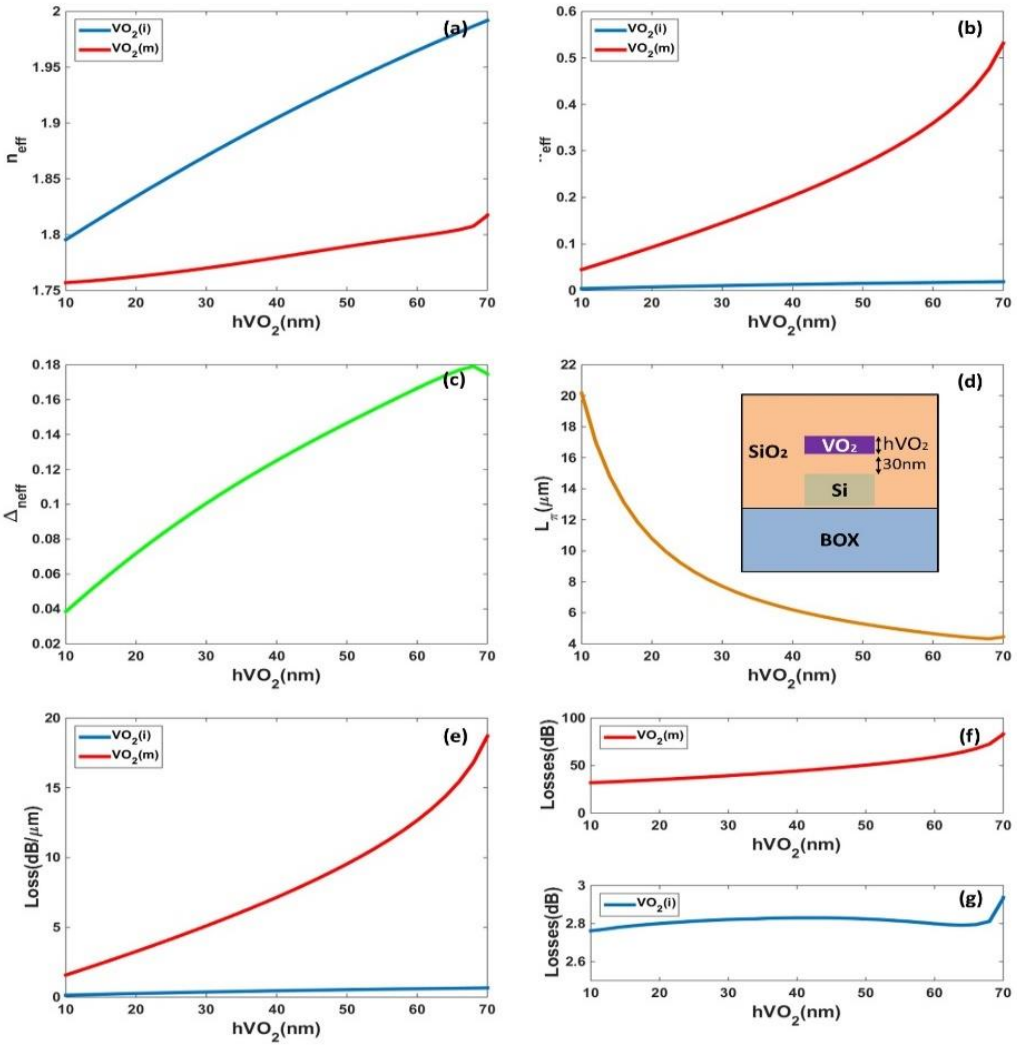

Figure 64: (a,b) Real and imaginary part of the effective refractive index for both states. (c) Δneff and (d) resultant Lπ length for a wavelength of 1550nm as a function of the VO_2 film thickness for the waveguide structure shown in the inset. (c) Propagation losses for both VO_2 states and (d) total losses for the Lπ length.

The optimum values obtained for each polarization are summarized in Table 9. The optimum values of the spacer and VO_2 film thicknesses have been chosen with the goal of minimizing the losses in the insulating state, which is the most critical parameter to achieve a good performance of the switch.

Table 9: Summary of optimum values for TE and TM polarization.

Pol.	hVO_2(nm)	h(nm)	Lπ(μm)	Losses in insulating state(dB)	Losses in metallic state(dB)
TE	10	0	16	2.3	22
TM	70	30	4.5	2.9	83

It can be seen that shortest active length has been obtained for TM polarization. However, a taper structure would be necessary to excite the desired mode and also the coupling losses would be higher. Furthermore, bend losses in conventional silicon waveguides are also higher for TM polarization so that larger ring radius would be required with respect to TE polarization. As instance, for a radius of 3.5μm, it should be noticed that bend losses cannot be neglected in the silicon waveguide for TM polarization as it was depicted in Figure 60. On the other hand, we have also analyzed the impact of having a VO_2 film with a width higher than the waveguide. This can be necessary depending on the electrodes configuration. Figure 65 shows the TE mode profiles for both VO_2 states for the waveguide optimized for TE polarization when the width is the same than the silicon waveguide or much higher and Figure 66 show the results for the waveguide optimized for TM. In any case, it can be seen that the effective index and loss are almost unchanged.

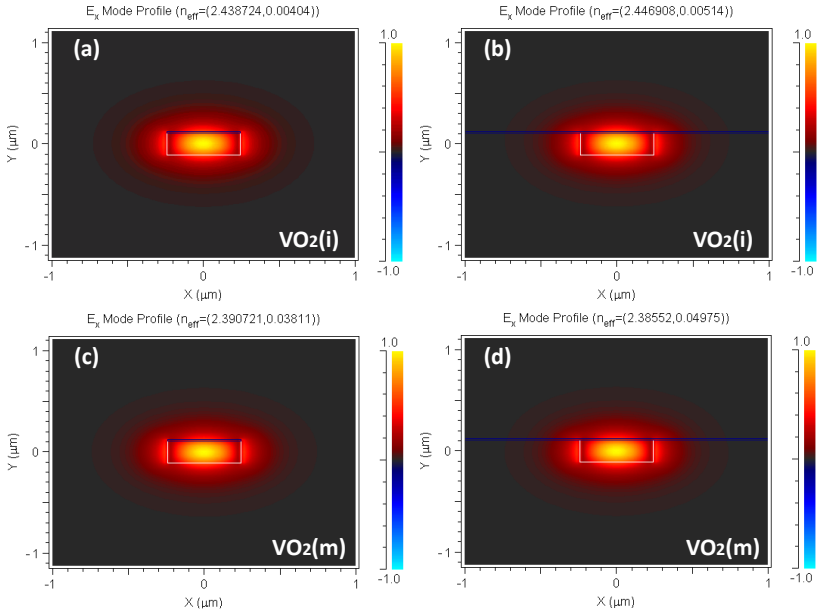

Figure 65: TE mode profile for (a,c) VO_2 film with the same width than the silicon waveguide and (b,d) VO_2 film with a width much higher than the waveguide width. The optimized values are h=0nm and hVO_2=10nm.

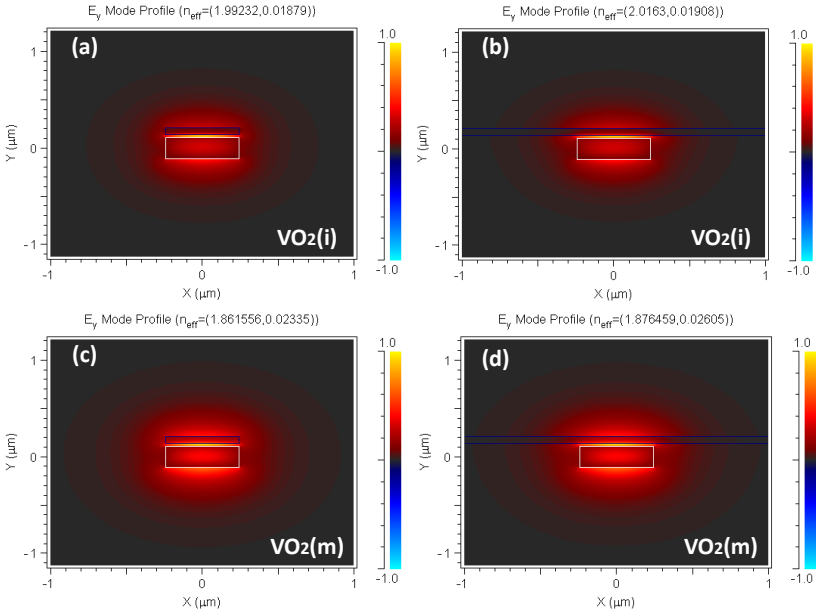

Figure 66: TM mode profile for (a,c) VO_2 film with the same width than the silicon waveguide and (b,d) VO_2 film with a width much higher than the waveguide width. The optimized values are h=30nm and hVO_2=70nm.

For the design of the real waveguide for the 2x2 microring switch, we have started from the previous designs for each polarization but we have introduced several limitations considering the characteristics of the fabrication process:

- A standard silicon waveguide with a cross section of 480 x 220nm is considered. The waveguide is covered by a silica cladding which is etched down and planarized close to the waveguide. The VO_2 film is then deposited and metal contacts are placed on both sides of the waveguide.
- The VO_2 film is wide enough to avoid the introduction of optical losses in the field of the waveguide due to the proximity of the electrodes.
- The electrodes are deposited directly over the VO_2 film. It implies that the upper-cladding of the device is air instead of silica.
- The length of the VO_2 patch is optimized to only obtain propagation losses of 0.5dB in the cross state (insulating state).

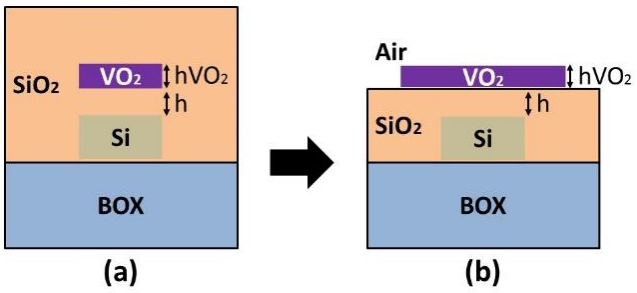

Figure 67: (a) Ideal VO_2/Si waveguide. (b) Redesign to take into account the real structure.

The silica spacer and the VO_2 film thickness have been redesigned to achieve the best performance in terms of insertion losses and crosstalk of the 2x2 switch.

3.2.3. Design optimization for TE polarization.

Figure 68 shows the (a,c) real and (b,d) imaginary part of the effective refractive index for both VO_2 states. As it was expected, comparing with the insulating state, there is a change in the real part of the effective refractive index and the mode increases its losses for the metallic state, giving a huge change in the absorption.

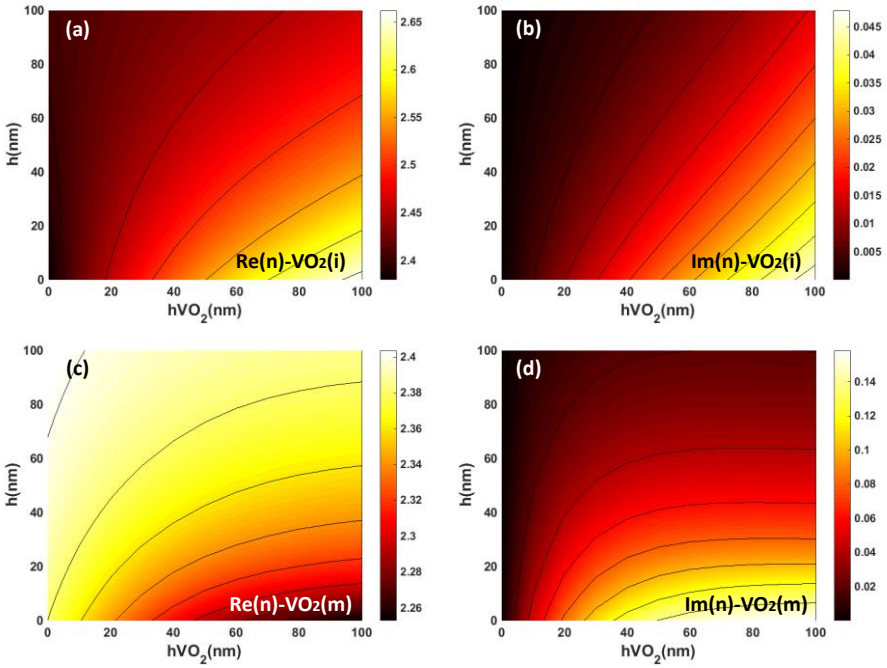

Figure 68: For TE polarization and both VO_2 states, the (a,c) real and (b,d) imaginary part of the effective refractive index are represented as function of the silica spacer and the VO_2 thickness.

From the contours depicted in Figure 68 (b) and (d), Figure 69 shows the propagation losses for the insulating and the metallic states in dB/μm:

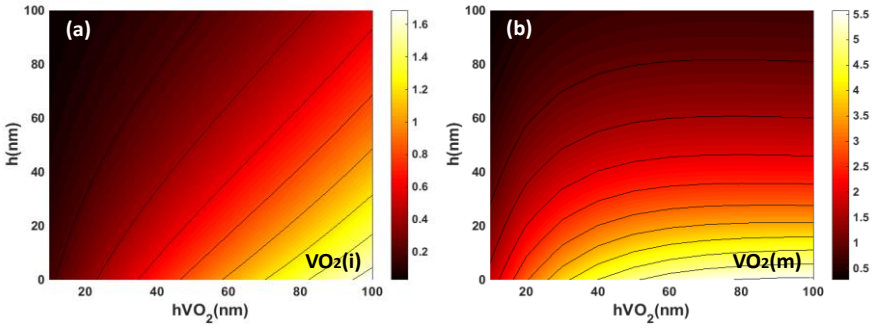

Figure 69: Losses in dB/um for the (a) insulating and (b) metallic states.

The variation in the real part of the effective refractive index is obtained by subtracting the contours depicted in Figure 68(a) and (c). It determines the L_π length, and therefore the phase shift introduced with the SMT. However, we have imposed that the losses introduced in the VO_2 in the insulating state should be lower than 0.5dB. Therefore, the VO_2 length (L_{VO2}) will be shorter than L_π and the phase shift will be lower than pi radians. Figure 70 shows the (a)Δ_{neff}, (b) L_π, (c) L_{VO2} and (d) phase shift.

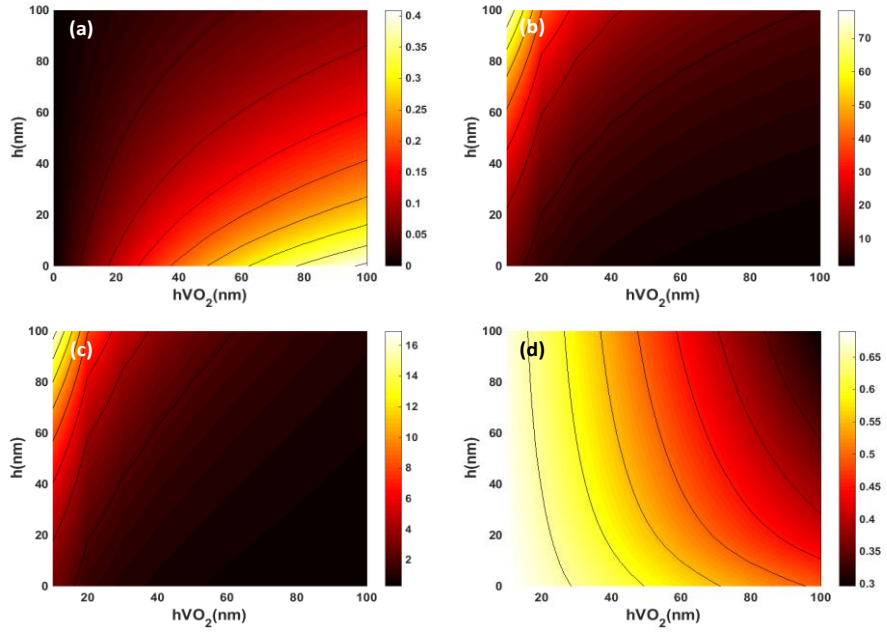

Figure 70: The (a) variation in the effective refractive index, (b) length to achieve a phase shift of pi radians, (c) active length to ensure losses of 0.5B in the insulating state and (d) phase shift for the active length are depicted for TE polarization.

Finally, the insertion losses of the switch have been calculated as the losses in the cross state (vanadium dioxide in its insulating state) with losses $a_i = 0.5dB$ and $\phi_i = 0$. On the other hand the crosstalk levels for the cross and the bar states have been calculated considering the insulating ($a_i = 0.5dB, \phi_i = 0$) and metal states (a_m, ϕ_m) respectively.

$$IL_{cross}\ (a_i = 0.5dB, \phi_i = 0) = \frac{a_i(1-t^2)^2}{1-2t^2a_i cos\phi_i + (t^2a_i)^2}$$

$$CT_{cross}(a_i = 0.5dB, \phi_i = 0) = \frac{t^2a_i^2 - 2t^2a_i cos\phi_i + t^2}{1-2t^2a_i cos\phi_i + (t^2a_i)^2}$$

$$IL_{bar}(a_m, \phi_m) = \frac{t^2a_m^2 - 2t^2a_m cos\phi_m + t^2}{1-2t^2a_m cos\phi_m + (t^2a_m)^2}$$

$$CT_{bar}(a_m, \phi_m) = \frac{a_m(1-t^2)^2}{1-2t^2a_m cos\phi_m + (t^2a_m)^2}$$

The losses in the metallic state have been obtained adding the variation in the absorption to the losses in the insulating state. The phase, is defined as the shift introduced by the length of the VO_2 patch considering that the shift would be π radians for the calculated L_π length:

$$\Delta\alpha = [Losses\ VO_2(m) - Losses\ VO_2(i)] \cdot L_{VO2}$$

$$a_m(dB) = a_i(dB) + \Delta\alpha$$

$$\emptyset_m = \frac{L_{VO2}}{L_\pi} \cdot \pi$$

The insertion loss, optimum t and crosstalk at the bar and cross states as a function of h and h_{VO2} are shown in Figure 71 for TE polarization.

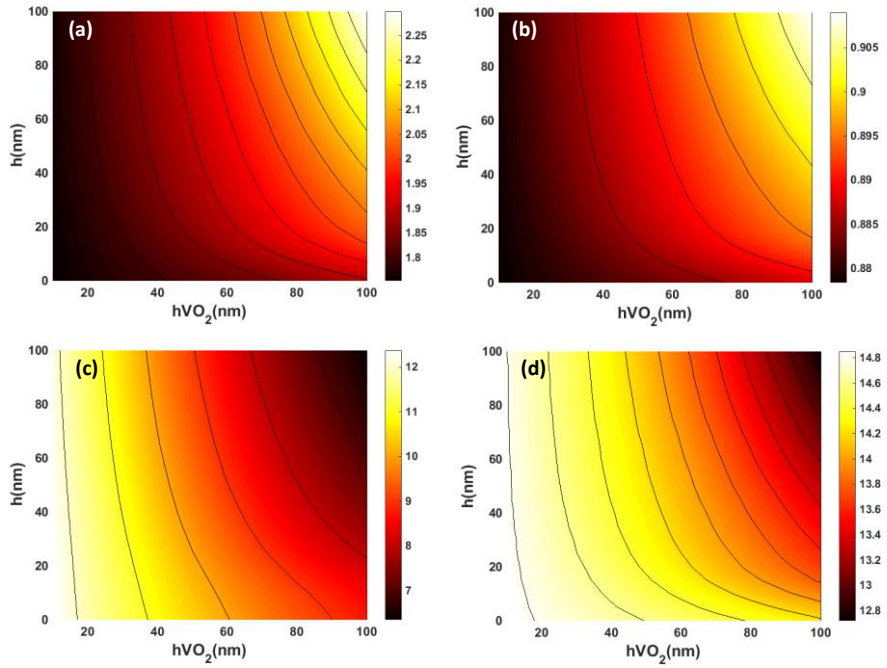

Figure 71: (a) Insertion losses, (b) optimum transmission coefficient and crosstalk levels at the (c) bar and the (d) cross states are shown for TE polarization.

Insertion losses and crosstalk are maximized as the VO_2 layer is thinner while the influence of varying the spacer thickness is low. However, the active length is minimized for thinner spacers as is shown in Figure 70(b). Therefore, lower spacers and VO_2 thicknesses are desirable to achieve the optimum switching performance. For a 10nm-thick VO_2 film deposited on top of the silicon waveguide (h=0nm), an active length of 2.8μm will be required to ensure insertion losses of 1.75dB and a crosstalk higher than 12dB at both switching states. Figure 71(b) shows the required transmission coefficient in the microring resonator to obtain the calculated insertion losses and crosstalk values. According to the designed

values of h and hVO_2, the optimum transmission coefficient is t=0.88 for TE polarization. 3D-FDTD simulations have been carried out to determine the required gap between the ring and the input/output waveguides to obtain the required transmission coefficient. A radius of 3.5µm has been first chosen for a compact footprint below 100µm². Figure 72(a) shows that a gap of 30nm provides the transmission coefficient of 0.88.

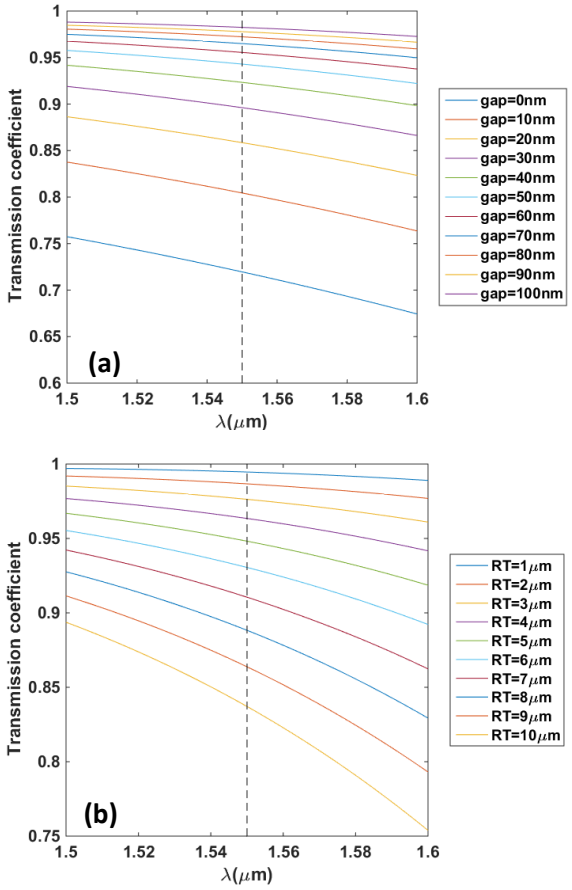

Figure 72: (a) Transmission coefficient as function of the wavelength and the gap distance between the input/output waveguides and the ring. (b) Transmission coefficient as function of the wavelength and the racetrack length for a gap distance between the input/output waveguides and the ring of 200nm.

Nevertheless, a gap of 30nm between the input/output waveguides and the ring can be challenging during the fabrication process. Considering this, a possibility consists in using a racetrack configuration to fulfill fabrication constraints. Increasing the coupling length allows to increase the distance between the ring and the waveguides making possible a more feasible fabrication process. Figure 72(b) shows that for a gap distance of 200nm between the input/output waveguides and the ring, the optimum transmission coefficient is obtained with a

racetrack length of 8µm. The main values obtained for the TE polarization design are summarized in Table 10.

Table 10: Summary of the results obtained for TE polarization.

Pol.	h (nm)	hVO_2 (nm)	Lπ (µm)	LVO_2 (µm)	ΔØ (rad)	Δα (dB)
TE	0	10	13	2.88	0.69	4.36

IL (dB)	CT_{BAR} (dB)	CT_{CROSS} (dB)	t
1.75	12.3	14.8	0.88

Figure 73 shows the different TE mode profiles for the silicon waveguide and for the Si-VO_2 waveguide structure with the optimum parameters previously designed. The mode does not experiment a huge change in its mode profile when the VO_2 changes from the insulating state to the metallic state. Nevertheless, an order of magnitude change in the imaginary part of the effective refractive index is obtained. In both VO_2 states, the mode profile is also very similar to the one of the silicon waveguide. It ensures a soft transition from the TE mode of the input silicon waveguide to the mode of the hybrid section, reducing the losses by reflection and mode mismatch.

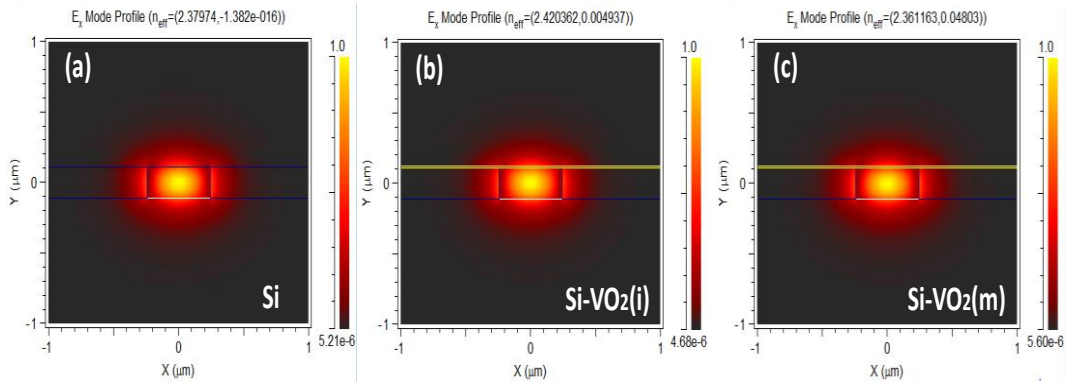

Figure 73: TE polarization mode profile for the (a) silicon waveguide and for the Si-VO_2 waveguide in the (b) insulating and (c) the metallic state.

In order to analyze the transmission performance and to confirm the low coupling losses due to the modal mismatch between the silicon and hybrid VO_2/Si waveguides, the optimum hybrid VO_2/Si waveguide have been simulated by 3D-FDTD. Figure 74 shows the electric field contour maps for both VO_2 states. Coupling losses are negligible and the transmission performance is in excellent agreement with simulation results obtained from the modal analysis. Thereby,

losses in the insulating state, shown in Figure 74 (a), are 0.5 dB while they increase to around 5 dB when the VO_2 changes to the metallic state, shown in Figure 74(b). It should be reminded that the VO_2/Si waveguide length has been designed to have only 0.5dB losses at the insulating state.

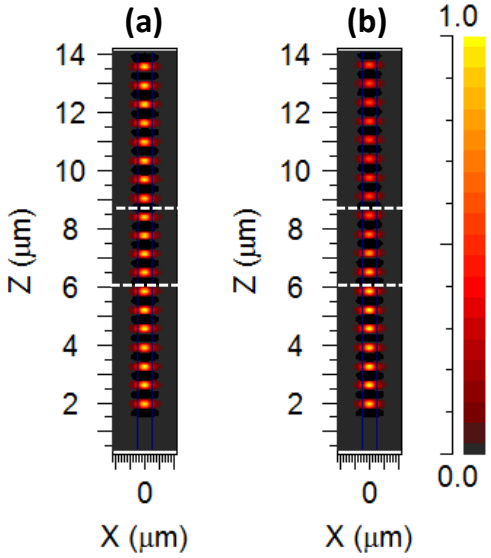

Figure 74: 3-D FDTD simulations of the designed hybrid VO_2/Si waveguide, which is depicted with a white dashed rectangle, in the (a) insulating and (b) metallic states for TE polarization. The hybrid waveguide length is 2.8μm.

3D-FDTD simulations of the final hybrid VO_2/Si microring switching structure have also been performed to validate the whole design. Figure 75(a) shows the response at the cross state. In this case, the VO_2 is in the insulating state and the switch operates at the ring resonance. The optical bandwidth is around 3.8nm that will allow a data throughput rate higher than 500Gbps. Furthermore, the throughput can be increased beyond Tbps operation by using a WDM optical signal with a wavelength spacing matched with the free spectral range of the ring resonances to simultaneously switch on and off a large number of wavelength channels. Figure 75(b) shows the response at the bar state in which the VO_2 is switched to the metallic state. It can be seen that the higher ring losses have a large influence on the ring resonance, which is almost suppressed. Furthermore, the resonance wavelengths are also shifted due to the additional phase shift induced by the variation in the VO_2 state. Both effects contribute to improve insertion losses and reduce the crosstalk.

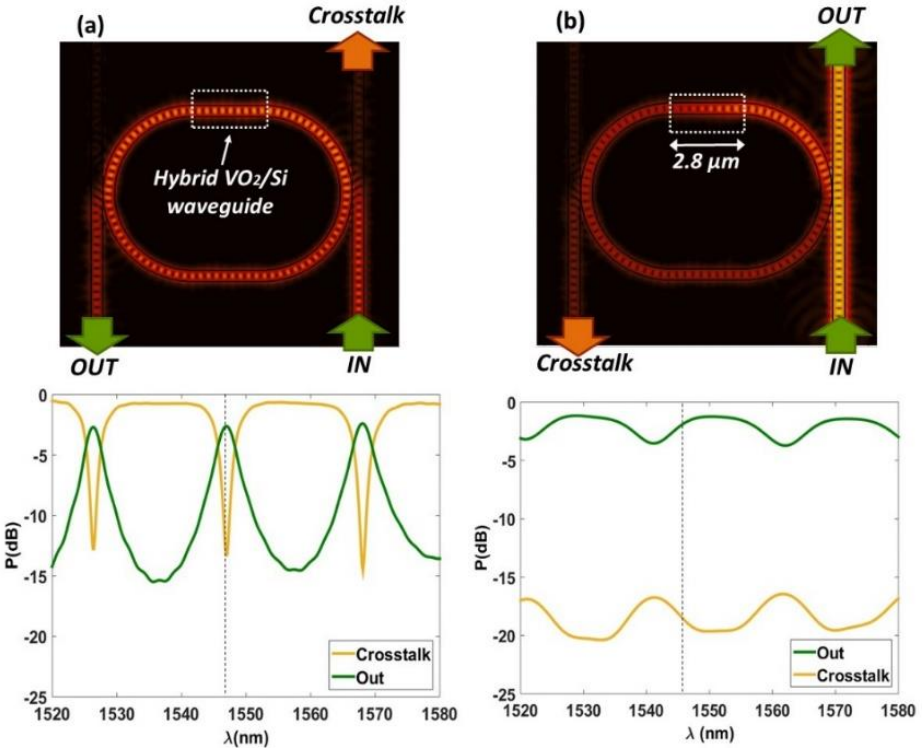

Figure 75: 3-D FDTD simulations of the hybrid VO_2/Si microring switch for the (a) cross and (b) bar states and TE input polarization. The dashed vertical line shows the operating optical wavelength.

3.2.4. Design optimization for TM polarization.

We have extracted the same results than in the previous section but this time considering the TM modes of the waveguide. Figure 76 shows the effective refractive index for both VO_2 states as function of h and hVO_2.

Especially interesting is the evolution of the effective refractive index for the metallic state (c,d). There are abrupt changes in the real and the imaginary part of the effective refractive index. This is due because depending on the combination of h and hVO_2, the TM mode has a very different mode profile and therefore, its effective refractive index shows important variations. For example, Figure 77 shows, for a silica spacer of 20, 80 and 200nm, the mode profiles for a VO_2 thickness of 20, 45 and 70nm. For a silica spacer of (g,h,i) 200nm, the TM mode profile is very similar to the TM mode of a silicon waveguide surrounded by silica. If the silica spacer is reduced to 80nm and the VO_2 film is thicker than 40nm (e,f) the field is concentrated in the silica between the silicon waveguide and the VO_2 film. The same behavior is depicted for a silica spacer of 20nm with a field even more concentrated in the slot. This higher concentration provokes a higher level of losses on the mode.

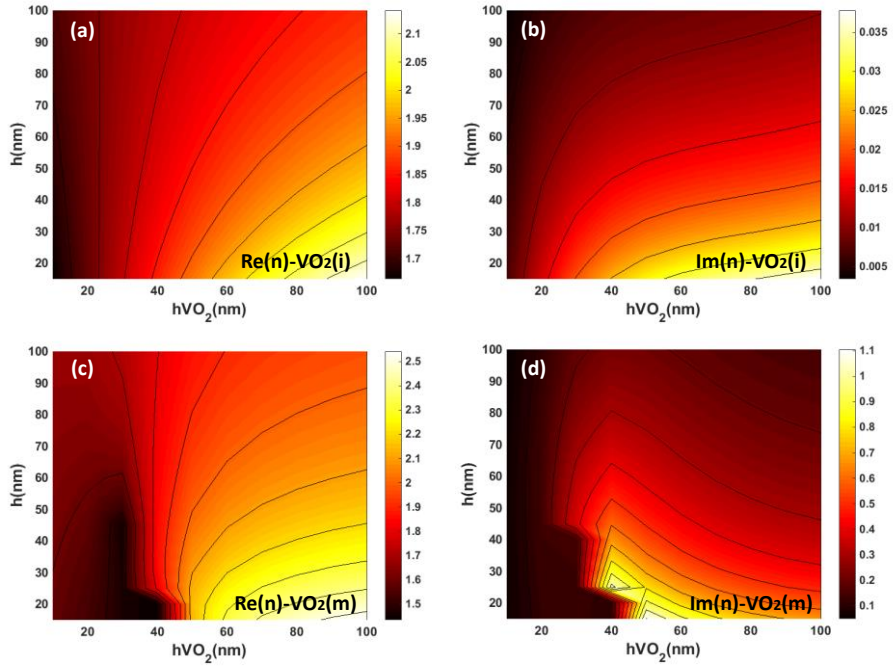

Figure 76: For TM polarization and both VO_2 states, the (a,c) real and (b,d) imaginary part of the effective refractive index are represented as function of the silica spacer and the VO_2 thickness.

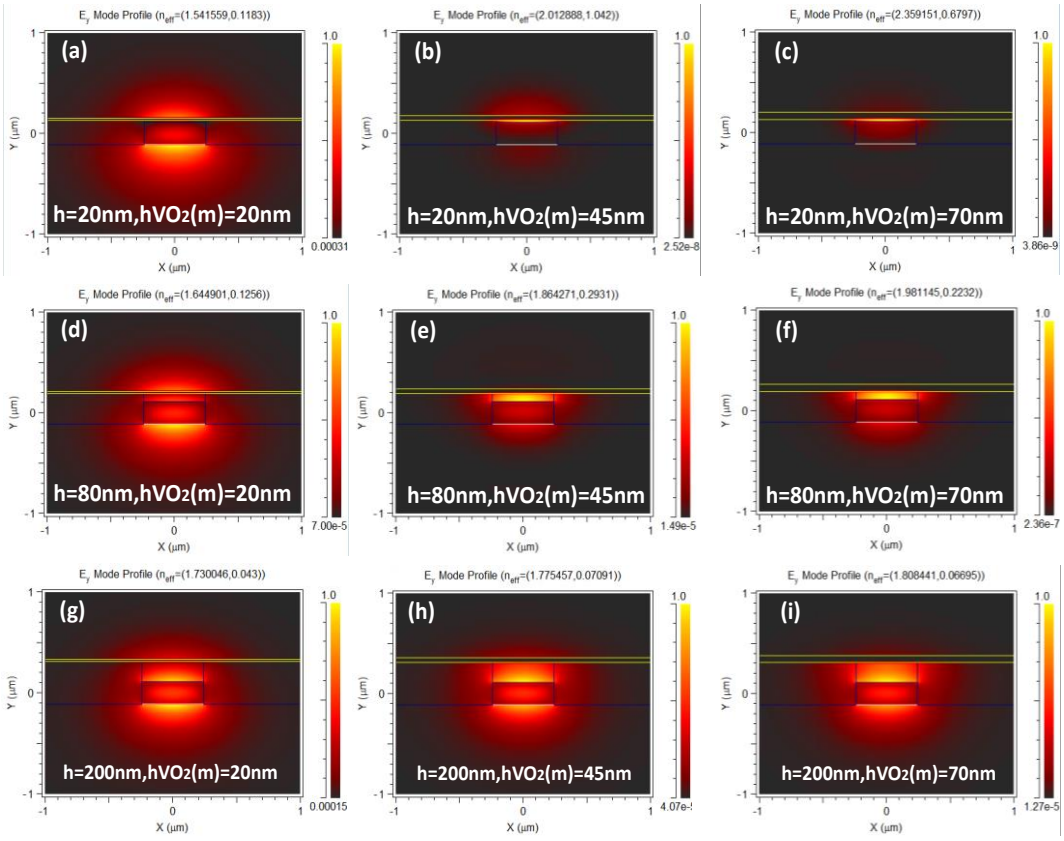

Figure 77: TM mode profiles as function of silica spacer and VO_2 thickness.

Table 11 describes an approximation of the behavior of the TM mode as function of h and hVO_2 obtained from the analyses of Figure 76 and Figure 77.

Table 11: Approximation of the behavior of the TM mode.

h(nm)	hVO_2(nm)	Behaviour
[15,100]	<40	Like a TM mode of a silicon waveguide.
[15,100]	>40	The field is concentrated in the slot
>100	---	Like a TM mode of a silicon waveguide.

Figure 78 shows the propagation losses for the insulating and the metallic states in dB/µm and Figure 79 shows the (a)Δ_{neff}, (b) L_π, (c) L_{VO2} and (d) phase shift. The insertion losses, crosstalk levels and optimum transmission parameter for TM polarization are shown in Figure 80. In this case, it can be seen that there is a region where low insertion losses are achieved. For different combinations of h and hVO_2, insertion losses below 1.3 dB are possible but the crosstalk at bar state is penalized. Therefore, there is a trade-off between the insertion losses and crosstalk levels at both states. For a VO_2 film with a thickness of 40nm and a spacer of 25nm and an optimum transmission coefficient of t=0.85, crosstalk levels higher than 16dB and insertion losses of 1.5dB are achieved by using an ultra-short active length of only 0.67µm.

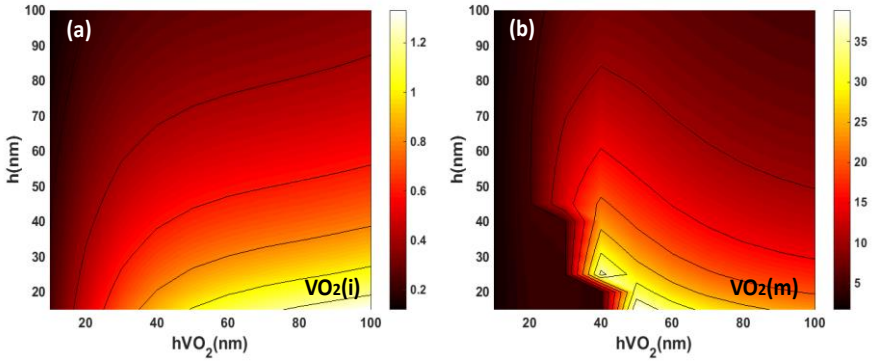

Figure 78: Losses in dB/um for the (a) insulating and (b) metallic states.

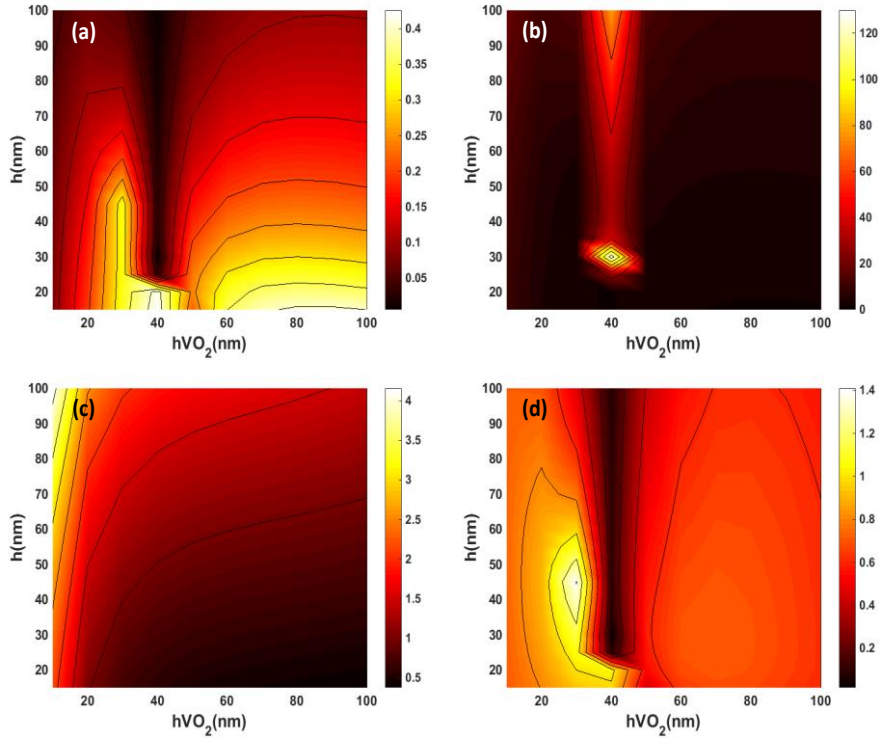

Figure 79: The (a) variation in the effective refractive index, (b) length to achieve a phase shift of pi radians, (c) active length to ensure losses of 0.5B in the insulating state and (d) phase shift for the active length are depicted for TM polarization.

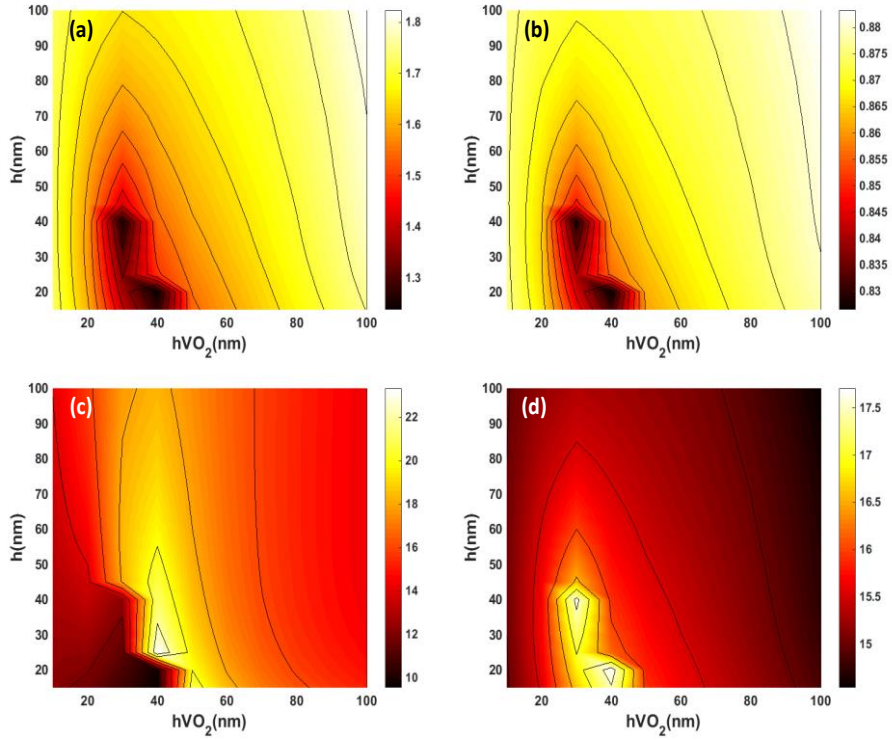

Figure 80: (a) Insertion losses, (b) optimum transmission coefficient and crosstalk levels at the (c) bar and (d) cross states are shown for TM polarization.

To achieve the optimum t of 0.85 using the racetrack configuration with a gap between the input/output waveguides and the ring of 200nm, Figure 72(b), the racetrack would be larger than for the TE polarization. In this case, a length ranging 9 to 10µm would be necessary. Table 12 summarizes the main values obtained in the design for TM polarization.

Table 12: Summary of the results obtained for TM polarization.

Pol.	h (nm)	hVO_2 (nm)	Lπ (µm)	LVO_2 (µm)	ΔØ (rad)	Δα (dB)
TM	25	40	26	0.67	0.081	24

IL (dB)	CT_{BAR} (dB)	CT_{CROSS} (dB)	t
1.5	23.3	16.1	0.85

The TM mode profiles of the silicon waveguide and for the optimized waveguide structure, considering both VO_2 states, are depicted in Figure 81. Comparing with the TM mode of the silicon waveguide, the vanadium dioxide provokes the confinement of the mode through the silica spacer between the silicon waveguide and the VO_2 film. For the metallic state, the waveguide becomes multimode and two possible modes appear. Figure 81(c) shows the highly confined mode considered to obtain the results shown in Figure 80. It can be seen that the mode profile is similar with respect to the insulating state but there is a large variation in the imaginary part of the effective index that gives rise to a high loss difference of 25dB. However, a very small loss difference of only 1.8 dB is achieved with the second mode shown in Figure 81(d) basically because the mode profile is more similar to the mode of the silicon waveguide, Figure 81(a), and there is less optical confinement in the VO_2 layer. In contrast with the case of TE polarization, for both VO_2 states, it is expected that the change in the modal shape will introduce losses due to the mode mismatch.

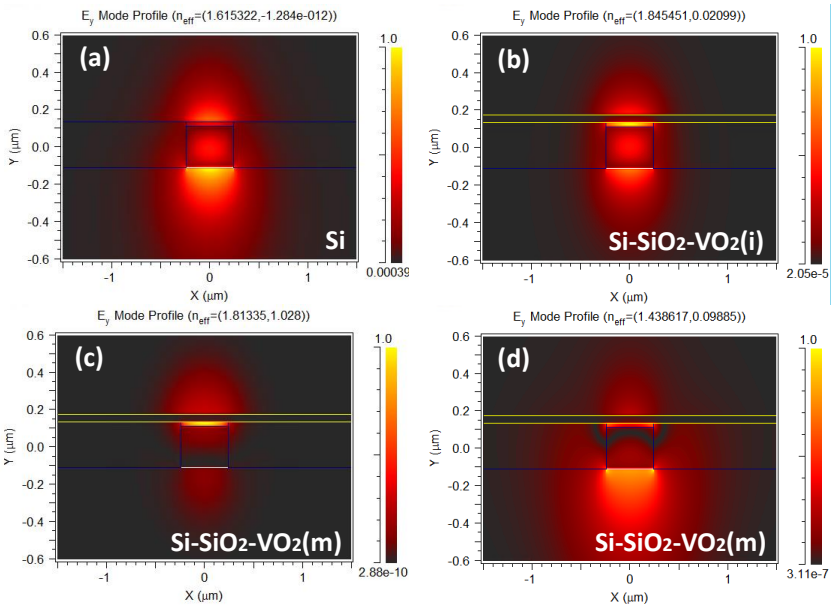

Figure 81: TM mode profile for (a) the silicon waveguide and for the Si-VO_2 waveguide structure in the (b) insulating and (c,d) metallic states. For the metallic state two modes are considered.

Once again, the structure have been simulated by 3D-FDTD to analyze the transmission performance and coupling losses due to the modal mismatch between the silicon and hybrid VO_2/Si waveguides. Figure 82 shows the electric field contour maps for TM polarization and both VO_2 states. Although the VO_2 length has been calculated to obtain losses of 0.5dB in the insulating state, the total losses in this state, Figure 82(a), are increased to 2.1dB due to the inefficient coupling. In this case, coupling losses cannot be neglected because there is a higher mode mismatch between the TM mode in the silicon waveguide and the TM mode in the hybrid VO_2/Si waveguide, as it was expected according to the results shown in Figure 81. Furthermore, losses of only 5.2dB have been obtained when the VO_2 changes to the metallic state, which is shown in Figure 82(b). These losses are much smaller than the expected ones of around 25dB due to the multimode performance of the hybrid VO_2/Si waveguide. More concretely, the undesired second TM mode, Figure 81(d), is also partially excited thus contributing to reduce the total losses of the structure that will therefore have a negative impact on the switching performance. To only excite the slot mode depicted in Figure 81(c) it would be necessary some kind of additional structure like a taper in order to achieve the transition from the input mode to the slot mode of the hybrid section. Nevertheless, this structure would introduce several fabrication steps and it would increase the losses in the insulating state. Therefore, the optimum polarization for the switch device is TE polarization.

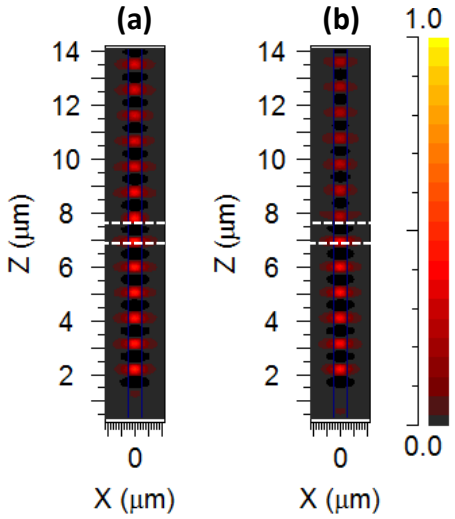

Figure 82: 3-D FDTD simulations of the designed hybrid VO_2/Si waveguide, which is depicted with a white dashed rectangle, in the (a) insulating and (b) metallic states for TM polarization. The hybrid waveguide length is 0.67μm.

3.2.5. VO_2 optical characterization by ellipsometry.

The refractive index of VO_2 planar films on Si wafers have been measured by ellipsometry. Figure 83 shows the (a) real and (b) imaginary (extinction coefficient, k) part of the refractive index as function of the wavelength for VO_2 planar films with thicknesses of 40nm, 75nm and 90nm.

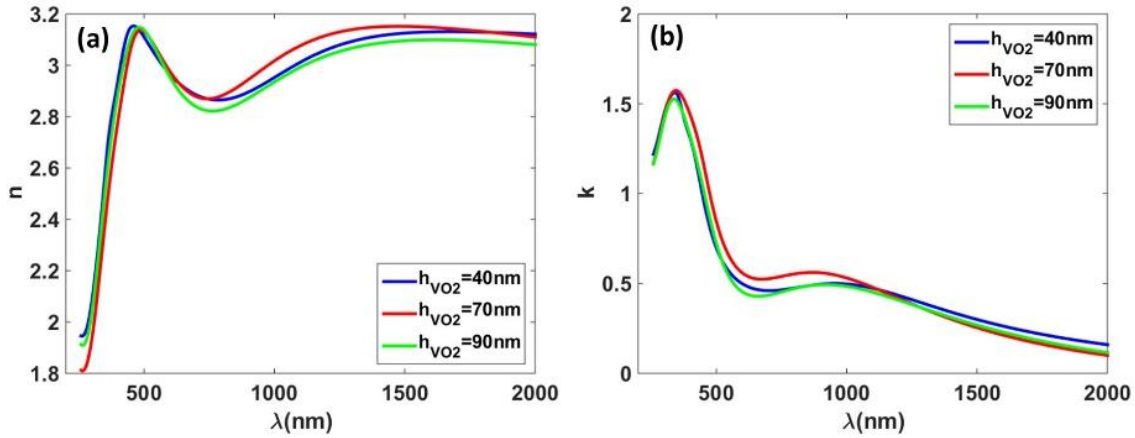

Figure 83: (a) Real and (b) imaginary part of the refractive index as function of the wavelength measured by ellipsometry in VO_2 planar films with thicknesses of 40nm, 75nm and 90nm.

Table 13 summarizes, for a wavelength of 1550nm, the refractive index measurements of the different planar films as function of the VO_2 thickness. According to the extracted data, the refractive index is quite stable for this range

of thicknesses. The real part is around 3.1 while the imaginary part ranges between 0.23 and 0.28. In the simulations, we have considered a lower value for the imaginary part according to the bibliography [49]. It implies that a fabricated device with vanadium dioxide should show higher losses than the calculated in the simulations during the insulating state. Small losses in this state are crucial to achieve high performance. Nowadays, several approaches like doping the vanadium dioxide are under study looking for the reduction of the imaginary part of the effective refractive index of the material at steady conditions.

Table 13: For a wavelength of 1550nm, refractive index of the planar films as function of the VO_2 thickness.

VO_2 thickness (nm)	**n(λ=1550nm)**	**k(λ=1550nm)**
39.565 ± 0.299	3,128	0,281
74,921±0.622	3,15	0,232
86.017 ± 0.973	3,098	0,248

To characterize the influence of the temperature, the refractive index has been measured at three different temperatures in collaboration with Horiba. In this case, the thickness of the VO_2 film was 90nm. The chosen temperatures were 30, 70 and 110°C that correspond to temperatures in the insulating state, across the SMT and the metallic state respectively. The values of the real and imaginary part, at 1550nm, as function of the temperature are summarized in Table 14.

Table 14: Real (n) and imaginary (k) part of the refractive index of a VO_2 film as a function of temperature.

Temperature (°C)	**n (λ=1550 nm)**	**k (λ=1550 nm)**
30	3.1	0.25
70	3.1	0.3
110	1.6	2.9

The values obtained at 30°C and 70°C are consistent with the refractive index of the insulating state obtained by bibliography at room temperature [49]. At 110°C a clear change in both components of the refractive index is observed consistent with a metallic behavior although the real part of the index is lower than the expected.

3.2.6. Electrical characterization over VO_2 films.

The efficiency of the phase transition in the VO_2 can only be analyzed experimentally due to the lack of accurate theoretical models implemented in commercial solvers.

In the control of the vanadium dioxide switching, one of the remaining challenges, is to trigger the phase transition in the VO_2 integrated with silicon photonic waveguides by an external electric field instead of thermally, which has already been demonstrated for high speed electronics [74] and it is starting to be investigated for photonics [62], to benefit from the ultrafast response inherent to the SMT effect.

Therefore, this point has been the subject of an intense research. Initial works argued that the insulator to metal transition was mainly induced electrically because the leakage current through the device was not enough high to reach the critical temperature of the VO_2 [75,76]. In the last years, several works have explained the VO_2 transition as a combination of an electric process with a thermal effect. Electrical triggering has been justified due to the fast switching time. Nevertheless, a pure electric field switching without any thermal contribution has not been completely demonstrated although it has been tried, for example, introducing dielectrics to [77-79] eliminate the leakage current. The metal insulator transition triggering has also been described by means of the carrier injection due to the Poole-Frenkel effect [74,78]. This effect provides an exponential growth in the I-V characteristics of a two terminal device prior to an abrupt current change which indicates the formation of a thermal filament or metallic current path.

This means that the current flowing through the VO_2 layer most probably does not only modify the carrier density locally but also increases the temperature of the layer, bringing the system closer to the thermal SMT transition. Since heat dissipation is slow, this may hamper a fast return to the insulating state upon cooling.

Therefore, controlling the SMT by heating or with an electric field are the most common approaches for developing electro-optical devices based on the VO_2/Si hybrid technology. The optimum design of the electrodes to reduce the power consumption and switching time is still a challenging area. Recently, the phase transition using electrodes with a VO_2 patch between them have been studied [77,78,81]. Thermal effects have an important role in the phase transition and they are related to the geometry and material used for the electrodes and the load

resistance [77]. Joushaghani et al. observed, by controlling the current applied to a VO_2 microwire, that the phase transition is produced in two different steps [80]. As it was mentioned previously, the first step is an electronic process which gives rise to a change in resistivity, and therefore optical absorption, without hysteresis. On the other hand, the second step of the phase transition is a process based on thermal filament formation which is mainly due to a thermal contribution by Joule heating.

The electrical switching performance of VO_2 junctions has been simulated and experimentally analyzed using the structure shown in Figure 84. The thickness of the VO_2 has been fixed to 40nm. Copper electrodes have been used with a thickness of 100nm.

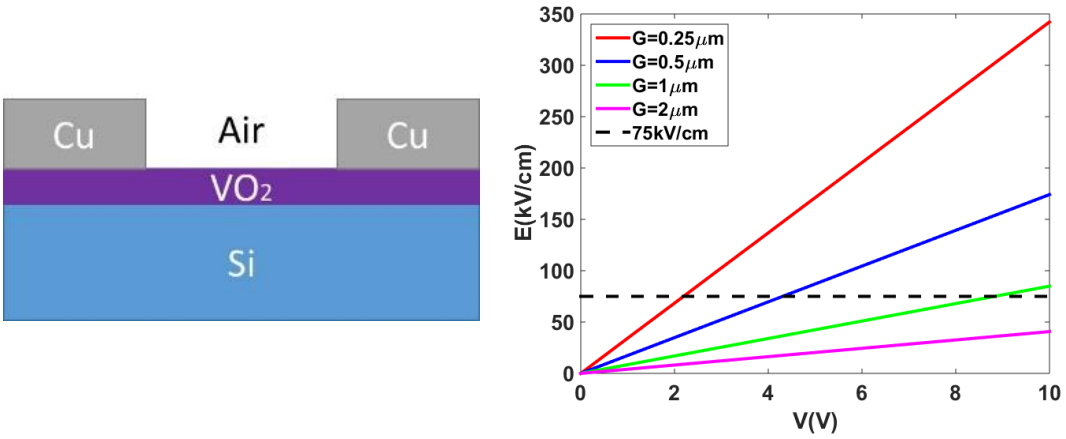

Figure 84: Cross section of the fabricated structure and electric field as function of the applied voltage for different gaps between the electrodes.

The electric field distribution along the structure has been firstly simulated with COMSOL by applying voltage sweeps for different gaps between the electrodes. According to previous works [77], the required electric field to induce the insulator to metal transition is around 75kV/cm. This electric field is achieved for a voltage of 4.4V, 8.8V and 17.6V for an electrode gap of 500nm, 1µm and 2µm respectively, as it is shown in Figure 84.

To compare simulations with experimental results, electrodes with different gaps and widths have been fabricated to analyze the influence of these parameters in the required electrical power to induce the VO_2 change. Figure 85 shows (a) a schematic of the electrode layout specifying the considered gap and width ranges, (b) the gds file containing all the electrodes and (c) a SEM images of the fabricated structures.

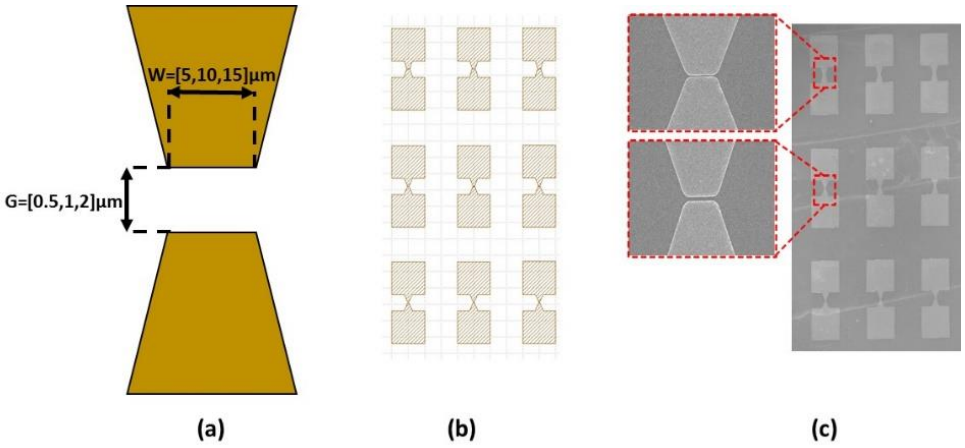

Figure 85: a) Schematic of the electrodes, (b) designed gds and (c) SEM images of the fabricated structures.

The separation between the electrodes and their width have been varied ranging from 500nm to 2µm and from 5µm to 15µm respectively. The devices have been measured by applying voltage sweeps with the current limited, using a load resistance of 1kΩ, to avoid their deterioration. To realize the measurements, two DC probes are deposited directly over the metallic pads and a Keithley 2440 Source-meter is used to simultaneously generate the voltage sweeps and measure the current through the device.

Figure 86 shows the V-I response of the electrodes with a width of 5µm and gaps of 500nm, 1µm and 2µm. In all cases, an abrupt increase in the current is obtained demonstrating the transition from the insulator to the metallic state.

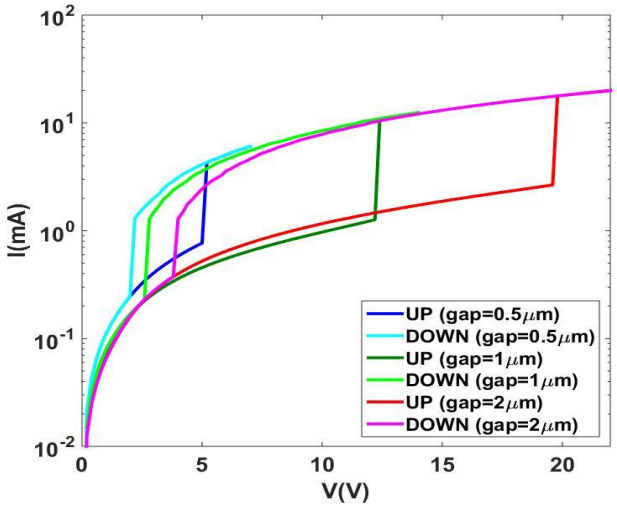

Figure 86: V-I response of the electrodes with a width of 5µm and gaps of 500nm, 1µm and 2µm.

With a low applied voltage, the electric field across the junctions leads to a small leaking current through the VO_2 due to the finite resistance in the insulating

state. When the applied voltage is high enough to induce the SMT ($V > V_{SMT}$), the resistance of the VO_2 drops and the current is abruptly increased. After the SMT, decreasing the applied voltage, the curve traces a different tendency due to the hysteretic behaviour of the VO_2 at the phase transition. When the reverse phase transition is accomplished ($V < V_{MST}$), the VO_2 returns to the original resistance state. The hysteresis width and the reverse phase transition are highly dependent on the contact metal and the thermal dissipation rates [81].

Figure 87 shows the raising sweeps for the structures outlined above. In the same graph is included the V-I response of the load resistance (1kΩ). Comparing the required voltage to induce the insulator to metal transition in each device it is demonstrated that there is a proportional relation between the required voltage and the gap. As it was expected, a higher electrical power is required to induce the SMT when the gap separation is increased because higher voltage values are needed to achieve similar values for the electric field. For example, when the gap is increased by a factor of two, the required voltage to induce the insulator to metal transition is also increased by the same factor.

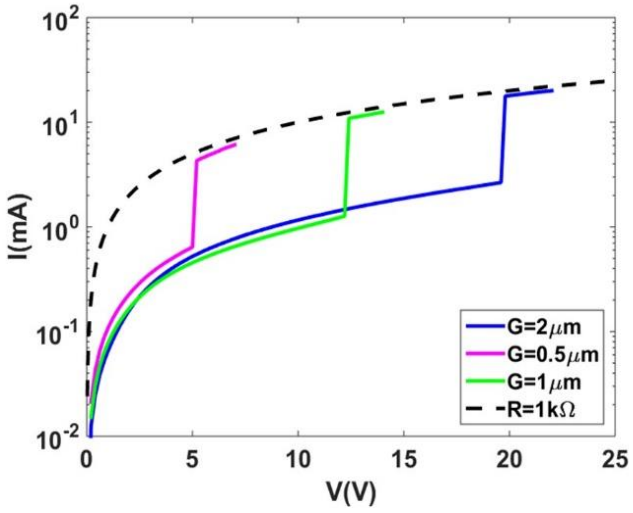

Figure 87: V-I response for the electrodes with different gaps and a width of 5μm.

Figure 88(a) shows the electric schematic of the measured structures with the load resistance. The VO_2 section between the metals can be modelled as a parallel of a resistance and a capacitance. However, as the measurements are in DC, the capacitance behaves as an open circuit. Furthermore, the resistances of the contacts and the pads are also negligible in comparison with the resistance of the VO_2 patch and the load resistance. Figure 88(b) shows the simplified schematic considering these assumptions.

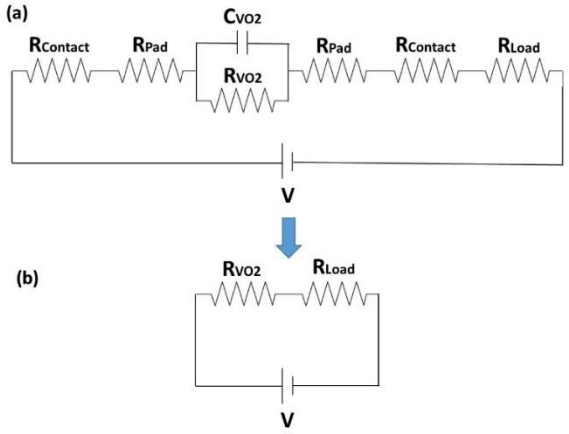

Figure 88: (a) Electrical schematic of the measured structures and (b) simplified model for DC measurements.

In the insulating state, the VO_2 is very resistive so the resistance is expected to be higher than the load resistance. By contrary, reaching the metallic state, the resistance of the VO_2 is decreased and the total resistance is governed by the load resistance. The confirmation of this behavior is demonstrated with the abrupt changes in the current through the device. In addition, it is important to notice the change in the slope before and after the transition. Before the transition, in the insulating state and including the load resistance, the average slope for the different devices is 8.25kΩ. On the other hand, after the transition, the average slope has been reduced to 1kΩ. It is necessary to remember that the load resistance is 1kΩ, so in the metallic state the resistance of the VO_2 patch is highly decreased and becomes negligible in comparison with the load resistance. Therefore, the change in the slope confirms again the change in the resistance of the VO_2 during the insulator to metal transition.

Table 15 summarizes the main results for the electrodes with different gaps and a width of 5µm. The required voltage to induce the insulator to metal transition is in very good agreement with simulation results. However, the current also increases as the gap is larger, which results in a significant increase of the required electrical power.

Table 15: Summary of insulator to metal transition results for the electrodes with a width of 5µm.

Gap (µm)	**V_{source} (V)**	**$I_{I\rightarrow M}$ (mA)**	**$V_{I\rightarrow M}$(V)**	**R_I (kΩ)**	**$P_{I\rightarrow M}$(mW)**
0.5	5	4.3	5.2	6.81	23
1	12.2	10.9	12.4	8.61	135
2	19.6	17.8	19.8	6.36	352

Figure 89 shows the V-I response for the electrodes with different gaps and a width of (a) 10µm and (b) 20µm. Once again, when the metallic state is reached, the slope of the different curves is determined by the load resistance due to the low resistance of the VO_2 in this state. Nevertheless, the slope in the insulating state is mainly determined by the gap but also on the electrode width.

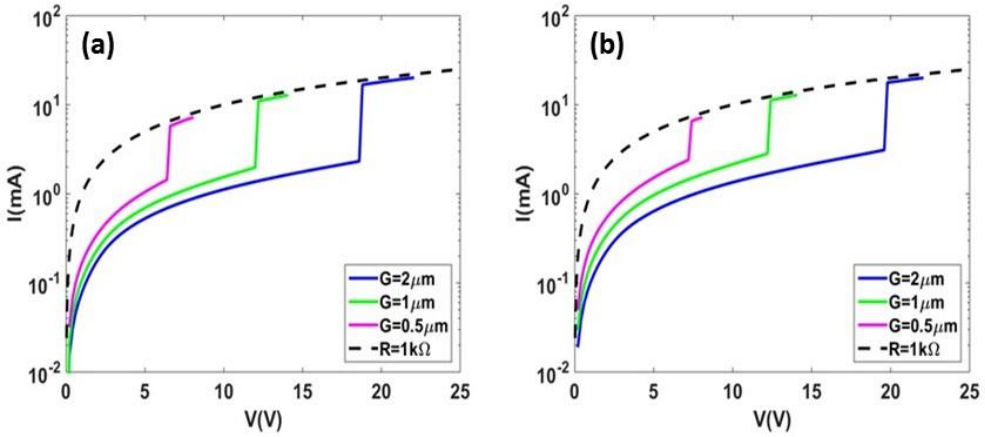

Figure 89: V-I response for the electrodes with different gaps and a width of (a) 10µm and (b) 20µm.

Table 16 and Table 17 show the insulator to metal transition results for the voltage, current, resistance and electrical power for an electrode width of 10µm and 20µm respectively. It can be observed that, for a determined width, lowering the gap decreases the resistance of the VO_2 while for a certain gap, increasing the width also contributes to reduce the resistance of the VO_2. On the other hand, analyzing the required voltage to induce the insulator to metal transition, it has been obtained that the effect of the electrode width is almost negligible.

Table 16: Summary of insulator to metal transition results for the electrodes with a width of 10µm.

Gap (µm)	**V_{source} (V)**	**$I_{I\rightarrow M}$ (mA)**	**$V_{I\rightarrow M}$(V)**	**R_I (kΩ)**	**$P_{I\rightarrow M}$(mW)**
0.5	6.4	5.8	6.6	3.44	38
1	12	11	12.2	5.06	134
2	18.6	17	18.8	7.02	320

Table 17: Summary of insulator to metal transition results for the electrodes with a width of 20µm.

Gap (µm)	**V_{source} (V)**	**$I_{I\rightarrow M}$ (mA)**	**$V_{I\rightarrow M}$(V)**	**R_I (kΩ)**	**$P_{I\rightarrow M}$(mW)**
0.5	7.2	6.5	7.4	1.99	48
1	12.2	11.2	12.4	3.33	139
2	19.6	17.7	19.8	5.3	350

Table 18 shows the required electrical power to induce the insulating to metal transition depending on the electrode gap and width. Clearly, the electrical power significantly increases when a higher gap is used. Furthermore, wider electrodes also increase the required electrical power due to the lower resistance of the VO_2 section (only a small discrepancy is observed for the case of gap of 2µm and width of 10µm).

Table 18: Required electrical power (mW) to induce the insulating to metal state depending on the electrode parameters.

Gap(µm)	**W=5µm**	**W=10µm**	**W=20µm**
0.5	23	38	48
1	135	134	139
2	352	320	350

For gap separations larger than 2µm the electrodes usually collapse at the VO_2-electrode interface. When the contact separation is increased, a higher voltage is necessary to maintain the required electric field intensity to switch the vanadium dioxide. Therefore, when the vanadium dioxide film is switched to its metallic state, an abrupt circulation of the current is obtained. If the current is not limited by an external resistance, usually the temperature increment burns the device melting the contacts or the vanadium dioxide film. This limitation is important for the integration with an optical waveguide because the proximity of the electrodes could introduces additional optical losses.

Table 19 summarizes the different values of the resistance of the VO_2 patch before the transition to the metallic state as function of the gap between the electrodes and their width.

Table 19: Resistance (kΩ) of the VO_2 patch before the transition to the metallic state.

Gap(µm)	W=5µm	W=10µm	W=20µm
0.5	6.81	3.44	1.99
1	8.61	5.06	3.33
2	6.36	7.02	5.3

Once the vanadium is switched to the metallic state, the resistance of the VO_2 patch is highly decreased. In fact, as it was described in Figure 87 and Figure 89, the slope of the I-V response is approximately equal to the load resistance. Figure 88 (b) shows the simplified equivalent circuit of the VO_2 junction with the load resistance. The selection of the load resistance is important in terms of power consumption but also due to its influence on the VO_2 phase transition. In the metallic state, the power consumption can be calculated as

$$P \approx \frac{V_{source}^2}{R_{load}}$$

It means that the power can be decreased by increasing the load resistance. Nevertheless, the vanadium dioxide phase transition is based on two successive steps. An electronic process based on the Poole-Frenkel effect followed by a thermal process characterized by thermal filamentation. The load resistance works as a current-limiting resistance so too high values for this resistance could limit the thermal process and reduce the optical absorption. On the other hand, if the external resistance is increased, the voltage over the vanadium dioxide junction is decreased so to maintain the required electric field it is necessary to increase the applied voltage. In this case, the power consumption will increase (as the voltage is squared in the power calculation) so a trade-off in the selection of the external resistance and the applied voltage is mandatory.

3.2.7. Proposal of a short-circuited electrode.

In an attempt to reduce the power consumption as well as simplifying the contacting scheme in the designed VO_2/Si microring switch [82], a short-circuited electrode configuration is proposed. The principle of operation is very simple as it is just to use the heat generated by the short-circuited electrode to change the state in the VO_2. Therefore, the structure shown in Figure 90 has been fabricated to characterize and analyze the electrode performance.

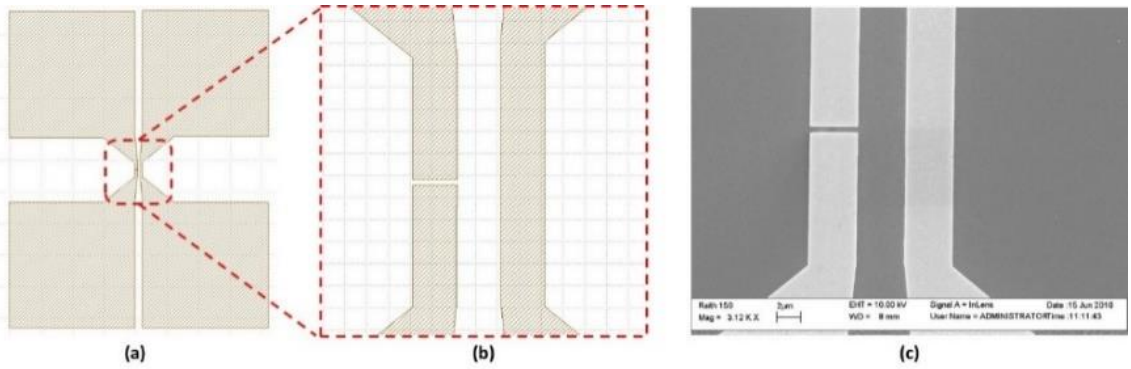

Figure 90: (a,b) Gds of the structure to characterize the short-circuited electrode. (c) SEM image of the fabricated structure.

The structure consist on two electrodes separated by a 4µm long VO_2 section. Figure 91 shows the electric schematic of the measurements. The electrode of the right side is the short-circuited electrode. When a voltage (V_1) is applied to this electrode, a very high current circulation (I_1) is obtained due to the low resistance of the electrode. This current gradually provides a temperature increment in the VO_2 that affects the insulator to metal transition performance of the electrode of the left side. Providing a temperature increment higher than 90 degrees, the VO_2 changes from the insulating to the metallic state.

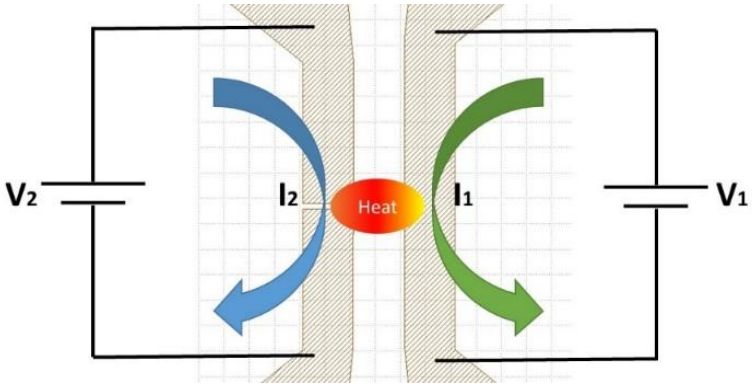

Figure 91: Electric schematic of the 4 probes measurements.

The electrode of the left side has a gap of 500nm and a width of 4µm. In this electrode, the application of a low voltage (V_2) provides a low circulation of current (I_2) due to the high resistance of the VO_2 section in its insulating state. Nevertheless, due to the temperature increment obtained by means of the short-circuited electrode, the resistance of the VO_2 section is reduced. This effect, increases the circulation of current through the electrode of the left side (I_2). Figure 92(a) shows the V-I response of the left side electrode as function of the current circulating through the short-circuited electrode. It is clearly seen how the required voltage to induce an abrupt change in the current is decreased when the current through the short–circuited electrode is increased due to the

temperature increment. With these measurements it is demonstrated the propagation of the generated heat along the VO_2 film. Figure 92(b) shows the required voltage to induce the VO_2 transition as function of the power applied to the short-circuited electrode. As the applied power is increased, the heat generated and propagated is increased so the required voltage to switch the VO_2 is reduced.

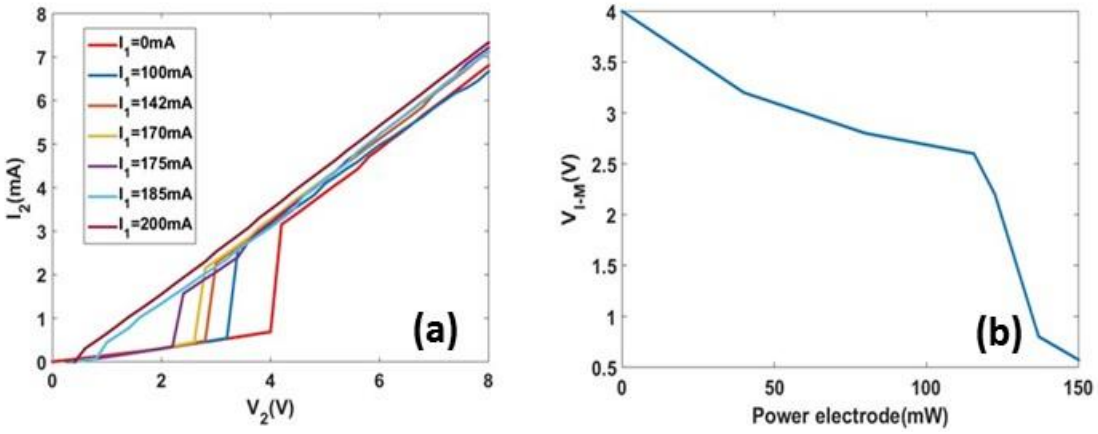

Figure 92: (a) V-I response of the left side electrode as function of the current circulating through the short-circuited electrode.(b) Required voltage to induce the semiconductor to metal transition as function of the electric power applied to the short circuited electrode.

From the results shown in Figure 92 it can be seen that a high current of around 200mA is required to change the VO_2 section between the electrodes to the metallic state. The high electrical current is in part due to the very low resistance of the short-circuited electrode, which is around 3.75Ω. However, the main point here is that the whole VO_2 section is completely changed as the electrode of the left side behaves as a short circuit. The required electrical power is around 150mW but this value can be improved by decreasing the distance between the two types of electrodes.

The proposed short circuited electrode has a lower power consumption compared to the non-short circuited electrodes shown in Figure 85. A comparison between the short circuited electrode and the non-short circuited one is shown in Figure 93. In both cases, the distance between the electrodes and the waveguide is the same (s). Therefore, in the non-short circuited, the gap distance between the metallic pads is the width of the waveguide plus two times the separation between the pad and the waveguide.

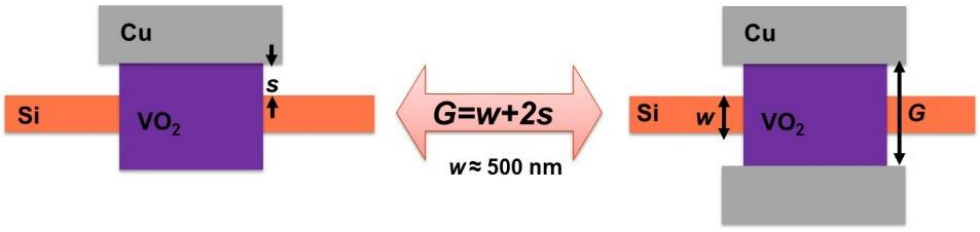

Figure 93: Comparison between the short circuited and the open circuited electrode structures. To establish the comparison, the distance between the electrode and the waveguide is the same in both structures.

In the short circuited electrode, the semiconductor to metal transition is induced by the current trough the electrode. This current provides a temperature increment which changes the vanadium dioxide towards the metallic state. In this case, the resistance of the electrode is extremely low (around 4Ω) and an external load resistance is not necessary to protect the vanadium dioxide. Therefore, the required power to achieve the transition can be calculated as follows,

$$P = I_{source}^2 \cdot R_{electrode}$$

Due to the low resistance of the electrode, high current levels can be obtained with low source voltage values. According to several thermal simulations carried out by COMSOL, the required applied power to achieve the phase transition, when the distance between the electrode and the waveguide is 1.5µm, is around 40mW.

On the other hand, in the non-short circuited electrode a load resistance is necessary to protect the device by limiting the current through the VO_2 in the metallic state. To compare with the short-circuited electrode, the gap between the pads is 3.5µm as it was depicted in Figure 93. Approximately, the required electric field in a VO_2 junction to induce the phase transition is around 10^7 V/m. It implies that, according to the gap of the device, an applied voltage of around 35V would be necessary. In this case, the required power to induce the phase transition can be calculated as follows,

$$P = \frac{V_{source}^2}{R_{load}}$$

Using a load resistance of 1kΩ, the required power to the phase transition is raised above 1W. According to the previous equation, increasing the load resistance would reduce the required power. Nevertheless, viewing the simplified electrical scheme shown in Figure 88(b), it is important to notice that if the load resistance is increased the voltage applied to the VO_2 junction is decreased. Therefore, as it

was discussed in the previous section, it would be necessary to increase the applied voltage which would result in a higher consumption.

3.2.8. Electro-optical characterization of VO_2/Si devices.

Once the phase transition of the VO_2 has been experimentally investigated in planar films, the electro-optical characterization of the designed VO_2/Si hybrid devices have been addressed.

The process steps for fabricating the VO_2/Si devices are shown in Figure 94. The structures have been fabricated on standard SOI samples from SOITEC wafers with a top silicon layer with a thickness of 220 nm (resistivity ρ ~1-10 Ωcm^{-1}, with a lightly p-doping of ~10^{15} cm^{-3}) and a buried oxide layer thickness of 2µm. Silicon waveguides were first fabricated based on an electron beam direct writing process performed on a coated 100 nm hydrogen silsesquioxane (HSQ) resist film. After developing the HSQ resist using TMAH as developer, the resist patterns were transferred into the SOI samples employing an also optimized Inductively Coupled Plasma-Reactive Ion Etching (ICP-RIE) process with fluoride gases (SF_6/C_4F_8). Grating couplers were exposed on a PMMA layer using a second electron beam direct writing process prior to a 70 nm-etching process also performed with ICP-RIE system. Summarizing, a two etching process was followed: (1) a 70nm-etch for the grating couplers and (2) a full-etch for the rest of the silicon structures.

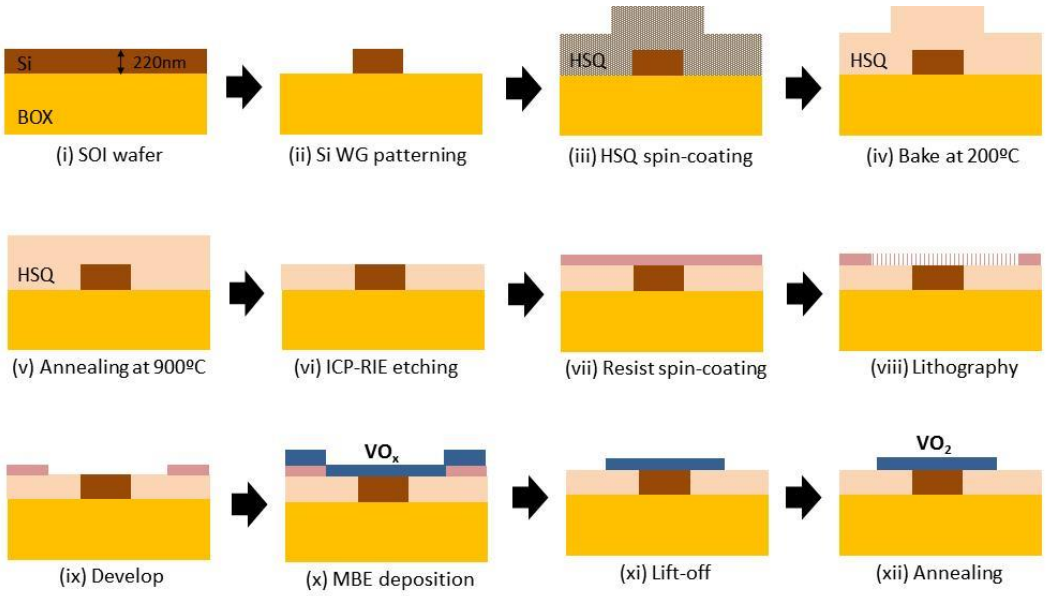

Figure 94: Process steps for fabricating the VO_2/Si devices.

The optimum waveguide design for the optical switch requires continuous VO_2 patchs over a section of the waveguide. According to the designs for TE and TM polarizations, the VO_2 patch should be placed directly over the waveguide or over a silica spacer of 25nm respectively. In order to achieve this, a planarization process is required to avoid an excessive quantity of silica over the waveguide. The samples made by IHP were planarized by CMP and the samples made in the NTC were planarized following the steps shown in Figure 94 (iii) to (vi), prior to the VO_2 deposition. The process is based on using the HSQ resist because it is a spin-on glass with good planarization properties and a silicon oxide-like behavior after annealing [83]. The HSQ is first spin-coated on the sample and baked at 200°C to remove the excess of dissolvent. The surface is planarized by annealing at 900°C and by etching by ICP-RIE up to the top of the silicon waveguide.

The fabrication of the VO_2 layer is based on molecular beam epitaxy (MBE) and a post-annealing process while a lift-off process has been chosen to pattern the layer. Patterning have not been based on reactive ion etching, due to the higher difficulty to align the VO_2 layer on top of the silicon waveguide [84]. The final steps of the fabrication process are depicted in Figure 94 (vii) to (viii). In this case, a PMMA resist is used. The regions where we want the VO_2 are defined by electron-beam lithography. MBE is used to deposit a VO_x layer and a lift-off process is followed to get rid of the VO_x in the undesired regions. Finally, a post-annealing process is carried out to form the VO_2 layer.

The process steps to fabricate the electrodes are shown in Figure 95. A similar lift-off process is again followed to define the contacts. A resist layer is placed over the sample by spin-coating. By means of a lithography and developing process the electrode pattern is transferred to the resist layer. Finally with a metal deposition and a lift-off, the metal contacts are placed.

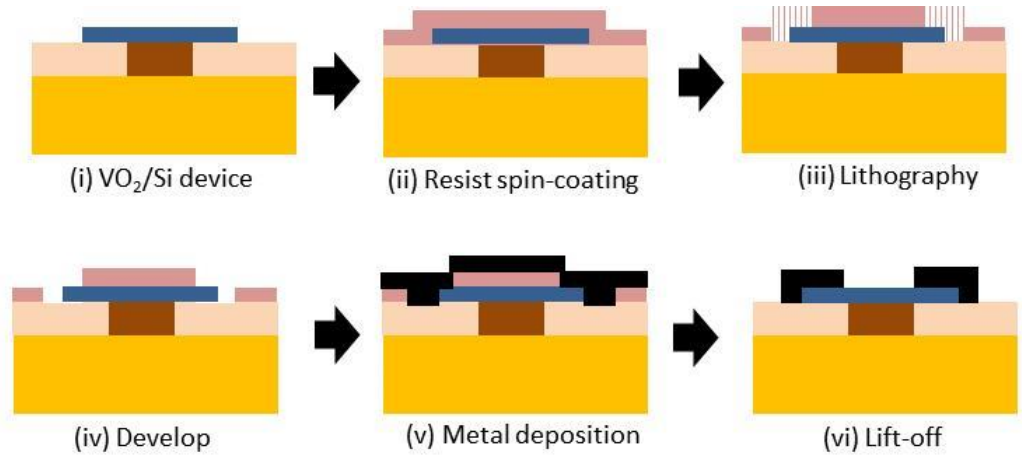

Figure 95: Process steps for the fabrication of the electrodes.

To check the usefulness of the HSQ as a substitute of silica, two identical copies were fabricated with a conventional SiO_2 upper-cladding deposited by PECVD and with the HSQ resist following the planarization process previously described. The objective were to characterize and demonstrate the proposed planarization process with optical measurements. Figure 96 shows the SEM images of the fabricated structures.

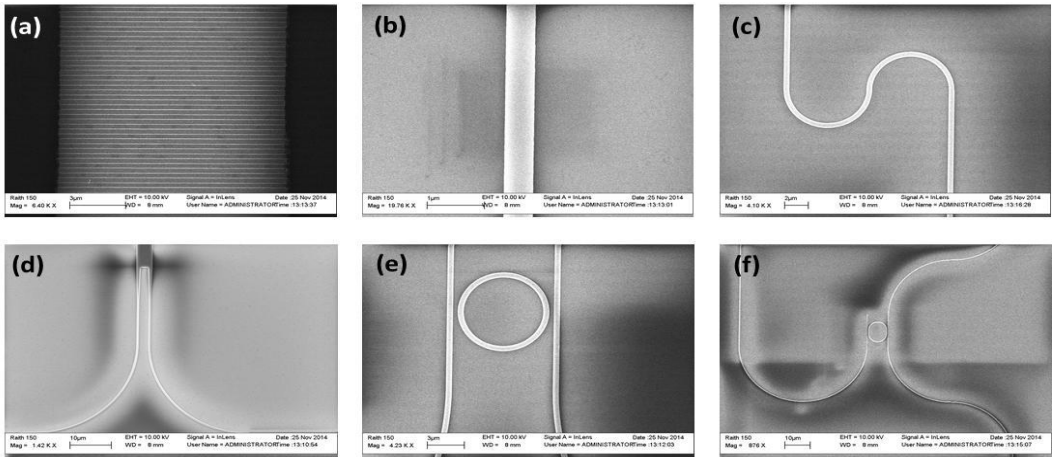

Figure 96: SEM images of fabricated structures: (a) grating coupler, (b) straight waveguide, (c) bent waveguide, (d) MMI and (e,f) add-drop ring resonator.

The most important characterization results for TE polarization are next summarized. Figure 97(a) shows the transmission response of several 500nm-wide silicon waveguides with SiO_2 and HSQ upper claddings as well as of the reference 12µm-wide silicon waveguide, which is used for alignment purposes. It can be seen that the response is similar for both SiO_2 and HSQ upper claddings. Furthermore, the transmission is also close to the reference waveguide, confirming the low propagation losses of the 500nm-wide waveguide (losses below 10dB/cm).

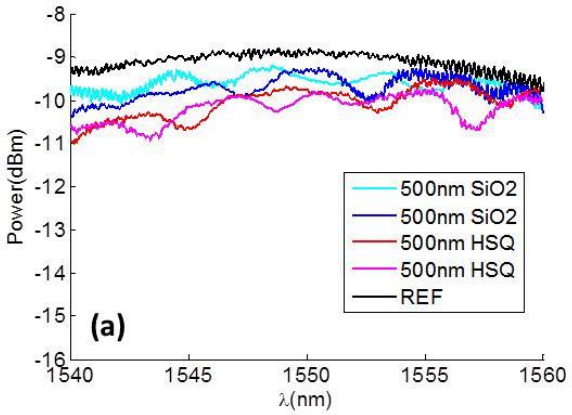

Figure 97: Experimental results of straight waveguides with silica or HSQ claddings.

Figure 98 shows the output power in the through (OUT_1) and drop (OUT_2) ports of the ring resonator with 2µm coupling length for the (a) SiO_2 and (b) HSQ upper claddings. It can be noticed once more that the response is almost identical. Furthermore, it can also be seen that the transmission response in the drop port has very low losses indicating low losses in the ring resonator structure. Bend losses around 0.1dB were measured.

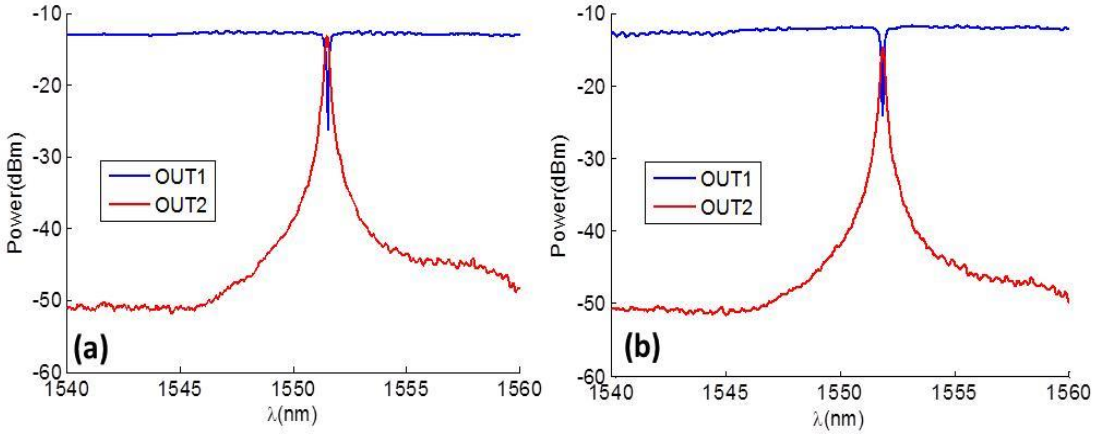

Figure 98: Experimental response of the ring resonator with (a) SiO_2 and (b) HSQ upper cladding.

The silicon structures fabricated and planarized at IHP, including waveguides and add-drop microring resonators, were first measured to characterize the passive performance before fabricating the active devices. Figure 99 shows (a) the gds file used to define the devices and (b) a photograph of the fabricated sample.

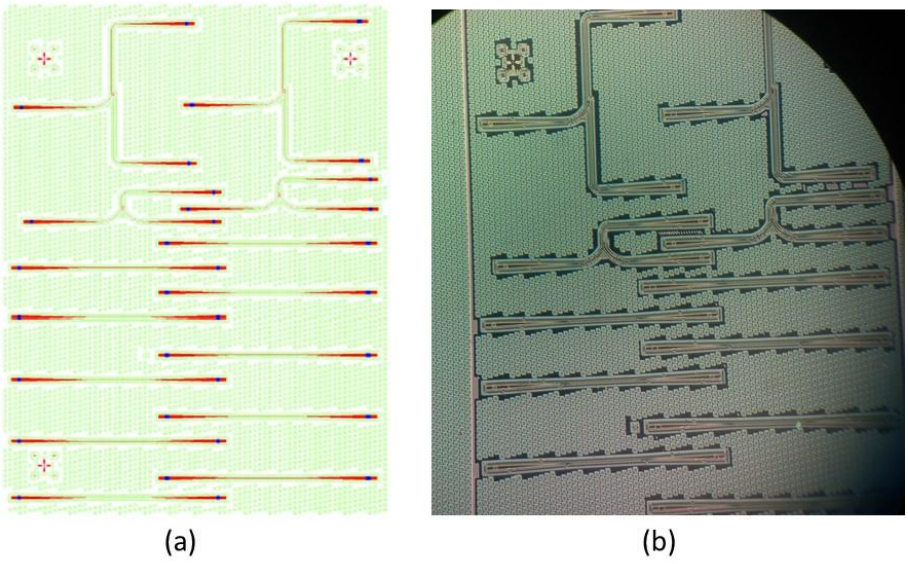

Figure 99: (a) Designed GDS of silicon structures and (b) fabricated sample at IHP.

This sample was planarized by CMP as it is shown in Figure 100. CMP provided a great planarization, yielding a perfect VO_2 deposition directly over the silicon waveguide.

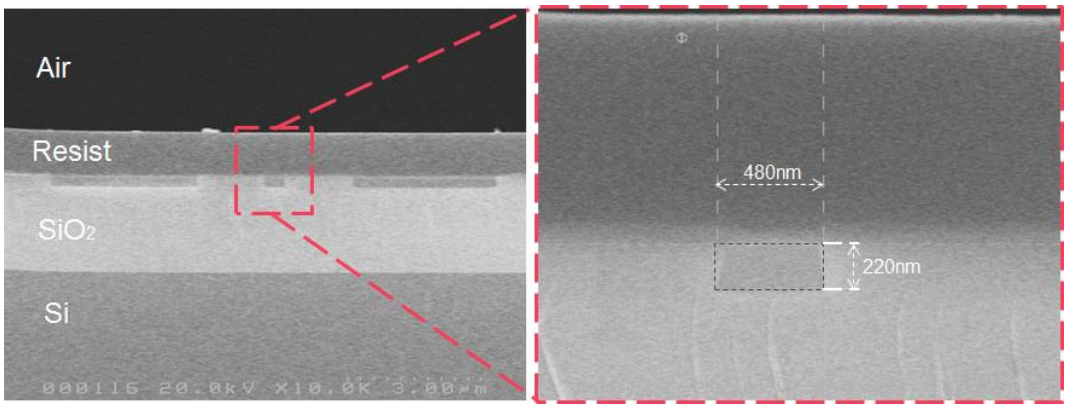

Figure 100: SEM image of the waveguide cross section. The CMP process provides a great planarization, allowing to a perfect VO_2 deposition directly over the silicon waveguide.

Figure 101(a) shows the spectral response of different silicon waveguides with the same length. It can be seen that there were a very good repetitivity and that propagation losses were low (<10dB/cm) since the estimated fiber-to-fiber coupling losses were around 10dB. Figure 101(b) shows the output power in the through (s_{11}) and drop (s_{12}) ports of the microring resonator. It can be seen that an extinction ratio higher than 15dB is achieved in the s_{11} response. Furthermore, almost negligible insertion losses at the ring resonance have also been obtained in the s_{12} response.

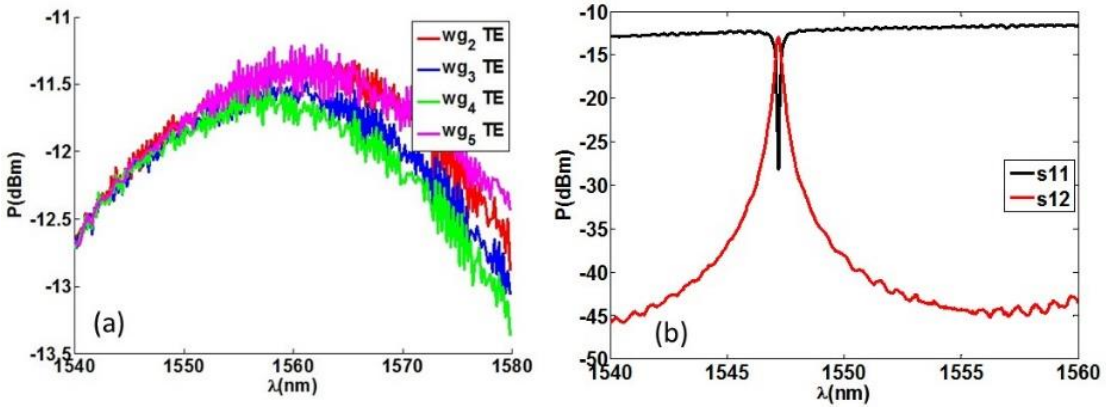

Figure 101: Spectral response of (a) different silicon waveguides with the same length and (b) an add-drop microring resonator.

Once the samples were passively characterized, they were completed with the VO_2 and electrodes deposition. Figure 102(a) shows the SEM image of a microring resonator with the VO_2 film and metal contacts. In this case, a thicker VO_2 film

(around 50nm) was grown to allow a stronger effect on the electro-optical response. The fabrication of the active devices with the VO_2 layer and metal contacts was more challenging due to the small size of the sample (around 2mm x 2mm). The small size of the sample made also trickier the electro-optical characterization, as it can be seen in Figure 102 (b).

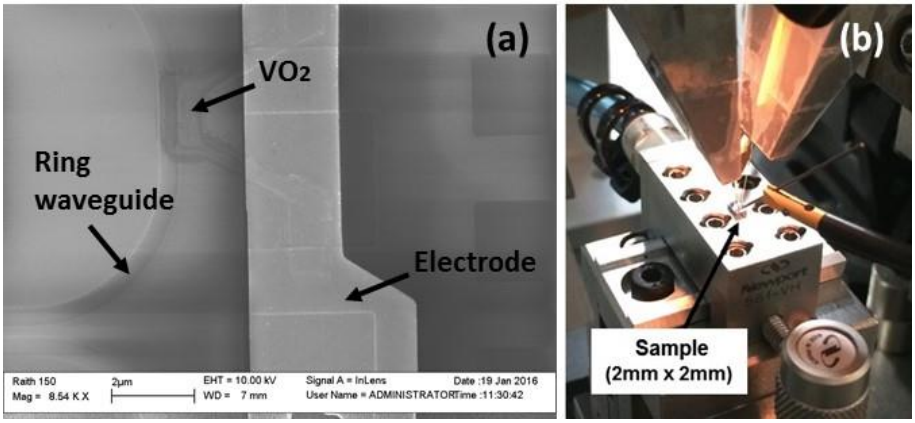

Figure 102: (a) SEM image of the microring resonator with the VO_2 film. (b) Detailed view of the sample electro-optical characterization.

Figure 103 shows the SEM image of a fabricated straight silicon waveguide with a hybrid section in the middle and the proposed short-circuited electrode to induce the switching of the VO_2. The inset shows a zoom of the hybrid section.

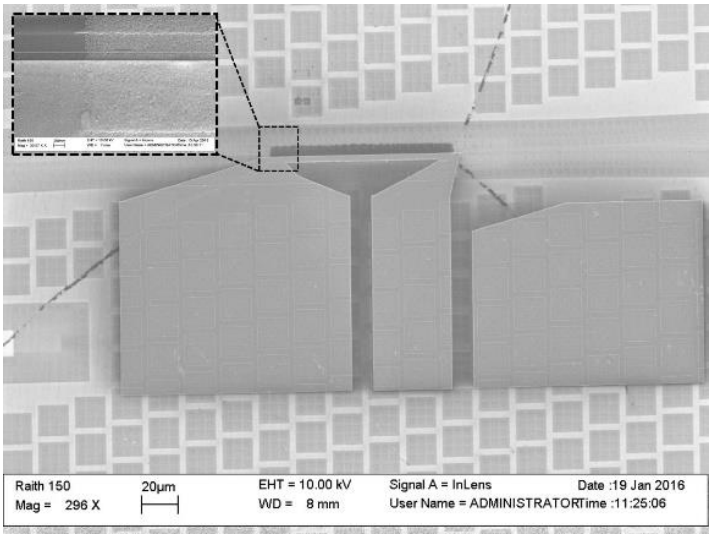

Figure 103: SEM image of a fabricated straight silicon waveguide with a hybrid section in the middle and a heater to induce the switching of the VO_2. The inset shows a zoom of the hybrid section.

The electro-optical control of the absorption in the straight waveguide by means of the proposed short-circuited electrode has been successfully demonstrated. In

this case, the distance between the electrode and the silicon waveguide has been reduced to 1.5µm to decrease the power consumption. The VO_2 fabrication and properties are the same than in the sample used to characterize the electrode. Figure 104 shows (a) the concept art of the straight waveguide with the VO_2 patch and (b) the optical spectrum of the device as function of two different values of applied power to the heater.

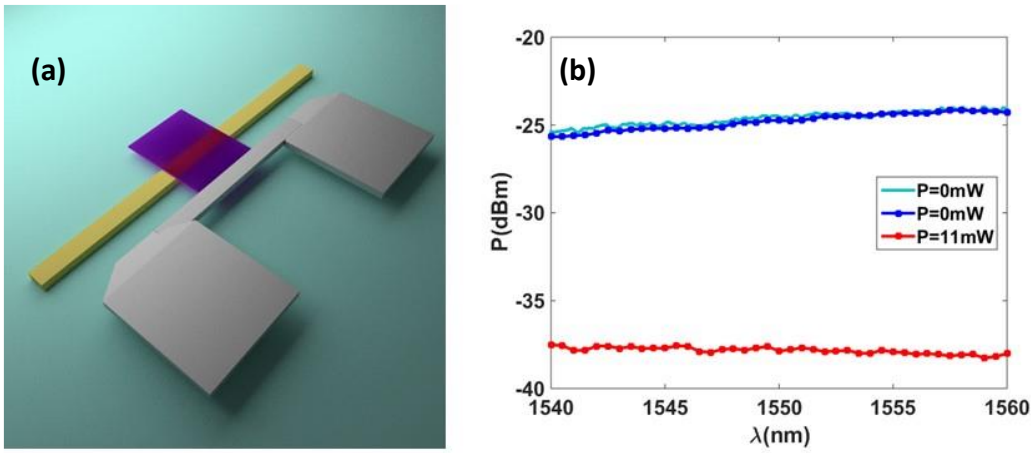

Figure 104: (a) Concept art of the straight waveguide with a hybrid VO_2-Si section with the proposed short-circuited electrode. (b) Optical spectrum depending on the power of the applied electrical signal.

The propagation losses of the hybrid VO_2/Si waveguide depend on the state of the VO_2. At steady conditions, the VO_2 is in the insulating state and we have the lowest losses. So first, the device was characterized without applying any power to the heater (P_{OFF}). Then the power was gradually increased until an abrupt change in the absorption was detected. First, the generated heat switches the VO_2 below the electrode. In the VO_2 patch, a temperature gradient determines the VO_2 areas switched to the metallic state. Applying more power to the electrode, the generated heat is high enough to reach a temperature above 70ºC in the whole VO_2 patch. In this way, by switching the VO_2 over the waveguide, the optical absorption is increased. When applying 11mW to the electrode, the VO_2 over the waveguide is switched towards the metallic state. Therefore, propagation losses in the hybrid VO_2/Si waveguide are highly increased which provokes an increment in the optical absorption of the waveguide of around 13dB. Higher optical absorption should be achieved in the metallic state according to the simulations. Unfortunately, electrodes were damaged at higher electrical powers due to the lower thermal conductivity of the oxide below the VO_2. Nevertheless, it was confirmed that the change between the two states was reversible and reproducible. It can be seen in Figure 104 (b) that when the electrical power was removed, the

optical losses returned to the original value, which confirms the switching back of the VO_2 to the insulating state.

Thermal simulations based on the finite element method (FEM) have also been carried out with COMSOL Multiphysics™ to analyze the heat transfer response and evaluate the impact on the power consumption. In Figure 104(b), the power of 11mW was obtained for a current of 55mA. Figure 105 shows the temperature as function of the distance from the center of the short-circuited electrode and for different electrical currents. In the simulations, with a current of 60mA, the temperature below the electrode is close to the transition temperature (T_{MIT} =70ºC) of the VO_2. However, it should be noticed that we have considered the thermal and electrical conductivities of the insulting state. Therefore, this approach does not consider the change in the conductivities when the VO_2 reaches the transition temperature. In the real device, it is expected that when the electrode is heating the VO_2 above its transition temperature, several regions would be switched to the metallic state. The conductivities of those regions will be increased providing a higher temperature along the VO_2 patch. Therefore, the heat transfer process will become more efficient. Nevertheless, according to the results shown in Figure 105, a current of 100mA would increase the temperature of the VO_2 on top of the silicon waveguide close to the transition temperature.

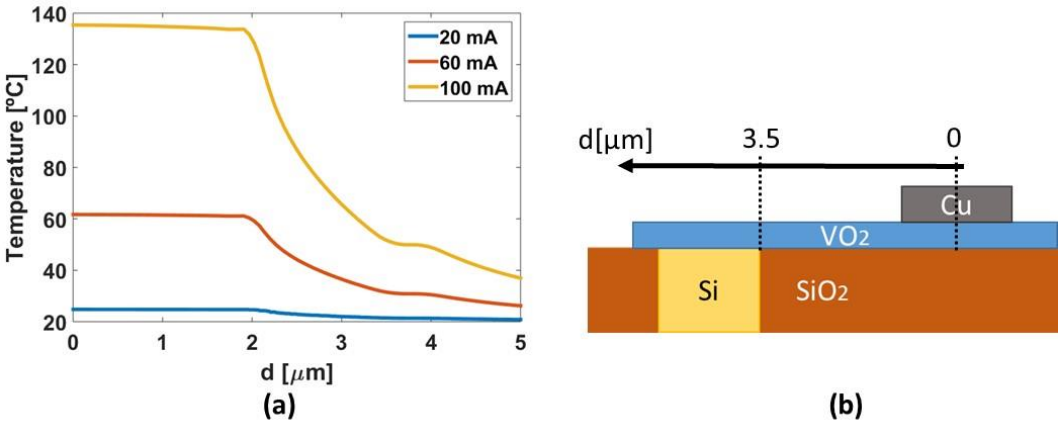

Figure 105: (a) Temperature as function of the distance from the center of the short-circuited electrode for different electrical currents. (b) Cross section of the simulated structure taking into account the influence on a silicon waveguide.

The electrical power required to achieve a current of 100mA in the proposed short-circuited electrode will be around 37.5mW. A significantly higher power would be needed by using the conventional electrodes shown in Figure 85 with a gap of 3.5µm (assuming a silicon waveguide width of 500nm). It should be noticed that the power needed to switch to the metallic state was higher than 50mW for a gap of only 2µm (Table 18). Therefore, the proposed short-circuited electrode

will clearly reduce the power consumption. Furthermore, the minimum distance to the silicon waveguide will be determined by the optical losses. Hence, values as low as 500nm would be possible which would minimize the power consumption.

Once the switching of the vanadium dioxide has been demonstrated in the straight waveguide, the proposed short-circuited electrodes have been used to control the VO_2 state in the designed VO_2/Si switch device [82]. Figure 107 shows (a) the concept art of the ring resonator with the hybrid VO_2/Si waveguide integrated and (b) the SEM image of the fabricated device. The switch is based on a 2x2 microring resonator with a radius of 3.5µm switched by means of a 2µm-long hybrid VO_2/Si waveguide placed on the microring.

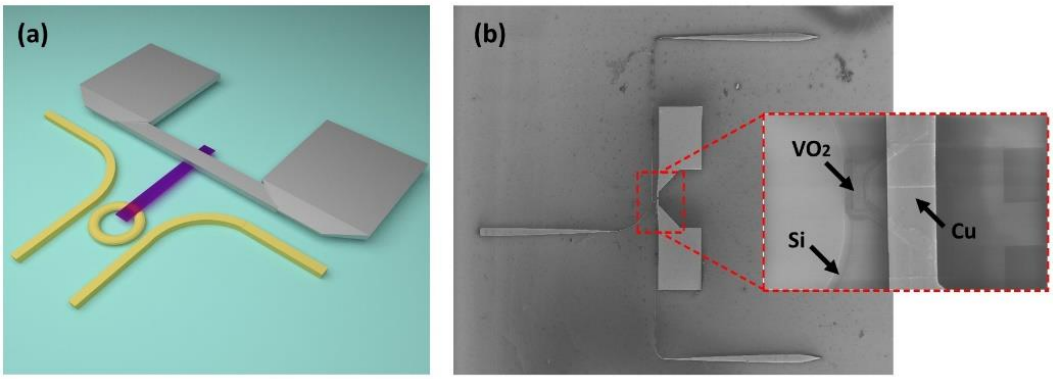

Figure 106: (a) Concept art of the simulated ring resonator with the VO_2/Si waveguide integrated. (b) SEM image of the fabricated device.

Figure 107 shows the optical response at the (a) through and (b) drop ports when an electrical power is applied to the electrode. The distance between the electrode and the hybrid VO_2/Si waveguide has been 1.5µm.

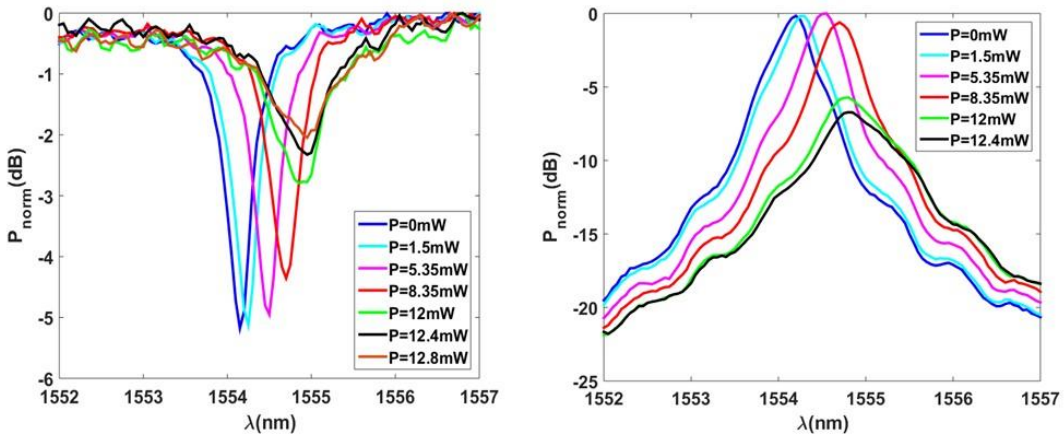

Figure 107: Optical spectrum as function of the applied power for the (a) through port and (b) drop port.

It can be clearly seen that, when the applied power increases, the generated heat gradually switches the VO_2 towards the metallic state thus increasing the ring losses. The depth of the resonance in the through port is reduced while the losses in the cross port are increased. On the other hand, it can be noticed that due to the change in the real part of the effective refractive index of the VO_2, a blue shift of the resonance should also be expected. Figure 108 shows the simulated results of the spectral response without and with the VO_2 film. For the insulating state, the higher losses in the VO_2/Si section of the microring structure increase the bandwidth of the resonance, decrease the extinction ratio and the resonance is shifted to higher wavelengths. On the other hand, for the metallic state the resonance is almost eliminated and shifted to lower wavelengths.

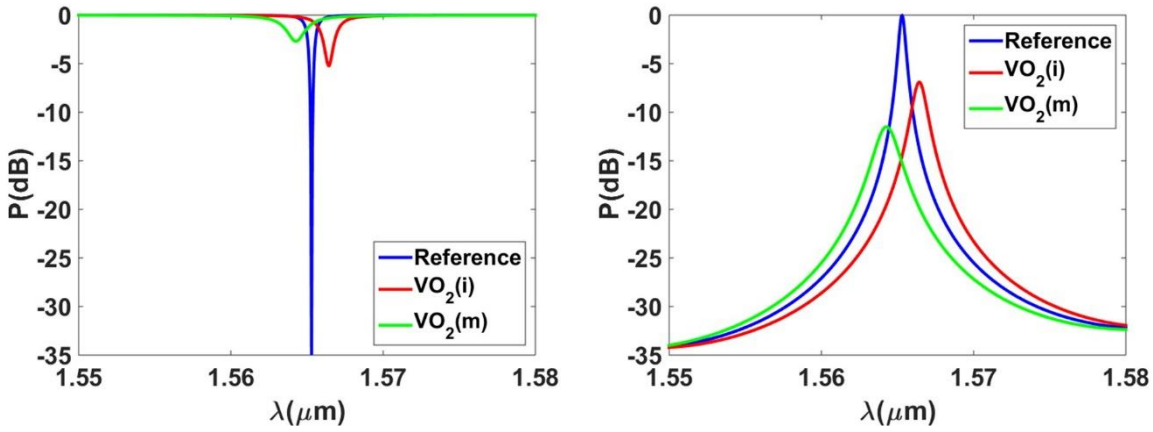

Figure 108: (a) Simulated results of the microring resonator spectral response without and with the VO_2 film. Thermo-optic effect in silicon is not considered.

Nevertheless, in the measurements shown in Figure 107, changing towards the metallic state, the resonance is slightly shifted to higher wavelengths instead of to lower wavelengths. This effect is due to the temperature increment of the silicon waveguide provoked by the heat generated by the heater. The thermo-optic effect in silicon provokes a shift towards higher wavelengths. Therefore, although the change from the insulating to the metallic state of the VO_2 provides a blue shift, the resonance is displaced towards higher wavelengths because the redshift contribution of the thermo-optic effect is stronger. The resonance shift is helpful to improve the insertion loss and extinction ratio at the bar state. Hence, the insertion losses are below 0.5dB and the crosstalk is higher than 20dB at the bar state (P=12.4mW). Conversely, the insertion losses at the cross state (P=0mW) are close to 8dB due to the high losses of the VO_2 in the insulating state. However, insertion losses could be improved either by increasing the silica spacer thickness between the VO_2 layer and the silicon waveguide or reducing the VO_2 thickness, as it was previously shown.

Figure 109 (a) shows the variation of the normalized power at the ring resonance as function of the applied electrical power in both through and drop ports. Experimental results are compared with the simulated values shown in Figure 109 (b) as a function of the variation of the optical losses in the microring. It can be seen that both results are consistent although the variation is somewhat different. In the experimental results, the variation of the ring resonance is almost negligible for an applied power below 5mW. This behavior is because the electrode has not generated enough heat to switch the VO_2 over the silicon waveguide. On the contrary, for higher applied powers, the amplitude of the resonance is rapidly reduced, especially in the drop port, due to the larger propagation losses in the hybrid VO_2/Si waveguide.

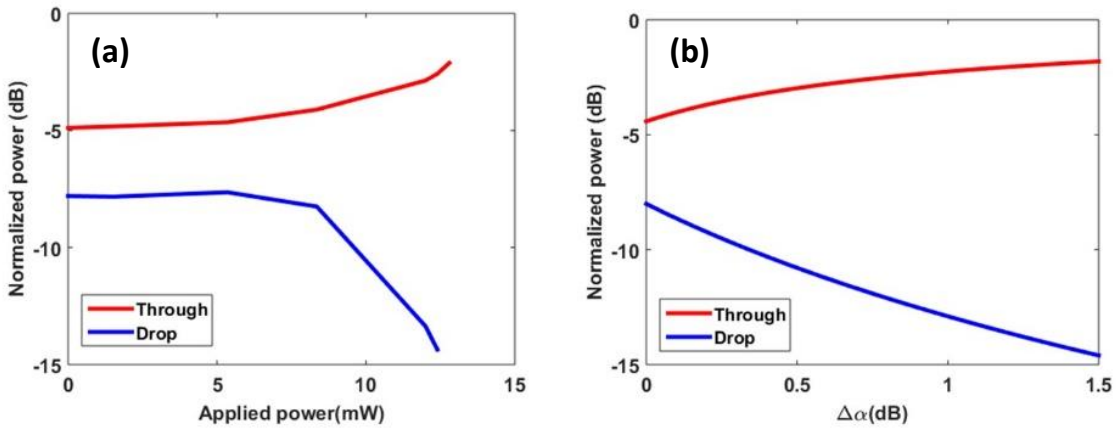

Figure 109: (a) Variation of the normalized power as function of the applied electrical power and (b) simulated variation as a function of the change of optical losses in the microring.

The slow temporal response of the optical switch has also been characterized. We were not able to measure the switching time because the electrodes were not adapted to the available RF probes. Nevertheless, a voltage pulse train with maximum voltage that corresponds to a power of around 12mW was used to characterize the slow temporal response. The obtained optical response is shown in Figure 14. An extinction ratio of around 3dB and 8dB is obtained at the through and drop ports respectively. It can also be seen that the device response is stable and that the switching between states is reversible and reproducible.

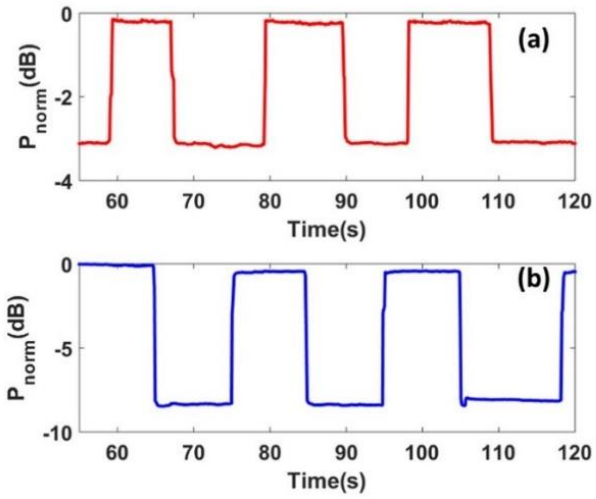

Figure 110: Temporal response of the optical switch at the (a) through and (b) drop ports.

In summary, the analysis and design optimization of a 2x2 optical switch based on a hybrid VO_2/Si microring structure has been carried out for both TE and TM polarizations. Extremely short active lengths have been demonstrated thus yielding to compact footprints lower than 100μm^2. The preferred polarization for the switch is TE due to the better transmission performance and negligible coupling losses with the silicon waveguide. Furthermore, most of the photonic circuits based on silicon photonics work also with TE polarization and a smaller radius, and therefore a more compact switching device, can also be achieved due to the smaller bending losses compared to TM polarization. Simulations show insertion losses below 1.8dB and crosstalk values above 12dB. Insertion losses can be lowered if the imaginary part of the VO_2 refractive index at the insulating state could be decreased. However, it should be noticed that in this case a higher transmission coefficient would also be required that would reduce the optical bandwidth of the switch. In the proposed device, the data throughput rate at a single optical wavelength will be higher than 500Gbps thus proving VO_2/Si technology as a promising approach for the development of switches with high throughput bandwidth, low power consumption, small footprint and compatibility with silicon CMOS photonics. This work has been published in Photonics Journal [82] and in the 12th International Conference on Group IV Photonics 2015 [85].

After the design, an experimental characterization of a device has been carried out. The control of the optical properties by means of the SMT in VO_2 has been demonstrated. A significant change of optical absorption has been achieved using a 2μm long hybrid VO_2/Silicon waveguide integrated in a ring resonator. The SMT was achieved by means of the generated heat in a novel short-circuit

electrode. In this way, a robust device which allows using high electrical power levels without collapsing the electrode was demonstrated.

Chapter 4

VO_2 as active material for other applications

The disruptive properties of the vanadium dioxide like its hysteretic behavior and the large change in the refractive index due to its phase transition allow the development of outstanding photonic applications. Figure 111 shows different potential applications depending on the exploited characteristic of the vanadium dioxide.

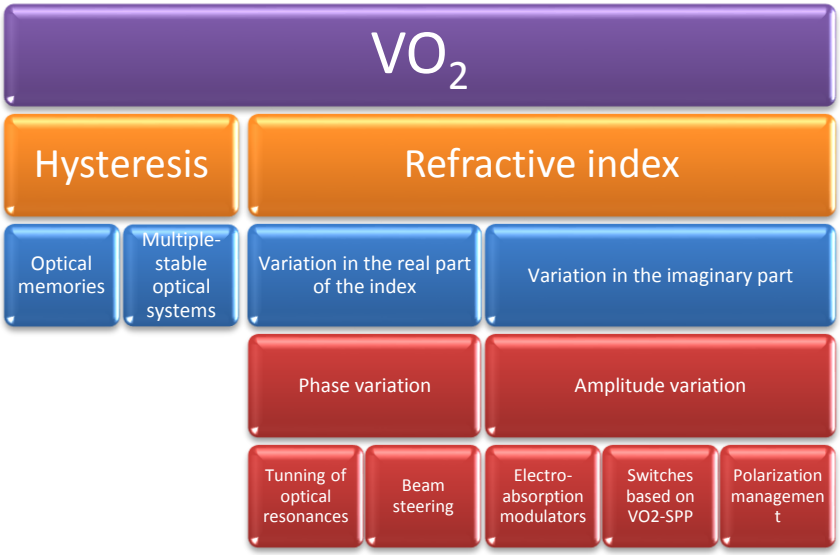

Figure 111: Potential photonics applications based on the optical properties of the VO_2.

Among the different applications offered by the vanadium dioxide, the use of the absorption and phase changes arising from its phase transition have been used for the development of electro-absorber modulators and switches [86-89]. The most common ways to combine VO_2 with silicon photonics in these devices is placing

thin films of VO_2 over a silicon waveguide or introducing the VO_2 in a slot structure. With the VO_2 over the silicon waveguide, the interaction of the TE fundamental mode with the VO_2 is weaker than with the transverse magnetic polarization due to the different shape of the modes. Polarizers, switches and modulators have been reported with this distribution. The slot configuration is very useful to enhance the interaction of the field with the vanadium dioxide to exploit, as instance, the change in the absorption. Recently, several modulators have been proposed [67].

The hysteretic behavior in the electrical and optical properties of the VO_2 also paves the way to the development of devices with different stable states. The hysteretic performance of its electrical properties has been recently used in the demonstration of MEMs or multi-state memories [90-93] while the optical hysteresis can be used to develop photonic devices based on optical bistability, allowing the development of optical memories.

In the next sections, the VO_2/Si hybrid technology has been used for the design of different electro-absorption modulators for TE and TM polarization. Furthermore, these technology is also used to propose a novel optical memory, an smart bionanosensor and a tunable metamaterial.

4.1. Electro absorption modulation.

The hybrid VO_2-Silicon waveguide provides a simple structure useful for the implementation of electro-absorption modulators. As we have mentioned in previous sections, the SMT of VO_2 provides a huge change in the effective refractive index of the structure, giving rise to a phase variation in interferometric or resonant structures. But also, provides an abrupt absorption change. It means that the hybrid waveguide performs as an electro-absorption modulator controlled by means of the VO_2 SMT. Figure 112 shows a concept art of the electro-absorption modulator and a schematic of its cross section.

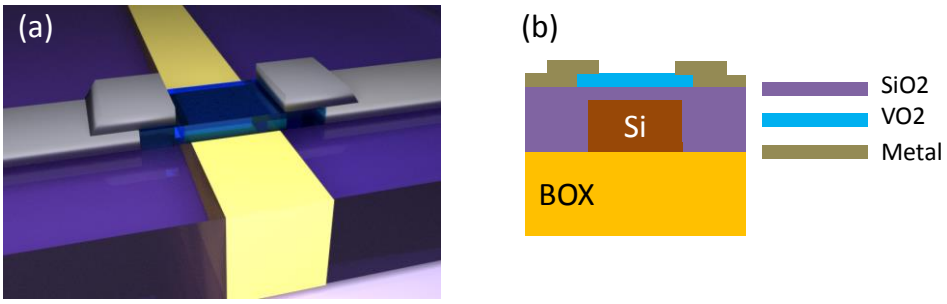

Figure 112: (a) Concept art of the electro-absorption modulator. (b) Cross section of the hybrid VO_2/Si waveguide.

A VO_2 layer is grown over the silicon waveguide. Metallic electrodes at both sides of the VO_2 allow the application of the electric field to induce the SMT. Without power applied, at steady conditions, the VO_2 layer remains in insulating state. In contrast, applying a power level enough high to induce the SMT, the VO_2 layer switches to the metallic state. The low losses in the insulating state and high losses in the metallic provides an extinction ratio that encodes the external stimuli applied to the VO_2 in the optical signal. Due to the different modal shape of the TE and TM modes, the thickness of the VO_2 layer and the height of the silica spacer are designed taking into account the input polarization. TE modes are more confined inside the silicon waveguide so the interaction with the VO_2 layer is lower while TM modes have a more intense interaction with the VO_2.

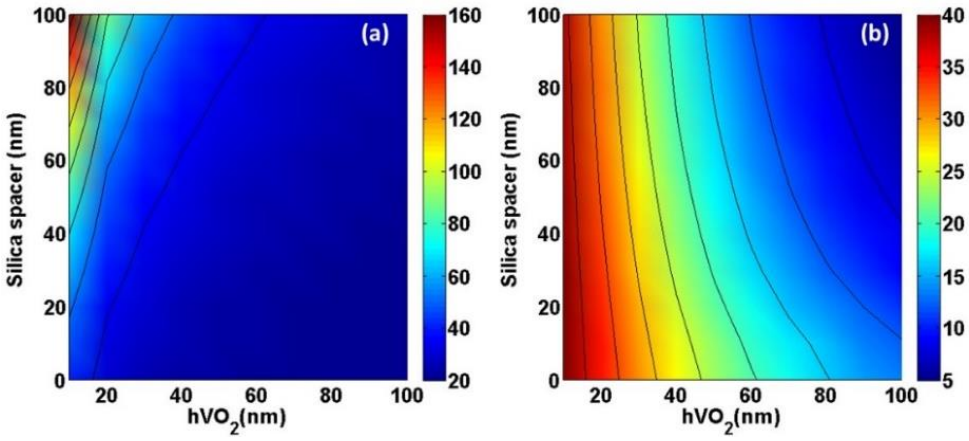

Figure 113: Active length (a) and extinction ratio (b) as function of the spacer and the VO_2 thickness for insertion losses of 5dB and TE polarization.

Figure 113 shows the active length and the extinction ratio for TE polarization as function of the VO_2 thickness and the silica spacer for a value of insertion losses of 5dB. Extinction ratio above 40dB for devices with an active length of 30μm is obtained using thin VO_2 films directly grown over the silicon waveguide. The same extinction ratio is achievable for higher values of silica spacer but the active length is largely increased.

In order to check the performance, 3D-FDTD simulations of the optimized structure have been carried out. Figure 114 shows the performance of the device for TE input polarization when the VO_2 is in the (a,b) insulating and (c,d) metallic states. For each case, top and lateral views are displayed. It is clearly shown how the field is highly attenuated in the metallic state while in the insulating state the insertion losses are around 5dB.

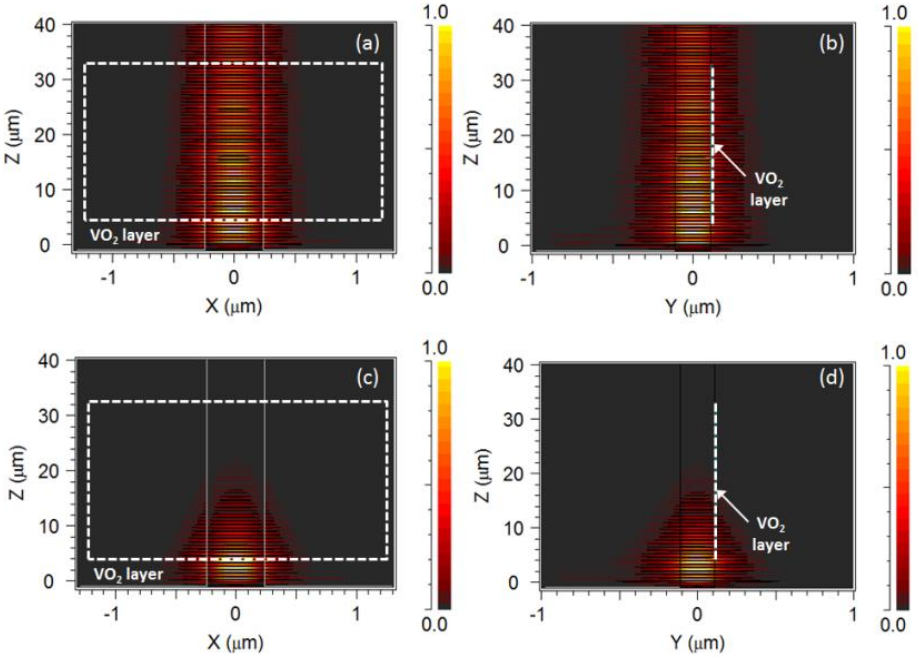

Figure 114: TE performance for the (a,b) insulating and (c,d) metallic states. Top and lateral views.

Figure 115 shows the spectrum for the insulating and the metallic states. For a wavelength range of 100nm the insertion losses are maintained below 5dB while for the metallic state the losses are higher than 50dB. The losses for the metallic state are somewhat higher than the predicted with the mode solver.

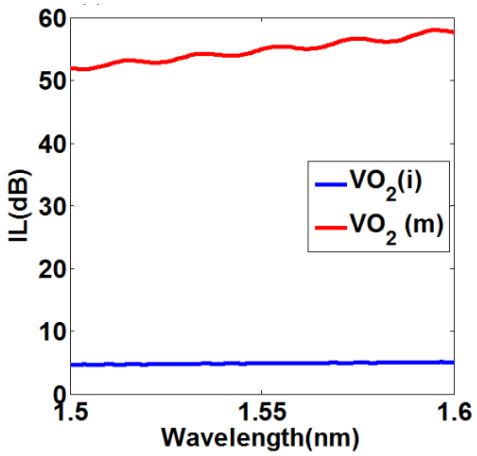

Figure 115: Optical spectrum for both VO_2 states is shown for a range of 100nm.

For TM polarization, Figure 116 shows the active length and the extinction ratio as function of the VO_2 thickness and the silica spacer for a value of insertion losses of 5dB. There is a local extinction ratio maximum above 250dB for a compact active length of only 6.2μm.

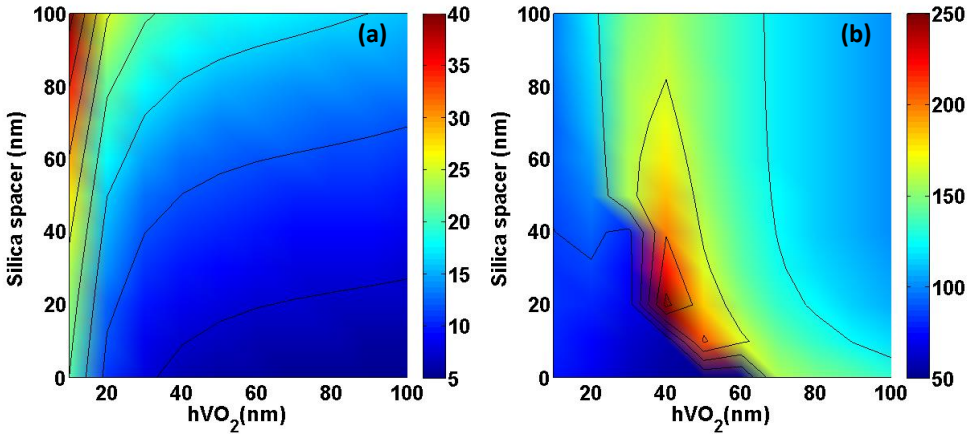

Figure 116: Active length (a) and extinction ratio (b) as function of the spacer and the VO_2 thickness for insertion losses of 5dB and TM polarization.

Nevertheless, Figure 117 shows the 3D-FDTD simulations and the extinction ratio is one order of magnitude lower than the expected with the mode solver. To achieve the performance described in Figure 116, a highly lossy slot mode in the metallic state must be excited. Hence, a structure based on an adiabatic taper to achieve the transition from the TM mode of the input waveguide to the slot mode of the hybrid waveguide section is required.

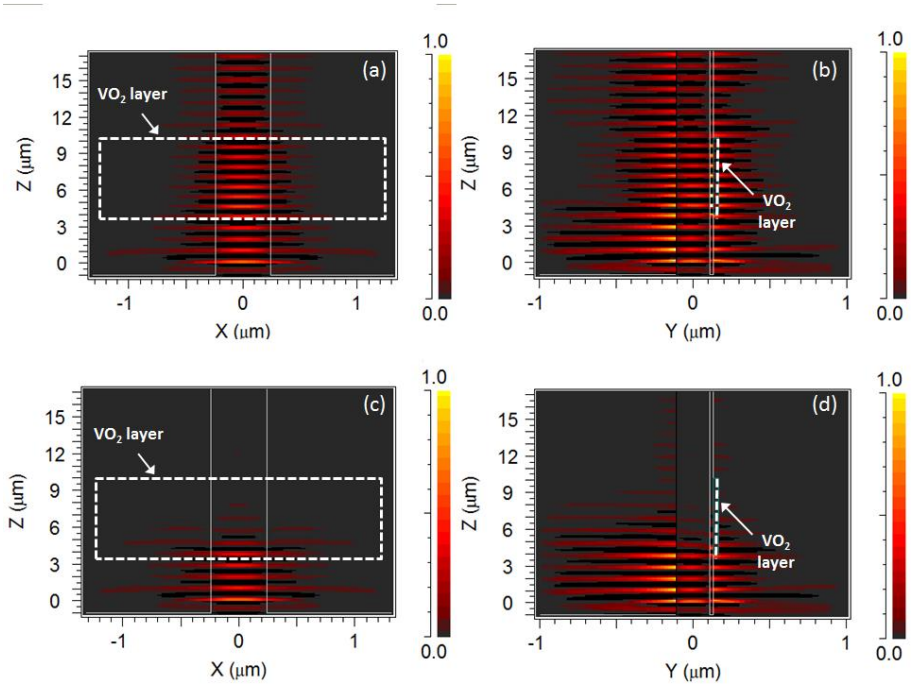

Figure 117: TM performance for the (a,b) insulating and (c,d) and metallic states. Top and lateral views.

Table 20 shows a summary of the active length and extinction ratio as function of the input polarization and the insertion losses for the optimized values of silica

spacer and VO_2 thickness. The results are obtained by means of the mode solver and for TM polarization, the slot mode highly lossy in the metallic state is considered.

Table 20: Active length and extinction ratio as function of the insertion losses and the input polarization.

	TE polarization (h=0 nm,h_{VO2}=10 nm)		**TM polarization (h=20 nm,h_{VO2}=40 mn)**	
IL	L(μm)	ER(dB)	L(μm)	ER(dB)
0.5	2.9	4.4	0.6	26.2
1	5.8	8.7	1.2	52.5
5	28.8	43.6	6.2	262

4.2. Electro absorption modulation with polarization rotation.

Vanadium dioxide films over a silicon waveguide is the easiest way to combine both materials for photonic applications. According to the results showed in Table 20, with this distribution, ultra-compact TM modulators with higher ERs than TE modulators are possible. Nevertheless the 3D-FDTD simulations confirmed the necessity of additional coupling structures to excite a slot mode highly lossy to achieve the described performance. Furthermore, it is important to remark that silicon photonic components are usually designed to work with TE polarization. To circumvent the issue of the low performance of the TE modulators based on the SMT of the vanadium dioxide, different topologies have been studied to obtain a higher interaction between the TE mode and the VO_2 active layer. Table 21 and Table 22 show the comparison with respect several works, with experimental or simulated results respectively, which exploit the absorption variation of VO_2 films in optical devices for TM or TE polarization. In order to establish a comparison, the figure of merit ($\frac{ER}{IL}$) proposed in [87], has been obtained for each case.

Table 21: Comparison with the state of the art of fabricated devices. Our device performance is simulation based.

Ref	**Polarization**	**LVO_2 (μm)**	**IL(dB)**	**ER(dB)**	**ER/IL [87]**
[86]	--	--	2	26	13
[49]	TE	2	2	6.5	3.2
[66]	TM	7	6	16.4	2.7
[61]	TE	1	2	4	2
[63]	TE	1	5	12	2.4
[78]	TM	2.5	0.25	2	8
Our work	TE	6	0.3	11	36.6

Table 22: Comparison with the state of the art of simulated devices.

Ref	Polarization	LVO_2 (µm)	IL(dB)	ER(dB)	ER/IL [87]
[87]	--	5	4.5/1.5	32.1/22.7	7/15
[65]	--	0.2	2	10	5
[67]	TM	9.47	0.77	3	3.9
[68]	TE/TM	0.5	2.73/1.79	3.9/8.7	1.4/4.8
Our work	TE	6	0.3	11	36.6

Therefore, the main objective is the development of TE modulators based on vanadium dioxide with a performance as good as the showed by the TM modulators without hardening the fabrication. According to these statements, we have proposed an enhanced electro-absorption VO_2/Si modulator with TM to TE conversion which reduces insertion losses and improves the extinction ratio. The proposed device has a length of 6µm and achieve the best trade-off between insertion losses and extinction ratio, as shown in Table 21 and Table 22.

A key parameter in modulators based on VO_2 is the modulation speed. In our modulator, the maximum speed would not be limited by the electrode geometry due to its extremely compact length. The modulation speed would therefore be limited by the dynamics of the SMT. Recently, several works [63,78] have experimentally studied the SMT to characterize the switching time of the transition between the two states of the VO_2. The speed of the modulator is actually limited by the metal to insulator transition because it is necessary to reduce the temperature reached by the VO_2 layer. However, switching times as low as 3ns have been experimentally demonstrated for the reverse transition [78]. Furthermore, several ways to reduce the time of this transition as reducing the switching pulse duration have also been proposed.

Figure 118 shows the device, which is based on a coupler structure. When the VO_2 is in the insulating state, the TM input is switched to the cross port of the coupler structure and rotated into a TE mode. The achieved insertion losses are below 0.3dB and the polarization extinction ratio above 30dB at the optical wavelength of 1.55µm. In contrast, for the VO_2 metallic state, the optical signal is attenuated at the output giving rise to an extinction ratio of 11dB. Therefore, by controlling the VO_2 state, the TM input provides a TE output which can be modulated by the electric pattern applied to the electrodes. Furthemore, the proposed device operates in a broadband wavelength range of 60nm with insertion losses below 0.5dB and modulation extinction ratios above 10dB.

Inset in Figure 118 shows the structure parameters. A silicon waveguide ($w_{Si} \cdot h_{Si}$) is used as an input port to introduce the optical signal. A hybrid Si/SiO_2/VO_2/Ag

waveguide is placed next to the silicon waveguide separated by a coupling gap (D). The electrode topology would take profit of the metallic layer as one of the contacts while a silicon area, with a negligible effect on the optical mode, would be defined at the side of the waveguide hybrid section to form the other contact [68,94]. The width of the hybrid waveguide is w_H and the thickness of the silica layer and the VO_2 layer are h_{SiO2} and h_{VO2} respectively.

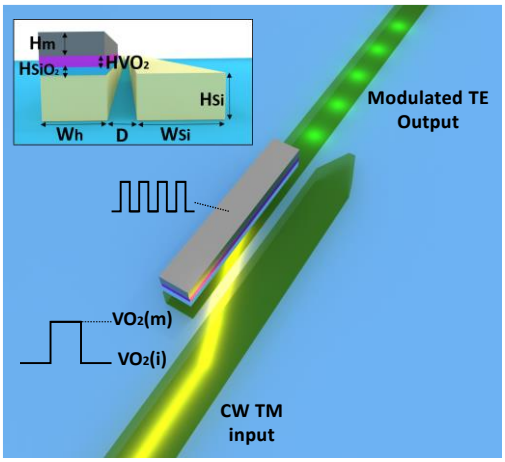

Figure 118: 3D Concept art of the performance for TM input polarization. The vanadium dioxide is switched between its different states by applying electric pulses, so the generated TE output is patterned. In the inset, a front view of the input waveguide and the hybrid waveguide is showed.

Mode coupling between the waveguides requires that their modes have the same effective refractive index to satisfy the phase matching condition [95,96]. Therefore, for the insulating phase (steady conditions), the effective refractive index of the TM input mode must have the same value than the TE mode of the hybrid waveguide. In such a way, the TM mode couples to the hybrid waveguide and is rotated into the TE mode. On the other hand, when the VO_2 is in the metallic state, the change of the refractive index gives rise to a phase mismatch that, together with high absorbing losses, maximize the extinction ratio of the modulator.

All the structural dimensions have been optimized to ensure the phase matching condition when the VO_2 is at its insulating state. The height of the silicon has been fixed to 220nm in both waveguides in order to use a standard SOI wafer. Furthermore, a 100nm thick silver layer (h_m) has been considered. For a silicon waveguide surrounded by air, the TM mode has an effective index of 1.58 for a width of 500nm. In the hybrid waveguide, a width of 320nm has been defined from preliminary simulations whereas the thicknesses of the silica spacer and the VO_2 film have been optimized. Figure 119(a) shows the real part of effective

refractive index for the TE mode of the 320nm wide-hybrid waveguide as function of h_{SiO2} and h_{VO2} for the VO_2 insulating state. A black isocurve for $n_{eff} = 1.58$ has been added on the contour plot. The best coupling condition between the waveguides will be achieved by any h_{SiO2}/h_{VO2} combination lying in this isocurve. From this curve, the VO_2 thickness is defined once the SiO_2 thickness is chosen.

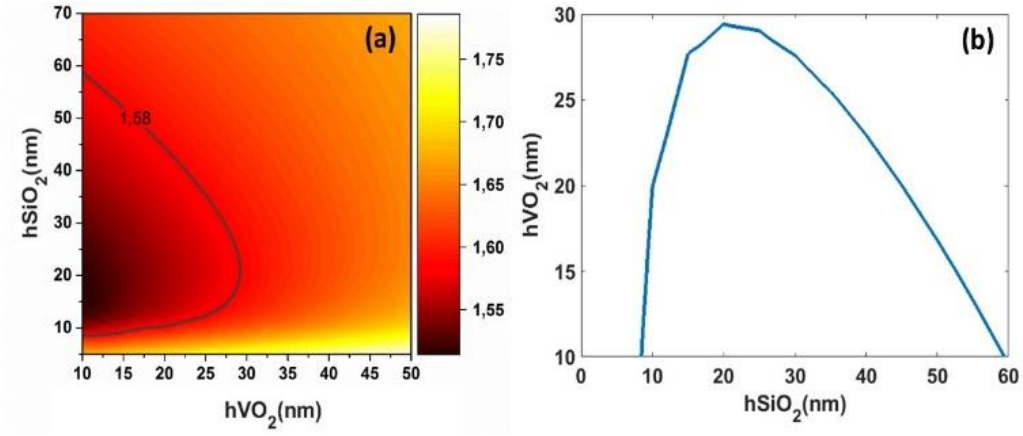

Figure 119: (a) Real part of the effective refractive index of the TE fundamental mode for the 320nm-wide hybrid waveguide as function of the silica spacer and the VO_2 thickness. A black isocurve for $n_{eff} = 1.58$ is also plotted. (b) Relation between the VO_2 and the SiO_2 thicknesses to accomplish the phase matching condition in the insulating state.

This restriction makes the different effective optical parameters for the structure to be single valued at each SiO_2 thickness, as shown in Figure 119(b). So as to obtain the best performance of the device it is necessary to achieve a trade-off arising the highest change in the refractive index due to the different states of the VO_2 and the highest losses in the metallic state. Figure 120(a) shows the effective refractive index of the TE mode for the insulating and the metallic state. Increasing the silica spacer, the effect of the VO_2 over the field guided in the waveguide is gradually reduced, so the index in the metallic state tends to be equal to the index in the insulating (n=1.58). Figure 120(b) shows that the variation in the effective refractive index due to the SMT is higher when the silica spacer is thinner. Furthermore, Figure 120(c) depicts the losses in the insulating state while (d) shows the losses in the metallic state. The maximum losses in the latter are achieved for a silica thickness of 15nm. Losses in the insulating state will also increase but they will not be detrimental. Thereby, the best trade-off between the losses in the metallic state and the index variation has been obtained for a silica thickness of 10nm. In this case, the propagation losses of the hybrid waveguide when the VO_2 is in the insulating state, shown in Figure 120(c), is around 0.7dB/μm. Once the silica thickness has been optimized, the thickness of

the VO_2 is extracted from Figure 119(b). In this case, for a silica thickness of 10nm, the VO_2 thickness to achieve the phase matching condition is 20nm.

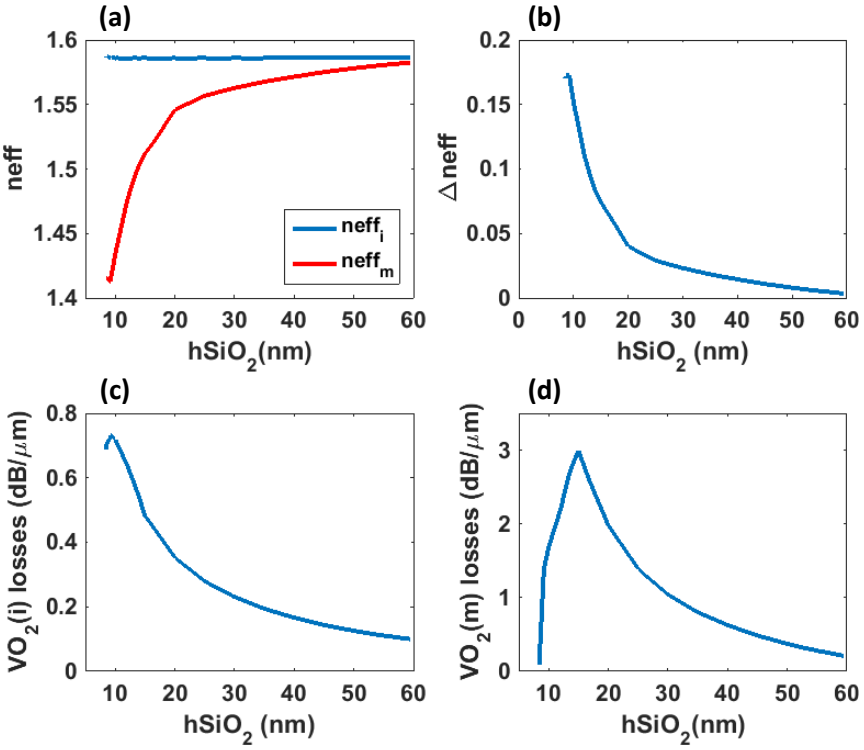

Figure 120: As function of the silica spacer; (a) effective refractive index for the TE mode for both states, (b) variation in the effective refractive index and losses in insulating (c) and metallic state.

Figure 121 shows the TM mode of the input waveguide and the TE mode of the hybrid waveguide for the optimized parameters (w_{Si}=500nm, w_H=320nm, h_{SiO2}=10nm, h_{VO2}=20nm). It can be seen that the effective refractive index of both modes is perfectly matched.

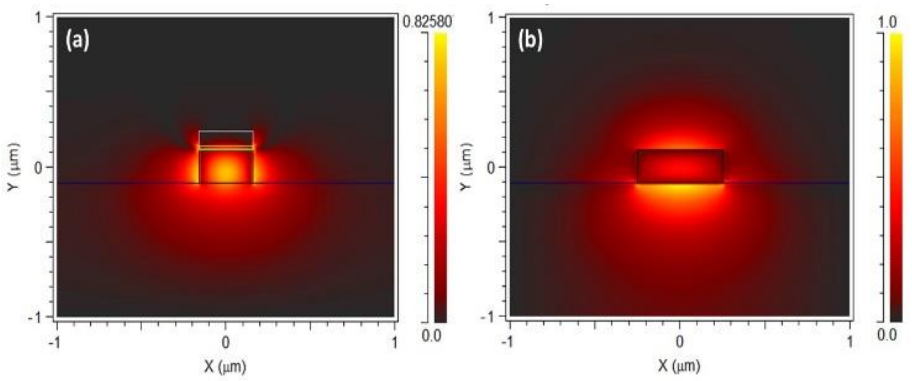

Figure 121: (a) TE mode of the hybrid waveguide and (b) TM mode of the input waveguide. Structural parameters have been optimized to obtain the same effective refractive index in both modes (n_{eff} = 1.58).

Once the structural parameters have been designed, 3D-FDTD simulations have been carried out to obtain the optimum values of distance between the waveguides and the coupling length. Figure 122 shows the insertion losses for both VO_2 states as function of the distance between the waveguides (D) and the coupling length (Lc). To achieve a large extinction ratio, high losses are desired in the metallic state while in the insulating state they should be as low as possible. The gap and the coupling length are selected according to this trade off.

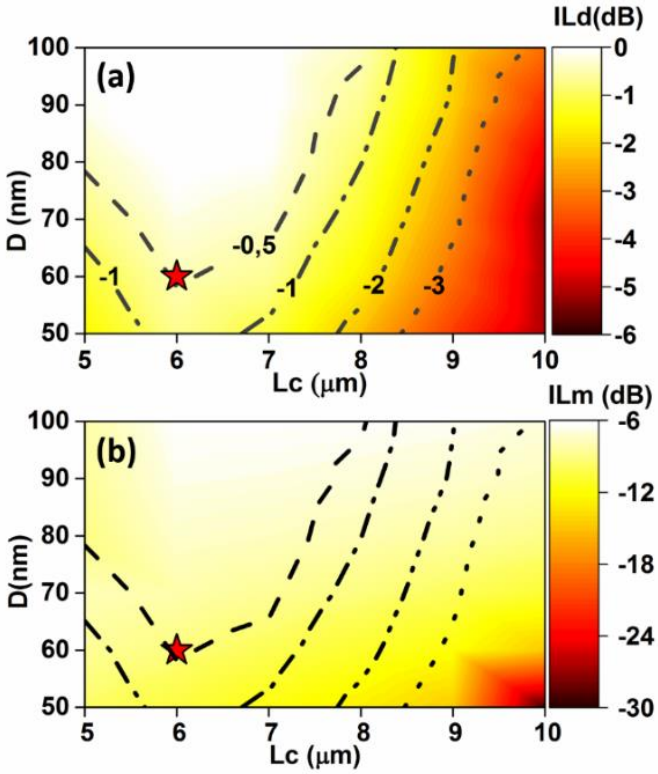

Figure 122: Insertion losses for (a) insulating and (b) metallic states as function of the distance between the waveguides, D, and the coupling length, Lc. For the insulating state, the dashed lines correspond to the losses isocurves. The x-y coordinates of those curves are also printed on the metallic state contour for better comparison.

In Figure 122(a) several losses isocurves are printed for the insulating mode and then reproduced as x-y coordinates in (b) using the same line code. In order to keep losses below 0.5dB in the insulating state while keeping the losses in the metallic state as high as possible (arising the best possible modulation extinction ratio), the distance between the waveguides must be D=60nm and the coupling length of Lc=6μm. This corresponds to insertion losses for the insulating state of 0.3dB and 11.6dB for the metallic state, leading to a modulation extinction ratio slightly above 11dB. It should be noticed that the insertion losses are lower than

the ones obtained from Figure 120(c) because the mode coupling occurs gradually along the hybrid waveguide section. Figure 123 shows the 3D-FDTD simulation of the optimized modulator at both states of VO_2.

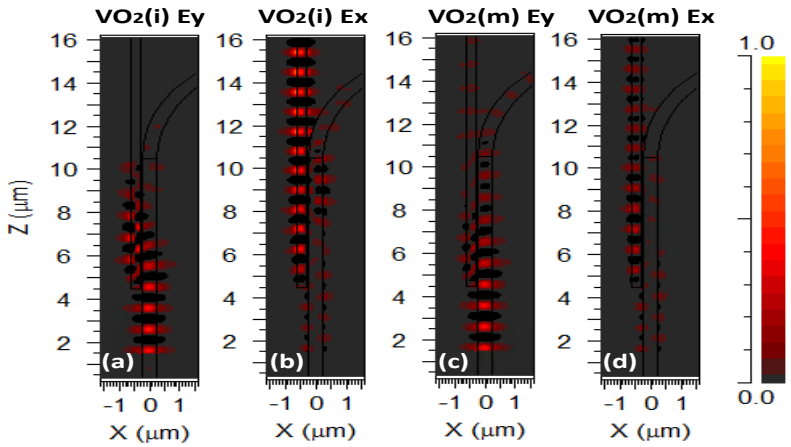

Figure 123: At steady conditions (a,b), the TM field is coupled to the hybrid waveguide and rotated to TE with high efficiency. Inducing the SMT, the VO_2 changes to the metallic state (c,d). The field is coupled but the conversion is not efficient so both TE and TM components are attenuated at the output port.

For the insulating state, the field is coupled to the hybrid waveguide and rotated into a TE mode as it is shown in Figure 123 (a) and (b). So in this case, the device acts as a rotator. Figure 124 shows the normalized output power of the optimized modulator as function of the wavelength for the rotated TE and undesired TM components when the VO_2 is in the insulating state. It is confirmed that a highly efficient TE-TM conversion is achieved at a wavelength of 1550nm with a polarization extinction ratio of 36dB and insertion losses of 0.3dB. Furthermore, a broadband wavelength performance of 60nm is also demonstrated with insertion losses below 0.5dB and polarization extinction ratios higher than 26dB.

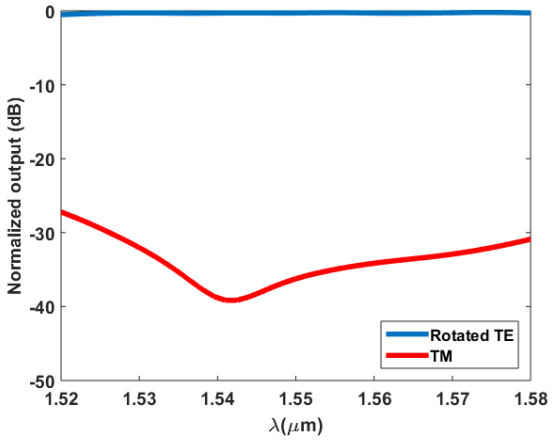

Figure 124: Normalized output power as function of wavelength for the rotated TE and undesired TM components when the VO_2 is in the insulating state.

Analogously, Figure 125 shows the normalized output power as a function of wavelength for the rotated TE component when the VO_2 is in the insulating and metallic states. For the metallic state the device is a non-efficient converter, as it was shown in Figure 123(c) and (d), due to the mismatch between the modes and the introduction of a higher value of losses. Therefore, the output power is notably attenuated yielding to a modulation extinction ratio higher than 10dB in all the wavelength range.

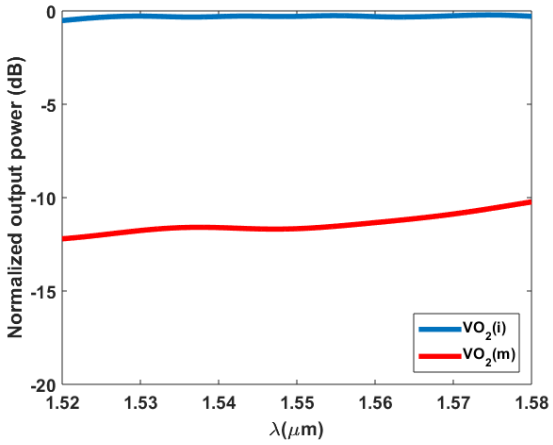

Figure 125: Normalized output power as a function of wavelength for the rotated TE component when the VO_2 is in the insulating and metallic states.

In summary, an electro-absorption VO_2/Si modulator has been proposed combining the mode coupling theory in a polarization splitting structure with the modulation capability of the vanadium dioxide. A TM input signal is converted to a modulated TE signal with polarization extinction ratios higher than 30dB, low insertion losses and broadband optical bandwidth.

4.3. Optical memory.

The hysteretic performance of VO_2 provide a path to the development of optical memories or multi-stable optical systems. Different time stable levels, of electric resistance and optical transmittance, are allowed if the VO_2 layer is maintained at a constant temperature within the range of temperatures described by its hysteretic window. Each of these states is reached by applying voltage or light pulses. The different time stable transmittance levels could allow the development of optical memories.

We propose an optical memory controlling the SMT of the VO_2 by heating. Figure 127 shows the hybrid structure Si-SiO_2-VO_2-SiO_2-Metal of the VO_2 memory.

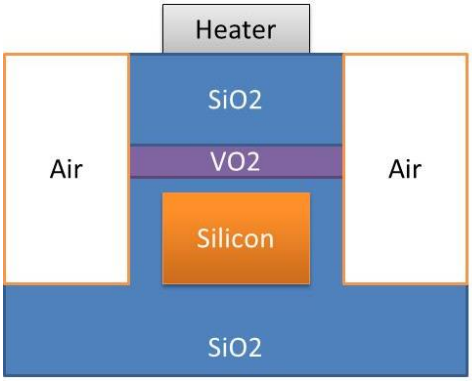

Figure 126: (a) Schematic of the proposed optical memory device based on VO_2.

The upper SiO_2 layer is enough thick to avoid the introduction of optical losses by the metal. The structure is etched to focus the heat in the VO_2 layer, avoiding its spreading into the SiO_2 surrounding. The transmittance hysteresis as function of the applied electrical power or the VO_2 temperature is shown in Figure 127. Applying the power p*, the VO_2 reaches the temperature T* and becomes stable around the point A (insulating state, ON memory state). To change to other state, point B (metallic state, OFF memory state), the power must be increased until the VO_2 reaches its metallic phase ($P > P_{I-M}$) and then decreased again to p*. Although the applied power is the same than in the beginning, due to the hysteresis, the transmittance does not come back to the point A. The system stabilizes at the point B on the "cooling down" branch of the hysteresis curve and remains in this state because the power applied maintains the VO_2 in a semi-metallic state. To come back to the original state the power is decreased to P_{M-I}, so the VO_2 comes back to its insulating phase, and then is increased to p*.

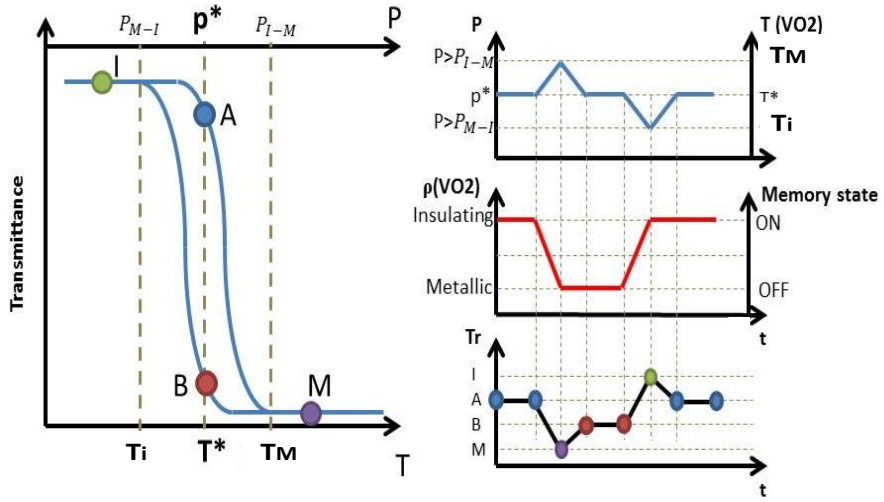

Figure 127: Transmittance as function of the VO_2 temperature and applied electrical power. The different graphs on the right side show an example of performance.

In order to quantify the required power consumption to control the VO_2 memory, several thermo-electric simulations have been carried out. Two different structures have been simulated; the structure described in Figure 128 (structure 1) and the same structure but without including the air columns (structure 2). In the structure 1, the air columns avoid the spreading of the heat in the surrounding, focusing better in the VO_2 surface and reducing the required power consumption to complete the SMT. For a temperature increment of 50C the required power are 0.78mW and 1.16mW in structure 1 and 2 respectively. Therefore, the structure 1 reduces the power consumption around a 35%.

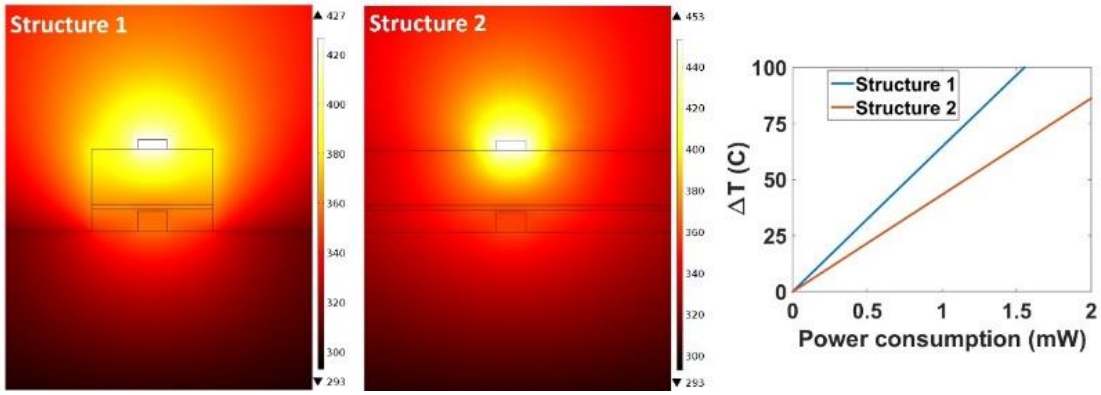

Figure 128: Transversal temperature distribution and $\Delta T(C)$ as function of Power consumption for both structures. Delimiting the structure by air columns, the heat is better canalized to the VO_2 surface instead of spreading to the surrounding media. In this way, the required power consumption to complete the MIT is reduced around a 35%.

4.4. Smart waveguide-based bionanosensor.

Silicon-based sensors have emerged as a promising candidate for the integration of point-of-care lab-on-chip systems able to provide the sensing abilities of current bulky and expensive devices employed by the biomedical industry. Efforts carried out so far have yielded several kinds of structures, most of them based on the use of silicon ring resonators with footprints ranging from tens of micrometers up to the millimeter scale. These approaches have proved to be a reasonable good performance in the interaction with biomolecules such as proteins and bacteria. Nevertheless, these attempts in the integrated sensing field show some drawbacks that have not yet been overcome; namely, a further improvement in the detection limit in complex media, expensive costs due to the necessity of typical use of external cavity lasers (ECL) or its integration with microfluidics technology. Aimed to provide a more compact an efficient solution, here we propose a novel approach based on the use of a single silicon waveguide, integrated with a VO_2 stretch that can be thermally controlled by a heatable tip, see Figure 129.

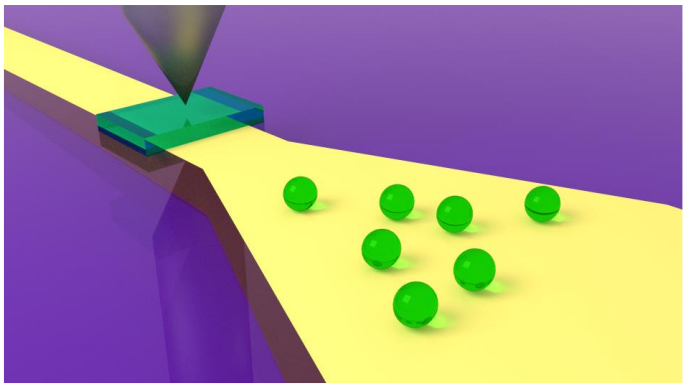

Figure 129: Concept art of the smart waveguide-based bionanosensor. The SMT of the VO_2 stretch, thermally controlled by the heatable tip, provides the dynamically control of the effective refractive index of the waveguide allowing to quantify the optical interaction of a molecule/particle with several propagated modes. This sensor offers a deep analysis in a lab-on-chip system.

Via temperature changes induced by the heatable tips it is possible to dynamically change the effective refractive index within the waveguide by controlling the SMT of the vanadium dioxide. It enables to quantify the optical interaction of the same molecule/particle with several propagated modes, offering by this way a richer and deeper analysis of the biostructure with the same lab-on-chip system. It has to be pointed out that the possibilities of this configuration are even greater: the use of several VO_2 stretches would display the chance of building up tailor-made index profiles so as to classify biotargets in a finer analysis. Once the refractive index is changed, it persists in the waveguide allowing us to induce this change by heatable tips distant from the sensing plate where the targets are tested. Besides, the compatible CMOS silicon waveguides here employed, assure a readily integration with current standard photonic procedures as well as paves the way to the implementation with future on-chip integrated semiconductor lasers.

4.5. Reconfigurable metamaterial for smart material-based surfaces.

Metamaterials are periodic structures which provide superficial and structural light guiding control by means of the introduction of changes in the refractive index of the material in small areas. Usual metamaterial approaches are based on static performances, meaning that the inclusion or modification of these small areas displays a fix topology able to fulfil only one determined function. As instance, imaging a bulky piece of silicon with small cylindrical areas compounded by other materials. This configuration would be great for providing a desired gradient index in order to conduct light with a specific pathway. But this pathway is not easily externally reconfigurable. To achieve the dynamic configurability of this network, one possible approach is the introduction of 'smart' materials. It is straightforward to consider again VO_2 as a perfect candidate to provide changes

in its refractive index, making possible the implementation of dynamic reconfigurable metamaterials. However, in order to control the light propagation, it is crucial to control the temperature of very small areas (like pixels) of the VO_2 surface and this is not possible with conventional heaters. A 2D matrix of nanoscale heatable tips can overcome this limitation, see Figure 130. Controlling the temperature of each tip renders the possibility to change the refractive index of the VO_2, assuring that the heat is fully concentrated on the pixel, paving the way for intelligent and reconfigurable metamaterial networks, a feature which could increase the versatility and flexibility of photonic integrated circuitry.

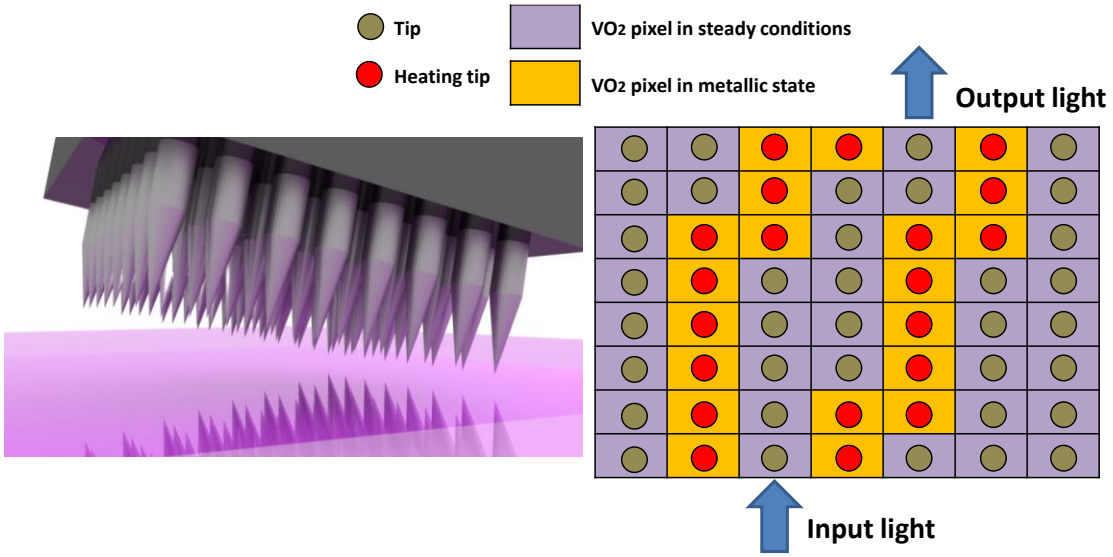

Figure 130: With the matrix of tips, a pixel control of the index in the VO_2 surface allows to make reconfigurable light guiding and processing by introducing changes in the refractive index of small areas. It opens a new path for high efficiency reconfigurable photonic devices.

Chapter 5

Conclusions and future work

5.1. Conclusions.

In this thesis, several topics like the polarization management, the optical switching and optical modulation have been investigated. The state of the art of these topics in silicon photonics have been analyzed and in some cases new devices have been proposed combining with another technologies like, for example, plasmonics. Furthermore, the integration of new materials in the silicon platform, like the vanadium dioxide, with disruptive optical and electrical properties has also been addressed. Optically, vanadium dioxide is a lossy material but combined with photonics is able to provide ultra-small devices with low power consumption and high performance.

The first topic studied in this thesis has been the polarization management in silicon photonics. Optical devices based on silicon have a polarization dependent performance. Therefore, it is crucial to feed them with their right polarization. We have proposed a polarization splitting and rotation device combining photonics with plasmonics able to split the different polarizations of light and convert the TM component into a TE one. For a broadband performance over a range of 60nm, the TE input polarization is directly guided to an output port with insertion losses below 1dB while the TM input polarization is splitted to another output port and rotated with insertion losses below 3dB and crosstalk higher than 35dB. We have also proposed a TM to TE converter based in the combination of photonics with plasmonics. The proposed device, with a total length of 8μm improves the extinction ratio above 20dB, while maintaining the insertion losses below 1.5dB, at the standard telecom wavelength of 1550nm. At the time of the publication, this device had one of the best ratios between the

extinction ratio and the insertion losses as it was reported in [95]. Our last contribution to the polarization management topic is the design of polarizers based on the hybrid technology VO_2/Si. Polarizers are key elements for polarization control and usually they work rejecting the non-desired polarization. Introducing the VO_2 to a polarizer structure allows to make them externally controlled by the SMT while maintaining the compatibility with CMOS fabrication techniques. This control allows to eliminate the unwanted polarization as function of an external signal. To the best of our knowledge, this is the first time that tunable polarizers compatible with silicon photonics have been proposed. Our tunable TE and TM pass polarizers exhibit an ultra-compact footprint with a total length of only 1µm, insertion losses below 3dB and broadband operation. Furthermore, they can be integrated in a compact structure to achieve a full control of the polarization of the input signal. In this case, the unwanted polarization would be attenuated above 17dB while the desired polarization would have losses below 5dB.

The next topic investigated in this thesis has been the optical switching. Optical switches with high performance and low power consumption are key building blocks to the development of optical networks. First, we have focused on the development of a novel approach to decrease the power consumption in silicon switches. More specifically, this method has been demonstrated experimentally in a switch based on an asymmetric MZI structure being operated with a conveniently chosen wavelength. A power consumption reduction up to 50% has been demonstrated which could open a new path for energy efficient switching in silicon via the thermo-optic effect. On the other hand, the introduction of vanadium dioxide in optical switching structures allows to take profit of the disruptive properties of this material, enhancing the performance of the devices. We have designed and optimized a 2x2 microring switch based on a hybrid VO_2/silicon waveguide structure. Active performance is based on the VO_2 SMT exploiting the change in absorption loss and also taking advantage of the induced phase shift to enhance the performance. Thus, insertion losses below 1.8 dB and crosstalk values above 12 dB have been achieved for TE operation in a compact switching device with an active length as low as 2.8µm and a footprint below 100µm^2. The data throughput rate at a single optical wavelength could be higher than 500Gbps thus proving VO_2/Si technology as a promising approach for the development of switches with high throughput bandwidth, low power consumption, small footprint and compatibility with silicon CMOS photonics.

After the design of the switch, the vanadium dioxide has been optically and electrically characterized. Ellipsometry measurements of films with different thicknesses under different temperatures have been carried out to measure the

refractive index. Then, different topologies of electrodes deposited over the VO_2 films have been characterized. We have proposed a short-circuited electrode topology which reduces the power consumption in comparison with conventional electrodes used in VO_2 junctions. Finally, we have experimentally demonstrated the switching capability of the designed 2x2 microring switch. A significant change of optical absorption has been achieved using a 2µm long hybrid VO_2/silicon waveguide integrated in the ring resonator structure.

Finally, we have focused on the design of different electro-absorption modulators based on the SMT of the vanadium dioxide. The simplest topology based on a VO_2 film over a silicon waveguide has been studied for both input polarizations. TE modulators have a lower interaction with the active material so they need to be longer than the TM modulators to achieve a good extinction ratio with the same insertion losses. Therefore, TM modulators show higher extinction ratios with a more compact footprint but they need additional coupling structures to excite the desired mode during the metallic state. In order to achieve a TM modulator with the output to TE polarization, a novel electro-absorption VO_2/Si modulator with polarization rotation has been proposed. Its performance is based on the combination of the mode coupling theory with the modulation capability obtained by means of the semiconductor to metal transition of the vanadium dioxide. The device is fed by a TM input signal which is converted to TE polarization and modulated changing the VO_2 state with a polarization extinction ratio higher than 30dB, very low insertion losses and a broadband optical bandwidth operation.

In summary, it can be stated that vanadium dioxide combined with photonics and plasmonics is a promising approach for developing novel devices for different applications with beyond the state of the art performance.

5.2. Future work.

One of the main goals in the SITOGA project is the integration of vanadium dioxide on silicon to demonstrate a beyond state of the art electro-optical switching component with fast switching times, low power consumption, ultra-small footprint and very low insertion losses. Once this photonic device has been demonstrated, the next step is to develop a functional demonstrator based on an 8x8 switching matrix with 100Gbit/s throughput and a total footprint below 3500µm^2. This demonstrator will validate the developed integration process of the vanadium dioxide with silicon photonics and drive the exploitation of the developed technology by the industrial partners.

Figure 131 shows different SEM images of a (a) 4x4 matrix composed by 4 rings and (b) 8x8 matrix composed by 16 rings. Both devices have also been designed and recently fabricated. The proposed on chip photonic non-blocking switching matrixes rely on the Benes architecture.

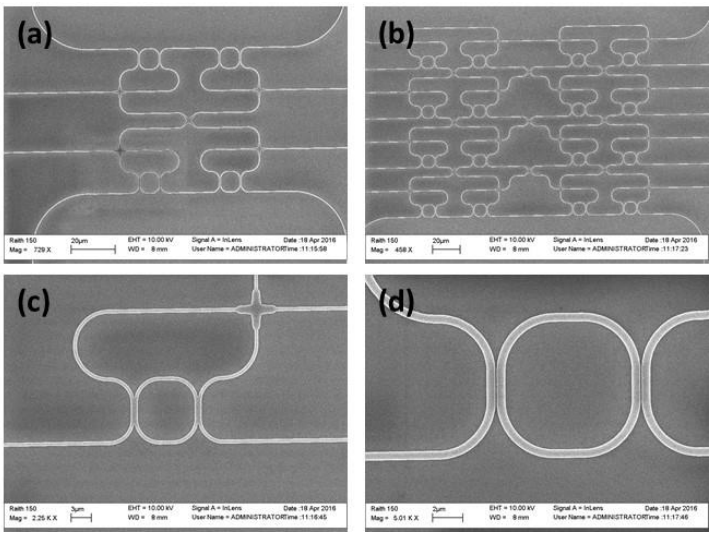

Figure 131: SEM images of (a) a 4x4 matrix composed by 4 rings, (b) an 8x8 matrix composed by 16 rings, (c) a view of a ring with a cross junction and (d) a view of the gap between the input/output waveguides and a ring.

An interconnection network is classified as nonblocking if any input can be connected to any unused output. The Benes architecture employs the fewest number of switching elements to build an NxN switch and provides the lowest insertion losses in comparison with other architectures [97]. The switching matrices employ as basic building block the 2x2 add-drop ring resonators developed in this thesis. Therefore, controlling the different rings via the semiconductor to metal transition of the vanadium dioxide will allow the full routing across the switching matrix providing a key component for optical networks with great performance.

In fact, the main future work is the characterization of these matrices and the demonstration of the functional demonstrator aimed at SITOGA. On the other hand, based on the developed work in the thesis, other research lines beyond the project SITOGA are:

- Characterize and optimize the switching time. It will be very interesting to analyze if the proposed short-circuited electrode has or has not a slower time response.
- Investigate different approaches to decrease the power consumption that can be achieved with the short-circuited electrode, for instance, by

decreasing the distance to the silicon waveguide or by simulating and optimizing the heat transfer process.

- Optimize the material to reduce the imaginary part of its refractive index in the insulating state for minimizing the optical losses and also to decrease the transition temperature to improve the efficiency of the SMT transition and therefore the power consumption.

List of publications

Journal publications

- **Sánchez, L.**, and Sanchis, P. (2013). Broadband 8 micrometers long hybrid silicon-plasmonic transverse magnetic-transverse electric converter with losses below 2 dB. Optics Letters, 38(15), 2842-2845.
- **Sánchez, L.**, Griol, A., Lechago, S., Brimont, A., and Sanchis, P. (2015). Low-Power Operation in a Silicon Switch Based on an Asymmetric Mach–Zehnder Interferometer. IEEE Photonics Journal, 7(2), 1-8.
- **Sánchez, L.**, Lechago, S., and Sanchis, P. (2015). Ultra-compact TE and TM pass polarizers based on vanadium dioxide on silicon. Optics letters, 40(7), 1452-1455.
- **Sánchez, L.**, Lechago, S., Gutierrez, A., and Sanchis, P. (2016). Analysis and Design Optimization of a Hybrid VO_2/Silicon 2x2 Microring Switch. IEEE Photonics Journal, 8(2), 1-9.
- **Sánchez, L.**, Cortes, F.J., Rosa, A., and Sanchis, P. (2016). Design of an ultra-compact electro-absorption VO_2-Si modulator with TM to TE conversion. Submitted.

Conference publications

- **Sánchez, L.**, Mas, S., and Sanchis, P. (2013). Ultra-compact hybrid silicon plasmonic polarization diversity circuit. In 10th International Conference on Group IV Photonics.
- Royo, F. L., Brimont, A., Vagionas, C., Dabos, G., Pleros, N., Vyrsokinos, K., **Sánchez, L.**, ... and Sanchis, P. (2014, March). Fabrication of modulators and 2× 2 switches in SOI based on the carrier depletion mechanism for optical interconnects. In SPIE OPTO (pp. 899112-899112). International Society for Optics and Photonics.
- **Sánchez, L.**, Brimont, A., Lechago, S., Griol, A., and Sanchis, P. (2014, May). A silicon Mach Zehnder comb switch for low power operation in on-chip optical data communications. In SPIE Photonics Europe (pp. 91330P-91330P). International Society for Optics and Photonics.
- Sanchis, P., **Sánchez, L.**, Castera, P., Rosa, A., Gutierrez, A. M., Brimont, A., ... and Bachelet, R. (2014, July). Silicon CMOS compatible transition metal dioxide technology for boosting highly integrated photonic devices with disruptive performance. In 2014 16th International Conference on Transparent Optical Networks (ICTON) (pp. 1-4). IEEE.
- Brimont, A., Vagionas, C., Pleros, N., Vyrsokinos, C., Griol, A., Sanchis, P., **Sánchez, L.,** ... and Losilla, N. S. (2014, August). Compact and

efficient silicon 2× 2 switches based on a reverse biased vertical pn junction. In 11th International Conference on Group IV Photonics (GFP).

- **Sánchez, L.**, Griol, A., Brimont, A., and Sanchis, P. (2014, August). A novel technique for minimizing power consumption in MZI based silicon switches. In 11th International Conference on Group IV Photonics (GFP).
- Sanchis, P., **Sánchez, L.**, Griol, A., Hurtado, J., Menghini, M., Homm, P., ... and Locquet, J. P. (2015, July). Ultra-low power hybrid VO_2/Si photonic microring switch. In 2015 17th International Conference on Transparent Optical Networks (ICTON) (pp. 1-4). IEEE.
- **Sánchez, L.**, Gutierrez, A. M., Brimont, A., and Sanchis, P. (2015, August). Design of an ultra-compact hybrid VO_2/silicon switch. In 2015 IEEE 12th International Conference on Group IV Photonics (GFP) (pp. 100-101). IEEE.
- **Sánchez, L.**, Rosa, A., Angelova, T., Hurtado, J., Griol, A., Sanchis, P., Menghini M., Homm P., Bilzen B., Locquet J.P. and and Zimmermann, L. Electrical Switching in Hybrid VO_2/Si Photonic Structures. In 2016 18th International Conference on Transparent Optical Networks (ICTON) (pp. 1-4). IEEE.

Other publications

- Deliverable D4.1: Developed VO_2/Si based waveguiding structures. Authors: **Luis David Sánchez**, Juan Hurtado, Amadeu Griol, Pablo Sanchis, Mariela Menghini and Jean-Pierre Locquet.
- Deliverable D4.2: Characterization of the electro-optical switching VO_2/Si performance on the chosen waveguide structure. Authors: **Luis David Sánchez**, Mariela Menghini, Stefan Abel, Juan Hurtado, Amadeu Griol, Jean-Pierre Locquet and Pablo Sanchis.
- Deliverable D4.3: Progress on development of novel electro-optical functionalities based on VO_2/Si. Authors: **Luis David Sánchez**, Alvaro Rosa, Amadeu Griol, Pablo Sanchis, Mariela Menghini and Jean-Pierre Locquet.
- Deliverable D4.4: Progress on the fabrication of the VO_2/Si switching component. Authors: Mariela Menghini, Jean-Pierre Locquet, **Luis David Sánchez**, Juan Hurtado, Amadeu Griol, Pablo Sanchis and Marilyne Sousa.
- Deliverable D4.5 VO_2/Si switching component compliant to specifications. Authors: Pablo Sanchis, **Luis David Sánchez**, Alvaro Rosa Escutia, Juan Hurtado, Amadeu Griol, Mariela Menghini, Pia Homm, Bart van Bilzen and Jean-Pierre Locquet.

Bibliography

[1] Soref, R. (2006). The past, present, and future of silicon photonics. IEEE Journal of selected topics in quantum electronics, 12(6), 1678-1687.
[2] Jalali, B., and Fathpour, S. (2006). Silicon photonics. Journal of lightwave technology, 24(12), 4600-4615.
[3] Arakawa, Y., Nakamura, T., Urino, Y., and Fujita, T. (2013). Silicon photonics for next generation system integration platform. IEEE Communications Magazine, 51(3), 72-77.
[4] Soref, R. (2010). Silicon photonics: a review of recent literature. Silicon, 2(1), 1-6.
[5] Bogaerts, W., Fiers, M., and Dumon, P. (2014). Design challenges in silicon photonics. IEEE Journal of Selected Topics in Quantum Electronics, 20(4), 1-8.
[6] Dionne, J. A., Sweatlock, L. A., Sheldon, M. T., Alivisatos, A. P., and Atwater, H. A. (2010). Silicon-based plasmonics for on-chip photonics. IEEE Journal of Selected Topics in Quantum Electronics,16(1), 295-306.
[7] Kinsey, N., Ferrera, M., Shalaev, V. M., and Boltasseva, A. (2015). Examining nanophotonics for integrated hybrid systems: a review of plasmonic interconnects and modulators using traditional and alternative materials. JOSA B, 32(1), 121-142.
[8] Gan, X., Shiue, R. J., Gao, Y., Meric, I., Heinz, T. F., Shepard, K., ... and Englund, D. (2013). Chip-integrated ultrafast graphene photodetector with high responsivity. Nature Photonics, 7(11), 883-887.
[9] Kim, J. T., Chung, K. H., and Choi, C. G. (2013). Thermo-optic mode extinction modulator based on graphene plasmonic waveguide. Optics express,21(13), 15280-15286.
[10] Shin, J. S., and Kim, J. T. (2015). Broadband silicon optical modulator using a graphene-integrated hybrid plasmonic waveguide. Nanotechnology, 26(36), 365201.
[11] Liu, M., Yin, X., Ulin-Avila, E., Geng, B., Zentgraf, T., Ju, L., ... and Zhang, X. (2011). A graphene-based broadband optical modulator. Nature, 474(7349), 64-67.
[12] Ye, C., Khan, S., Li, Z. R., Simsek, E., and Sorger, V. J. (2014). λ-size ITO and graphene-based electro-optic modulators on SOI. IEEE Journal of Selected Topics in Quantum Electronics, 20(4), 40-49.

[13] Bozhevolnyi, S. I. (2008). “Plasmonic nano-guides and circuits. In Plasmonics and Metamaterial”. Optical Society of America.
[14] Maier, S. A. (2007). “Plasmonics: fundamentals and applications”. Springer Science and Business Media.
[15] Tobing, L. Y., Tjahjana, L., and Zhang, D. H. (2012). Demonstration of low-loss on-chip integrated plasmonic waveguide based on simple fabrication steps on silicon-on-insulator platform. Applied Physics Letters, 101(4), 041117.
[16] Zhu, S., Lo, G. Q., and Kwong, D. L. (2012). Performance of ultracompact copper-capped silicon hybrid plasmonic waveguide-ring resonators at telecom wavelengths. Optics express, 20(14), 15232-15246.
[17] Cai, W., White, J. S., and Brongersma, M. L. (2009). Compact, high-speed and power-efficient electrooptic plasmonic modulators. Nano letters, 9(12), 4403-4411.
[18] Dionne, J. A., Diest, K., Sweatlock, L. A., and Atwater, H. A. (2009). PlasMOStor: a metal− oxide− Si field effect plasmonic modulator. Nano Letters, 9(2), 897-902.
[19] Thomas, R., Ikonic, Z., and Kelsall, R. W. (2012). Electro-optic metal–insulator–semiconductor–insulator–metal Mach-Zehnder plasmonic modulator. Photonics and Nanostructures-Fundamentals and Applications, 10(1), 183-189.
[20] Zhu, S., Lo, G. Q., and Kwong, D. L. (2013). Phase modulation in horizontal metal-insulator-silicon-insulator-metal plasmonic waveguides. Optics express, 21(7), 8320-8330.
[21] Pleros, N., Kriezis, E. E., and Vyrsokinos, K. (2011). Optical interconnects using plasmonics and Si-photonics. IEEE Photonics Journal, 3(2), 296-301.
[22] Fedyanin, D. Y., Krasavin, A. V., Arsenin, A. V., and Zayats, A. V. (2012). Surface plasmon polariton amplification upon electrical injection in highly integrated plasmonic circuits. Nano letters, 12(5), 2459-2463.
[23] Reed, G. T., and Knights, A. P. (2004). “Silicon photonics: an introduction”. John Wiley and Sons.
[24] Sun, X., Mojahedi, M., and Aitchison, J. S. (2016). Hybrid plasmonic waveguide-based ultra-low insertion loss transverse electric-pass polarizer. Optics Letters, 41(17), 4020-4023.
[25] Barwicz, T., Watts, M. R., Popović, M. A., Rakich, P. T., Socci, L., Kärtner, F. X., ... and Smith, H. I. (2007). Polarization-transparent microphotonic devices in the strong confinement limit. Nature Photonics, 1(1), 57-60.
[26] Komatsu, M. A., Saitoh, K., and Koshiba, M. (2012). Compact polarization rotator based on surface plasmon polariton with low insertion loss. Photonics Journal, IEEE, 4(3), 707-714.
[27] Zhang, J., Liow, T. Y., Yu, M., Lo, G. Q., and Kwong, D. L. (2010). Silicon waveguide based TE mode converter. Optics express, 18(24), 25264-25270.

[28] Zhang, J., Yu, M., Lo, G., and Kwong, D. L. (2010). Silicon waveguide-based mode-evolution polarization rotator. In SPIE Photonics Europe. International Society for Optics and Photonics.
[29] Kim, S., and Qi, M. (2015). Mode-evolution-based polarization rotation and coupling between silicon and hybrid plasmonic waveguides. Scientific reports, 5, 18378.
[30] Xie, A., Zhou, L., Chen, J., and Li, X. (2015). Efficient silicon polarization rotator based on mode-hybridization in a double-stair waveguide. Optics express, 23(4), 3960-3970.
[31] Hsu, C. W., Lin, H. Y., Chen, J. Y., and Cheng, Y. C. (2016). Ultracompact polarization rotator in an asymmetric single dielectric loaded rib waveguide. Applied optics, 55(6), 1395-1400.
[32] Fukuda, H., Yamada, K., Tsuchizawa, T., Watanabe, T., Shinojima, H., and Itabashi, S. I. (2006). Ultrasmall polarization splitter based on silicon wire waveguides. Optics Express, 14(25), 12401-12408.
[33] Fukuda, H., Yamada, K., Tsuchizawa, T., Watanabe, T., Shinojima, H., and Itabashi, S. I. (2008). Silicon photonic circuit with polarization diversity. Optics express, 16(7), 4872-4880.
[34] Yue, Y., Zhang, L., Yang, J. Y., Beausoleil, R. G., and Willner, A. E. (2010). Silicon-on-insulator polarization splitter using two horizontally slotted waveguides.Optics letters, 35(9), 1364-1366.
[35] Zhang, H., Huang, Y., Das, S., Li, C., Yu, M., Lo, P. G. Q., ... and Thong, J. (2013). Polarization splitter using horizontal slot waveguide. Optics express,21(3), 3363-3369.
[36] Guan, H., Novack, A., Streshinsky, M., Shi, R., Fang, Q., Lim, A. E. J., ... and Hochberg, M. (2014). CMOS-compatible highly efficient polarization splitter and rotator based on a double-etched directional coupler. Optics express, 22(3), 2489-2496.
[37] Zhang, J., Zhu, S., Zhang, H., Chen, S., Lo, G. Q., and Kwong, D. L. (2011). An ultracompact surface plasmon polariton-effect-based polarization rotator.Photonics Technology Letters, IEEE, 23(21), 1606-1608.
[38] Caspers, J. N., Alam, M. Z., and Mojahedi, M. (2012). Compact hybrid plasmonic polarization rotator. Optics letters, 37(22), 4615-4617.
[39] Caspers, J. N., Aitchison, J. S., and Mojahedi, M. (2013). Experimental demonstration of an integrated hybrid plasmonic polarization rotator. Optics letters,38(20), 4054-4057.
[40] Kiyat, I., Aydinli, A., and Dagli, N. (2005). A compact silicon-on-insulator polarization splitter. Photonics Technology Letters, IEEE, 17(1), 100-102.

[41] Xu, Y., Xiao, J., and Sun, X. (2014). A compact hybrid plasmonic polarization rotator for silicon-based slot waveguides. Photonics Technology Letters, IEEE,26(16), 1609-1612.
[42] Chee, J., Zhu, S., and Lo, G. Q. (2012). CMOS compatible polarization splitter using hybrid plasmonic waveguide. Optics express, 20(23), 25345-25355.
[43] Huang, Y., Zhu, S., Zhang, H., Liow, T. Y., and Lo, G. Q. (2013). CMOS compatible horizontal nanoplasmonic slot waveguides TE-pass polarizer on silicon-on-insulator platform. Optics express, 21(10), 12790-12796.
[44] Mahros, A. M., Tharwat, M. M., and Ashry, I. (2015). Investigating the characteristics of TM-pass/TE-stop polarizer designed using plasmonic nanostructures.Applied optics, 54(14), 4464-4470.
[45] Sun, X., Mojahedi, M., & Aitchison, J. S. (2016). Hybrid plasmonic waveguide-based ultra-low insertion loss transverse electric-pass polarizer.Optics Letters, 41(17), 4020-4023.
[46] Sánchez, L., Mas, S., and Sanchis, P. (2013). Ultra-compact hybrid silicon plasmonic polarization diversity circuit. In 10th International Conference on Group IV Photonics.
[47] Sun, X., Alam, M. Z., Wagner, S. J., Aitchison, J. S., and Mojahedi, M. (2012). Experimental demonstration of a hybrid plasmonic transverse electric pass polarizer for a silicon-on-insulator platform. Optics letters, 37(23), 4814-4816.
[48] Sánchez, L., and Sanchis Kilders, P. (2013). Broadband 8 micrometers long hybrid silicon-plasmonic transverse magnetic-transverse electric converter with losses below 2dB. Optics Letters, 38(15), 2842-2845.
[49] Briggs, R. M., Pryce, I. M., and Atwater, H. A. (2010). Compact silicon photonic waveguide modulator based on the vanadium dioxide metal-insulator phase transition. Optics express, 18(11), 11192-11201.
[50] Sánchez, L., Lechago, S., and Sanchis, P. (2015). Ultra-compact TE and TM pass polarizers based on vanadium dioxide on silicon. Optics letters, 40(7), 1452-1455.
[51] Taubenblatt, M. (2011, March). Optical interconnects for high performance computing. In Optical Fiber Communication Conference (p. OThH3). Optical Society of America.
[52] Bergman K. (2006). Photonic networks for intra-chip, inter-chip, and box-to-box interconnects in high performance computing. Proc. Opt. Commun. ECOC Eur. Conf.
[53] Lin, B. C., and Lea, C. T. (2013). Exploiting two-wavelength switching capability of silicon photonic microrings. Lightwave Technology, Journal of, 31(6), 975-981.

[54] Baba, T., Akiyama, S., Imai, M., Hirayama, N., Takahashi, H., Noguchi, Y., ... and Usuki, T. (2013). 50-Gb/s ring-resonator-based silicon modulator.Optics express, 21(10), 11869-11876.
[55] Yang, M., Green, W. M., Assefa, S., Van Campenhout, J., Lee, B. G., Jahnes, C. V., ... and Vlasov, Y. A. (2011). Non-blocking 4x4 electro-optic silicon switch for on-chip photonic networks. Optics express, 19(1), 47-54.
[56] Xu, H., Xiao, X., Li, X., Hu, Y., Li, Z., Chu, T., ... and Yu, J. (2012). High speed silicon Mach-Zehnder modulator based on interleaved PN junctions. Optics express, 20(14), 15093-15099.
[57] Chen, W., Wang, W., Guo, W., Gong, Z., Zhou, H., Zhou, Q., ... and Yang, J. (2012). A 2× 2 nonblocking Mach–Zehnder-based silicon switch matrix. Optics express, 20(11), 12593-12598.
[58] Li, X., Xiao, X., Xu, H., Li, Z., Chu, T., Yu, J., and Yu, Y. (2013). Mach–Zehnder-based five-port silicon router for optical interconnects. Optics letters,38(10), 1703-1705.
[59] Chen, W., Wang, W., Gong, Z., Zhou, Q., Jiang, X., Yang, J., and Zhou, H. (2012). Mach–Zehnder-based four-port switching module on SOI. Photonics Technology Letters, IEEE, 24(15), 1313-1315.
[60] Ryckman, J. D., Diez-Blanco, V., Nag, J., Marvel, R. E., Choi, B. K., Haglund, R. F., and Weiss, S. M. (2012). Photothermal optical modulation of ultra-compact hybrid Si-VO_2 ring resonators. Optics express, 20(12), 13215-13225.
[61] Ryckman, J. D., Hallman, K. A., Marvel, R. E., Haglund, R. F., and Weiss, S. M. (2013). Ultra-compact silicon photonic devices reconfigured by an optically induced semiconductor-to-metal transition. Optics express, 21(9), 10753-10763.
[62] Markov, P., Ryckman, J. D., Marvel, R. E., Hallman, K. A., Haglund, R. F., and Weiss, S. M. (2013). Silicon-VO_2 hybrid electro-optic modulator. In CLEO: Science and Innovations. Optical Society of America.
[63] Joushaghani, A., Jeong, J., Paradis, S., Alain, D., Aitchison, J. S., and Poon, J. K. (2015). Wavelength-size hybrid Si-VO_2 waveguide electroabsorption optical switches and photodetectors. Optics express, 23(3), 3657-3668.
[64] Sweatlock, L. A., and Diest, K. (2012). Vanadium dioxide based plasmonic modulators. Optics express, 20(8), 8700-8709.
[65] Ooi, K. J., Bai, P., Chu, H. S., and Ang, L. K. (2013). Ultracompact vanadium dioxide dual-mode plasmonic waveguide electroabsorption modulator. Nanophotonics, 2(1), 13-19.
[66] Joushaghani, A., Kruger, B. A., Paradis, S., Alain, D., Aitchison, J. S., and Poon, J. K. (2013). Sub-volt broadband hybrid plasmonic-vanadium dioxide switches. Applied Physics Letters, 102(6), 061101.

[67] Kim, J. T. (2014). CMOS-compatible hybrid plasmonic modulator based on vanadium dioxide insulator-metal phase transition. Optics letters,39(13), 3997-4000.

[68] Choe, J. H., and Kim, J. T. (2015). Design of Vanadium Dioxide-Based Plasmonic Modulator for Both TE and TM Modes. Photonics Technology Letters, IEEE, 27(5), 514-517.

[69] Dong, P., Preble, S. F., and Lipson, M. (2007). All-optical compact silicon comb switch. Optics express, 15(15), 9600-9605.

[70] Sanchez, L., Griol, A., Lechago, S., Brimont, A., and Sanchis, P. (2015). Low-Power Operation in a Silicon Switch Based on an Asymmetric Mach–Zehnder Interferometer. IEEE Photonics Journal, 7(2), 1-8.

[71] Sánchez, L., Brimont, A., Lechago, S., Griol, A., and Sanchis, P. (2014, May). A silicon Mach Zehnder comb switch for low power operation in on-chip optical data communications. In SPIE Photonics Europe (pp. 91330P-91330P). International Society for Optics and Photonics.

[72] Sánchez, L., Griol, A., Brimont, A., and Sanchis, P. (2014, August). A novel technique for minimizing power consumption in MZI based silicon switches. In 11th International Conference on Group IV Photonics (GFP).

[73] Bogaerts, W., De Heyn, P., Van Vaerenbergh, T., De Vos, K., Kumar Selvaraja, S., Claes, T., and Baets, R. (2012). "Silicon microring resonators", Laser and Photonics Reviews, 6(1), 47-73.

[74] Ruzmetov, D., Gopalakrishnan, G., Deng, J., Narayanamurti, V., and Ramanathan, S. (2009). Electrical triggering of metal-insulator transition in nanoscale vanadium oxide junctions. Journal of Applied Physics, 106(8), 083702.

[75] Stefanovich, G., Pergament, A., and Stefanovich, D. (2000). Electrical switching and Mott transition in VO_2. Journal of Physics: Condensed Matter, 12(41), 8837.

[76] Gopalakrishnan, G., Ruzmetov, D., and Ramanathan, S. (2009). On the triggering mechanism for the metal–insulator transition in thin film VO_2 devices: electric field versus thermal effects. Journal of materials science, 44(19), 5345-5353.

[77] Joushaghani, A., Jeong, J., Paradis, S., Alain, D., Aitchison, J. S., and Poon, J. K. (2014). Voltage-controlled switching and thermal effects in VO_2 nano-gap junctions. Applied Physics Letters,104(22), 221904.

[78] Markov, P., Marvel, R. E., Conley, H. J., Miller, K. J., Haglund Jr, R. F., and Weiss, S. M. (2015). Optically monitored electrical switching in VO_2. ACS Photonics, 2(8), 1175-1182.

[79] Zimmers, A., Aigouy, L., Mortier, M., Sharoni, A., Wang, S., West, K. G., ... and Schuller, I. K. (2013). Role of Thermal Heating on the Voltage Induced Insulator-Metal Transition in VO_2. Physical review letters, 110(5), 056601.

[80] Joushaghani, A., Jeong, J., Paradis, S., Alain, D., Aitchison, J. S., and Poon, J. K. (2015, August). Characteristics of the Current-Controlled Phase Transition of VO_2 Microwires for Hybrid Optoelectronic Devices. In Photonics (Vol. 2, No. 3, pp. 916-932). Multidisciplinary Digital Publishing Institute.

[81] Joushaghani, A., Jeong, J., Paradis, S., Alain, D., Aitchison, J. S., and Poon, J. K. (2014). Electronic and thermal effects in the insulator-metal phase transition in VO_2 nano-gap junctions. Applied Physics Letters,105(23), 231904.

[82] Sanchez, L., Lechago, S., Gutierrez, A., and Sanchis, P. (2016). Analysis and Design Optimization of a Hybrid VO_2/Silicon 2x2 Microring Switch. IEEE Photonics Journal, 8(2), 1-9.

[83] Maddalon, C., Barla, K., Denis, E., Lous, E., Perrin, E., Lis, S., ... and Dehan, E. (2000). Planarization properties of hydrogen silsesquioxane (HSQ) influence on CMP. Microelectronic engineering,50(1), 33-40.

[84] Van Bilzen, B., Homm, P., Dillemans, L., Su, C. Y., Menghini, M., Sousa, M., ... and Locquet, J. P. (2015). Production of VO_2 thin films through post-deposition annealing of V_2O_3 and VOx films. Thin Solid Films, 591, 143-148.

[85] Sánchez, L., Gutierrez, A. M., Brimont, A., & Sanchis, P. (2015, August). Design of an ultra-compact hybrid VO $_2$/silicon switch. In 2015 IEEE 12th International Conference on Group IV Photonics (GFP) (pp. 100-101).

[86] Chen, S., Yi, X., Ma, H., Wang, H., Tao, X., Chen, M., and Ke, C. (2003). A novel structural VO_2 micro-optical switch. Optical and quantum electronics,35(15), 1351-1355.

[87] Kruger, B. A., Joushaghani, A., and Poon, J. K. (2012). Design of electrically driven hybrid vanadium dioxide (VO_2) plasmonic switches. Optics express, 20(21), 23598-23609.

[88] Wang, H., Yi, X., Chen, S., and Fu, X. (2005). Fabrication of vanadium oxide micro-optical switches. Sensors and Actuators A: Physical, 122(1), 108-112.

[89] Markov, P., Appavoo, K., Haglund, R. F., and Weiss, S. M. (2015). Hybrid Si-VO_2-Au optical modulator based on near-field plasmonic coupling. Optics express, 23(5), 6878-6887.

[90] Seo, G., Kim, B. J., Kim, H. T., and Lee, Y. W. (2014). Thermally-or optically-biased memristive switching in two-terminal VO_2 devices. Current Applied Physics,14(9), 1251-1256.

[91] Pellegrino, L., Manca, N., Kanki, T., Tanaka, H., Biasotti, M., Bellingeri, E., ... and Marré, D. (2012). Multistate Memory Devices Based on Free-standing VO_2/TiO_2 Microstructures Driven by Joule Self-Heating. Advanced Materials, 24(21), 2929-2934.

[92] Driscoll, T., Kim, H. T., Chae, B. G., Di Ventra, M., and Basov, D. N. (2009). Phase-transition driven memristive system. Applied physics letters, 95(4), 043503.

[93] Coy, H., Cabrera, R., Sepúlveda, N., and Fernández, F. E. (2010). Optoelectronic and all-optical multiple memory states in vanadium dioxide. Journal of Applied Physics, 108(11), 113115.
[94] Kim, J. T. (2015). Silicon optical modulators based on tunable plasmonic directional couplers. IEEE Journal of Selected Topics in Quantum Electronics, 21(4), 184-191.
[95] Yin, M., Deng, Q., Li, Y., Wang, X., and Li, H. (2015). Ultrashort and low-loss polarization rotators utilizing hybrid plasmonic-dielectric couplers. Photonics Technology Letters, IEEE, 27(3), 229-232.
[96] Kim, S., and Qi, M. (2015). Polarization rotation and coupling between silicon waveguide and hybrid plasmonic waveguide. Optics express, 23(8), 9968-9978.
[97] Spanke, R. A. (1987). Architectures for guided-wave optical space switching systems. Communications Magazine, IEEE, 25(5), 42-48.